

Austenite stability in TRIP steels studied by synchrotron radiation

-

PhD Thesis

Austenite stability in TRIP steels studied by synchrotron radiation

Proefschrift

ter verkrijging van de graad van doctor
aan de Technische Universiteit Delft,
op gezag van de Rector Magnificus prof. ir. K.C.A.M. Luyben,
voorzitter van het College voor Promoties,
in het openbaar te verdedigen op maandag 31 maart 2014 om 15:00 uur

door

Romain BLONDÉ

Master in Material Sciences, Paul-Verlaine University of Metz

geboren te Belfort, France

Dit proefschrift is goedgekeurd door de promotor:

Prof. dr. E.H. Brück

Prof.dr.ir. S. van der Zwaag

Copromotor Dr.ir. N.H. van Dijk

Samenstelling promotiecommissie:

Rector Magnificus,	voorzitter
Prof. dr. E.H. Brück,	Technische Universiteit Delft, promotor
Prof.dr.ir. S. van der Zwaag,	Technische Universiteit Delft, promotor
Dr.ir. N.H. van Dijk,	Technische Universiteit Delft, copromotor
Prof.dr. M. Preuss,	The University of Manchester
Prof.dr.ir. A.S.J. Suiker,	Technische Universiteit Eindhoven
Prof.dr.ir. J. Sietsma,	Technische Universiteit Delft
Dr.Ing. U. Prahll,	RWTH Aachen University
Prof.dr. F.M. Mulder,	Technische Universiteit Delft, reservelid

This research was carried out under project number M41.5.08313 in the framework of the Research Program of Materials innovation institute (M2i) in the Netherlands (www.m2i.nl)

Copyright © 2014 by Romain Blondé

All rights reserved. No part of the material protected by this copyright notice may be reproduced or utilized in any form or by any means, electronic or mechanical, including photocopying, recording or any information storage and retrieval system, without permission from the publisher.

ISBN: 978-94-91909-03-0

Printed in The Netherlands by Uitgeverij BOXPress

Contents

Introduction	1
1.1 State of the art	2
1.2 Aim of the thesis.....	3
1.3 Contents of the thesis.....	3
1.4 References	5
Experimental methods	7
2.1 Instrumental setup	7
2.2 Theory of three-dimensional x-ray diffraction microscopy	11
2.3 References	12
Optimisation of the fraction of metastable austenite in TRIP steels	13
3.1 Introduction	13
3.2 Experimental methods.....	14
3.3 Results and discussion	15
3.3.1 Austenite fraction at room temperature	15
3.3.2 Austenite stability below room temperature.....	17
3.4 Conclusions	19
3.5 References	19
Tensile experiments at variable temperatures	21
4.1 Introduction	21
4.2 Experimental methods.....	23
4.2.1 Sample preparation	23
4.2.2 In-situ high-energy X-ray diffraction.....	24
4.2.3 Data analysis.....	26
4.3 Results and discussion	27
4.3.1 Macroscopic behaviour.....	27

4.3.2	Evolution of the austenite phase fraction.....	28
4.3.3	Relative change in lattice parameter.....	31
4.3.4	Lattice plane strain for individual $\{hkl\}$ planes.....	36
4.3.5	Austenite stability for different $\{hkl\}$ planes.....	39
4.3.6	Texture analysis.....	41
4.4	Conclusions.....	43
4.5	References.....	44
Shear experiments for different bainitic holding times.....		47
5.1	Introduction.....	47
5.2	Experimental methods.....	49
5.2.1	Sample preparation.....	49
5.2.2	In-situ high-energy X-ray diffraction.....	49
5.2.3	Data analysis.....	51
5.3	Results and discussion.....	53
5.3.1	Macroscopic mechanical behaviour.....	53
5.3.2	Evolution of the austenite phase fraction.....	55
5.3.3	Relative change in lattice parameter.....	56
5.3.4	Austenite stability for individual $\{hkl\}$ planes.....	61
5.3.5	Texture analysis.....	64
5.3.6	Comparison between shear and tensile deformation.....	66
5.4	Conclusions.....	67
5.5	References.....	68
Mapping investigation during shear experiments.....		71
6.1	Introduction.....	72
6.2	Experimental methods and data analysis.....	73
6.2.1	Sample preparation.....	73
6.2.2	In-situ high-energy X-ray diffraction.....	74
6.2.3	Analysis of diffraction data.....	75
6.2.4	Finite element modelling.....	76
6.3	Results and discussion.....	78
6.3.1	Macroscopic mechanical behaviour.....	78
6.3.2	Development of elastic shear strains.....	79
6.3.3	Transformation behaviour of metastable austenite.....	83
6.3.4	Comparison with finite element modelling.....	87

6.4	Conclusions	87
6.5	References	88
	Individual grain analysis during tensile test.....	91
7.1	Introduction	91
7.2	Experimental methods.....	92
7.2.1	Sample preparation	92
7.2.2	In-situ high-energy X-ray diffraction.....	93
7.2.3	Data analysis.....	95
7.3	Results and discussion	97
7.3.1	Macroscopic behaviour & phase fraction evolution.....	97
7.3.2	Initial microstructure	98
7.3.3	Microstructure evolution	99
7.3.4	High-precision transformation behaviour of individual grains.....	104
7.4	Conclusions	107
7.5	References	108
	High resolution XRD investigation of individual austenite grains	111
8.1	Introduction	111
8.2	Experimental details.....	113
8.2.1	Sample preparation	113
8.2.2	Experimental setup.....	114
8.2.3	Experimental procedure	115
8.3	Data analysis	119
8.3.1	Powder data analysis	119
8.3.2	Data analysis of single grains on the near-field detector.....	119
8.3.3	Data analysis of single grains on the far-field detector	120
8.4	Results and discussion	120
8.4.1	Macroscopic mechanical behaviour	120
8.4.2	Austenite phase fraction evolution	120
8.4.3	Single grain analysis.....	122
8.4.4	High resolution data analysis.....	123
8.4.5	Strain effect on the sub structure of individual austenite grains.....	127
8.5	Conclusions	130
8.6	References	131
	Summary	133

Samenvatting	137
List of publications	143
Acknowledgements.....	145
Curriculum Vitae	149

Chapter 1

Introduction

The development of modern automotive vehicles with improved environmental, safety and vehicle performance has driven the development of a variety of new steel grades that are lighter, safer, greener and more cost effective. Low-alloyed Transformation Induced Plasticity (TRIP) steel were especially developed for automotive applications in the 80s [1-3] and provide remarkable large elongation values, while retaining high-strength characteristics [4-9] (Fig. 1.1). Their complex microstructure at room temperature comprises three phases: ferrite, carbide-free bainite and retained austenite [10,11]. The beneficial mechanical properties of this advanced steel are coming from the multiphase microstructure, but also from the TRIP phenomenon, which consist of the diffusionless transformation of the soft austenite to the strong martensite providing a high tensile strength without deterioration of the uniform elongation [12,13] (Fig. 1.2).

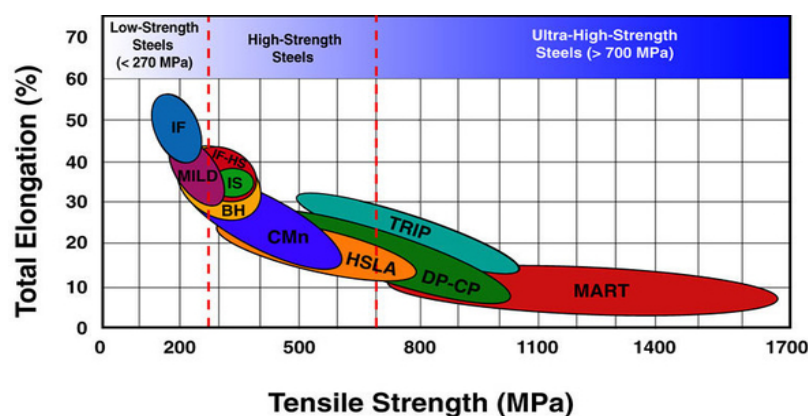


Figure 1.1: A comparison of relationship between ultimate tensile strength to total elongation of various steels [14].

The austenite phase is thermodynamically stable only at high temperatures. However by combining different alloying elements with a specific thermal process route, it is possible to retain a significant amount of austenite at room temperature in a metastable condition. The process route for the material is composed of two annealing steps: an intercritical annealing followed by a first quench to the temperature region where the bainite transformation takes place. After a specific holding time the material a second quench to room temperature is applied. Great efforts have been devoted to optimize the process route in order to retain a higher volume of austenite in metastable condition, which leads to improved mechanical response of the TRIP steel.

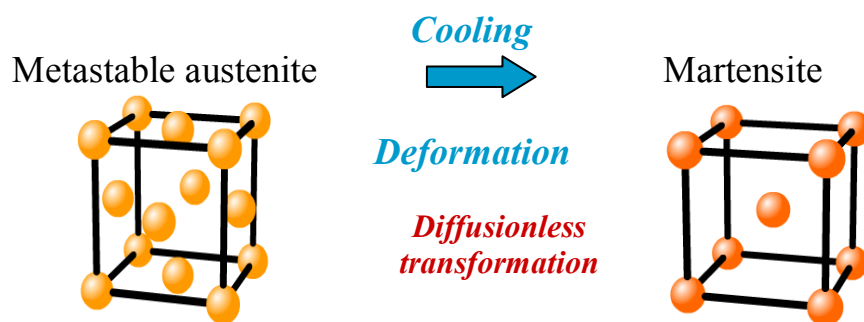


Figure 1.2: Schematic representation of the Transformation Induced Plasticity (TRIP) phenomenon.

1.1 State of the art

Despite the advantages offered by TRIP steels their volumes consumed in automotive markets remain low. This is partly due to the complex microstructure of the material and limited the insight in how the TRIP mechanism contributes to the overall performance in complex stress states. The key microstructure-property relationships have not been sufficiently well defined. This knowledge gap is a major obstacle for commercial developments since TRIP steels cannot be designed to meet specific application requirements. A more accurate control of the austenite stability is required to envisage wider industrial applications.

Recently, the research efforts of our group have yielded the first *in-situ* experimental information about the martensitic transformation of individual austenite grains within the -multiphase TRIP microstructure,

using synchrotron X-ray diffraction measurements during cooling the material [15-18]. Both the carbon content and grain volume of a significant number of individual grains were monitored throughout their martensitic transformation to obtain the first quantitative experimental data on the stabilizing effects of both parameters on the austenite phase. An accurate control of the spread in austenite grain size and the carbon content is an absolute requirement to control the TRIP properties of the material and thus the optimization of the mechanical properties. However, these results only convey information about the effect of two microstructural parameters on the thermal stability of the austenite grains. The stability of the austenite grains however depends on several intrinsic (carbon content, grain size and orientation) and extrinsic (local stress, surrounding microstructure) microstructural parameters. Furthermore, the martensitic transformation cannot only be activated thermally, but also by applied stress.

1.2 Aim of the thesis

In this PhD project the thermally- and mechanically- induced martensitic transformation of metastable austenite is studied in-situ within the bulk of TRIP steels. This transformation behaviour is correlated to the microstructure evolution. Different deformation modes have been investigated to characterize the austenite stability. A detailed study has been conducted to characterize the stability of individual austenite grains and characterize the interplay between microstructural parameters, like grain volume, carbon concentration and grain orientation within the bulk material to the mechanical stimuli. In-situ high-energy X-rays diffraction technique employed in this study will provide new insights into the factors determining the mechanical austenite stability. Three experiments have been conducted at the European Synchrotron Facility Source, Grenoble, FRANCE and at the Deutsches Elektronen-Synchrotron, Hamburg, GERMANY to achieve new insight in the transformation behaviour of metastable austenite in TRIP steels.

1.3 Contents of the thesis

In *Chapter 2* the experimental methods relevant for the high-energy X-ray diffraction experiments are briefly explained.

The experimental work conducted in this study is presented in six chapters. In *Chapter 3*, the retained austenite in metastable condition has been optimized for our material by tuning both the bainitic transformation temperature and bainitic holding time. Dilatometry and magnetization experiments have been conducted to determine the austenite fraction and its stability. These results led to an optimised sample preparation route for the synchrotron experiments.

Chapter 4 presents the results of the high-energy X-ray diffraction experiments during tensile tests at variable temperatures down to 153 K on low-alloyed TRIP steels. A detailed powder analysis has been performed to probe the austenite-to-martensite transformation by characterizing the evolution of the phase fraction, load partitioning and texture of the constituent phases simultaneously. The results show that at lower temperatures the mechanically induced austenite transformation is significantly enhanced and extends over a wider deformation range, resulting in a higher elongation at fracture. Low carbon content grains transform first, leading to an initial increase in average carbon concentration of the remaining austenite.

Chapter 5 presents the results on the microstructure evolution during shear loading of low-alloyed TRIP steels with different amounts of the metastable austenite phase and its equivalent Dual Phase (DP) grade studied by in-situ high-energy X-ray diffraction. A similar powder data analysis as presented in *Chapter 4* has been performed to investigate the behaviour of the constituent phases of the materials. The results show that for shear deformation the TRIP effect extends over a significantly wider deformation range than for simple uniaxial loading. A clear increase in average carbon content during the mechanically-induced transformation indicates that austenite grains with a low carbon concentration are least stable during shear loading.

Chapter 6 presents the results focusing on the determination of the local retained austenite-to-martensite transformation behaviour in an inhomogeneous yet carefully controlled shear loaded region of double notched TRIP and DP steel samples. The interplay between local strain development and the austenite-to-martensite transformation in low-alloyed TRIP steel has been studied in-situ during shear deformation by spatially resolved high-energy X-ray diffraction experiments in the vicinity of the shear

zone. The results indicate that the metastable retained austenite shows a mechanically-induced martensitic transformation in the localized shear zone, which is accompanied by a carbon enrichment of the remaining austenite. At the later deformation stages the geometry of the shear test samples results in the development of an additional tensile component. The experimental strain field within the probed sample area is in good agreement with finite-element calculations.

Chapter 7 presents the results on the stability of individual austenite grains in metastable condition studied in situ in low-alloyed TRIP steels. An analysis has been performed to correlate the macroscopic behavior of the material to the microstructural parameters of individual grains. The grain volume, carbon concentration, grain orientation and position have been investigated. Our results show the carbon concentration, grain volume and orientation play a significant role in the austenite stability. The grain volume is found to be the most relevant factor in the determination of the mechanical stability. The effect of the grain orientation on the mechanical austenite stability of individual grains has been determined experimentally: as expected grains with the highest Schmid factor showed the lowest stability.

Chapter 8 presents the results on the martensitic transformation behavior of the meta-stable austenite phase in low-alloyed TRIP steels has been studied in-situ using high-energy X-ray diffraction during tensile deformation. For the first time, a high resolution far-field detector was used to study the initial and evolving structure of individual austenite grains during uniaxial tensile deformation of the sample. The sub-grain size in austenite is found not to change significantly during the deformation. The final transformation to martensite occurred in either one or two loading steps.

1.4 References

- [1] O. Matsumura, Y. Sakuma, H. Takechi, *Trans. ISIJ* 27 (1987) 570.
- [2] O. Matsumura, Y. Sakuma, H. Takechi, *Scripta. Mater.* 21 (1987) 1301.
- [3] H.C. Chen, H. Era, M. Shimizu, *Metall. Trans.* 20A (1989) 437.
- [4] S. Oliver, T.B. Jones, G. Fournalis. *Mat. Sci. Tech.* 23 (2007) 423.
- [5] O. Kwon, K. Lee, G. Kim, K.G. Chin. *Mat. Sci. Forum* 638-642 (2010) 136.
- [6] A.K. Srivastava, G. Jha, N. Gope, S.B Singh. *Mat. Charact.* 57 (2006) 127.

-
- [7] L. Skálová, R. Divišová, J. Jandová. *Mat. Proc. Tech.* 175 (2006) 387.
- [8] A. Kammouni, W. Saikaly, M. Dumont, C. Marteau, X. Bano, A. Charai. *Mat. Sci. Eng. A* 518 (2009) 89.
- [9] J. Chiang, B. Lawrence, J.D. Boyd, A.K Pilkey. *Mat. Sci. Eng. A* 528 (2011) 4516.
- [10] S. Zaeferrer, J. Olhert, W. Bleck. *Acta Mater.* 52 (2004) 2765.
- [11] I.B. Timokhina, P.D. Hodgson, E.V. Pereloma. *Metall. Mater. Trans. A* 35A (2004) 2331.
- [12] P.J Jacques, Q. Furnémont, F. Lani, T. Pardoën, F. Delannay. *Acta Mater.* 55 (2007) 3681.
- [13] W.J. Dan, W.G. Zhang, S.H. Li, Z.Q. Lin. *Comp. Mat. Sci.* 40 (2007) 101.
- [14] J. Edgar, *Steel Identification Using Hardness Testing*, (2008)
http://www.autospeed.com/cms/title_Steel-Identification-Using-Hardness-Testing/A_109717/article.html
- [15] N.H. van Dijk, A.M. Butt, L. Zhao, J. Sietsma, S.E. Offerman, J.P. Wright, S. van der Zwaag. *Acta Mater.* 53 (2005) 5439.
- [16] E. Jimenez-Melero, N.H. van Dijk, L. Zhao, J. Sietsma, S.E. Offerman, J.P. Wright, S. van der Zwaag. *Acta Mater.* 55 (2007) 6713.
- [17] E. Jimenez-Melero, N.H. van Dijk, L. Zhao, J. Sietsma, S.E. Offerman, J.P. Wright, S. van der Zwaag. *Scripta Mater.* 56 (2007) 421.
- [18] E. Jimenez-Melero, N.H. van Dijk, L. Zhao, J. Sietsma, S.E. Offerman, J.P. Wright, S. van der Zwaag. *Acta Mater.* 57 (2009) 533.

Chapter 2

Experimental methods

2.1 Instrumental setup

The three dimensional X-ray diffraction experiments described in this thesis were performed at the instrument ID11 at the European Synchrotron Radiation Facility (ESRF) Grenoble, FRANCE and at the instrument P07 at the Deutsches Elektronen-Synchrotron (DESY), Hamburg, GERMANY. A schematic drawing of the experimental set-up to study the austenite stability in low-alloyed TRIP steels is shown in Fig 2.1.

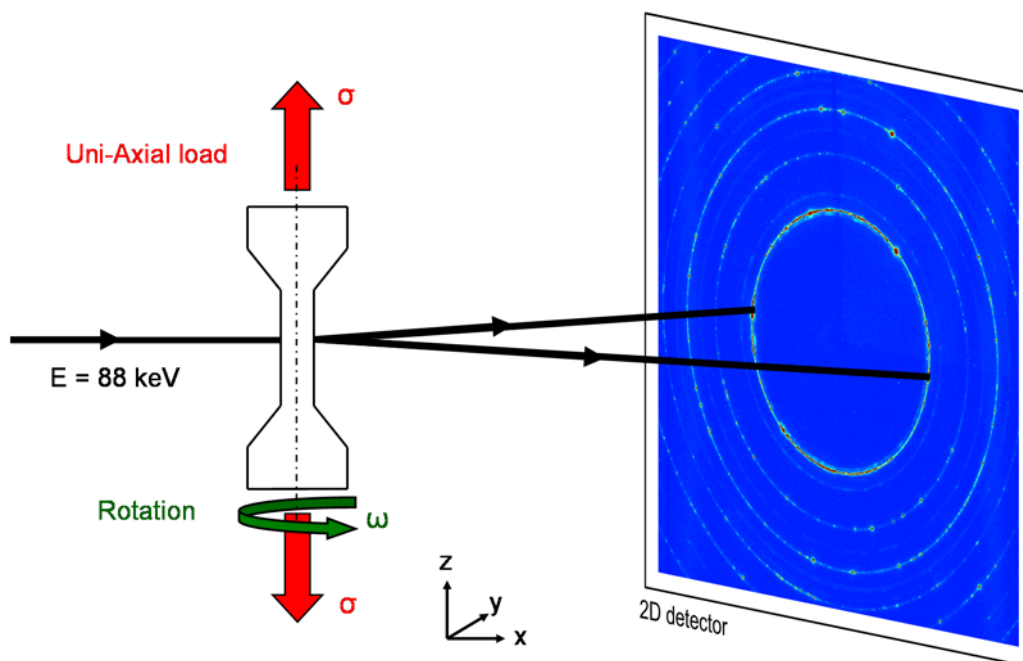


Figure 2.1: Schematic representation of the experimental setup used for the high-energy microbeam X-ray diffraction experiments on low-alloyed TRIP steels.

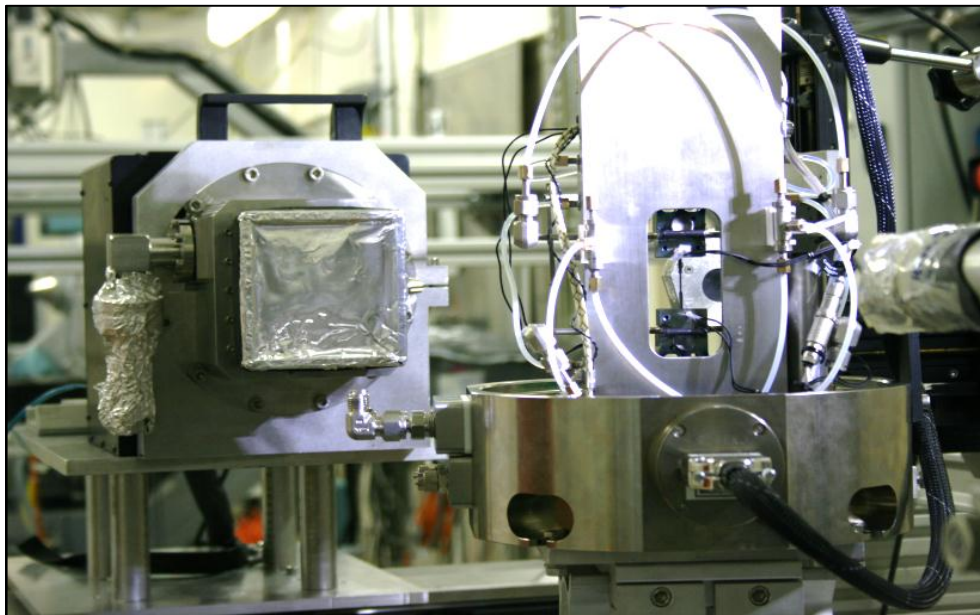
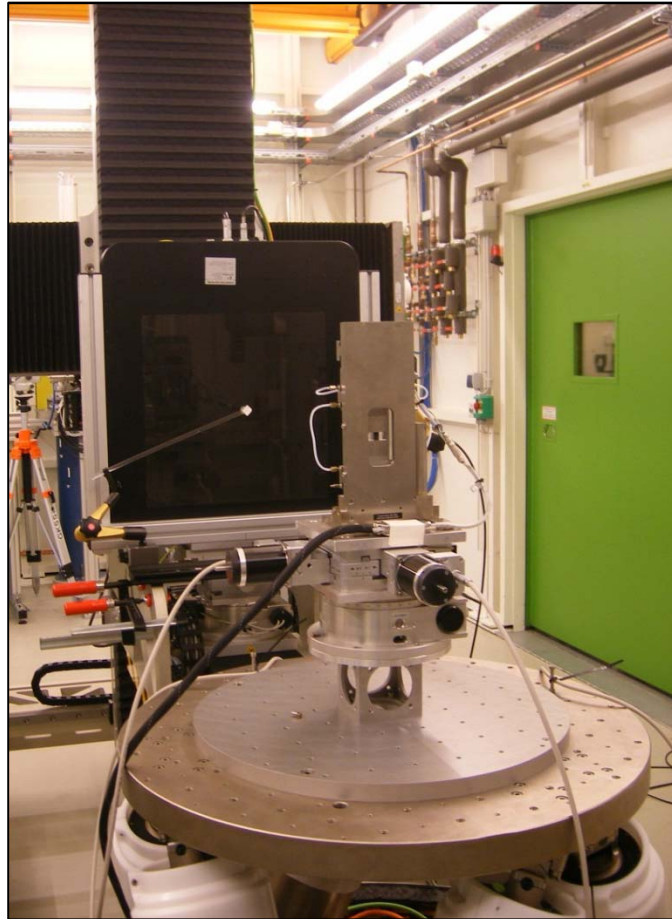


Figure 2.2: *Synchrotron X-rays diffraction experiments on low-alloyed TRIP steels at P07 (up) and ID11 (bottom). The sample is mounted on a tensile microtester placed on table able to translate in three directions (x , y , z) and rotate along the vertical axis (ω). In the background is the 2-dimensional CCD detector.*

Fig 2.2 shows the experimental hutch of the beamline where the experiments have been performed. A white synchrotron beam diffracts from a bent silicon Laue crystal, which induces a monochromatic X-ray beam with an energy of around 70-90 keV depending on the instrument. A set of slits defines the shape and the size of the X-ray beam. For our powder experiments the beam dimension was $100 \times 100 \mu\text{m}^2$. In order to illuminate the sample uniformly, a homogeneous flux of photon is required over the cross-section of the beam. As shown in Fig 2.3, the sample is mounted on a 2kN Deben microtester, which allows the in-situ studies of the austenite stability in low-alloyed TRIP steels by X-ray diffraction. The microtester is positioned on a table, which can be translated in three directions (x, y, z) and rotated over an angle ω . The diffracted X-rays are recorded with a 2D-CCD detector. For the high-resolution X-ray diffraction analysis, presented in chapter 8, a second 2D-CCD detector is positioned at a longer distance behind the first detector.

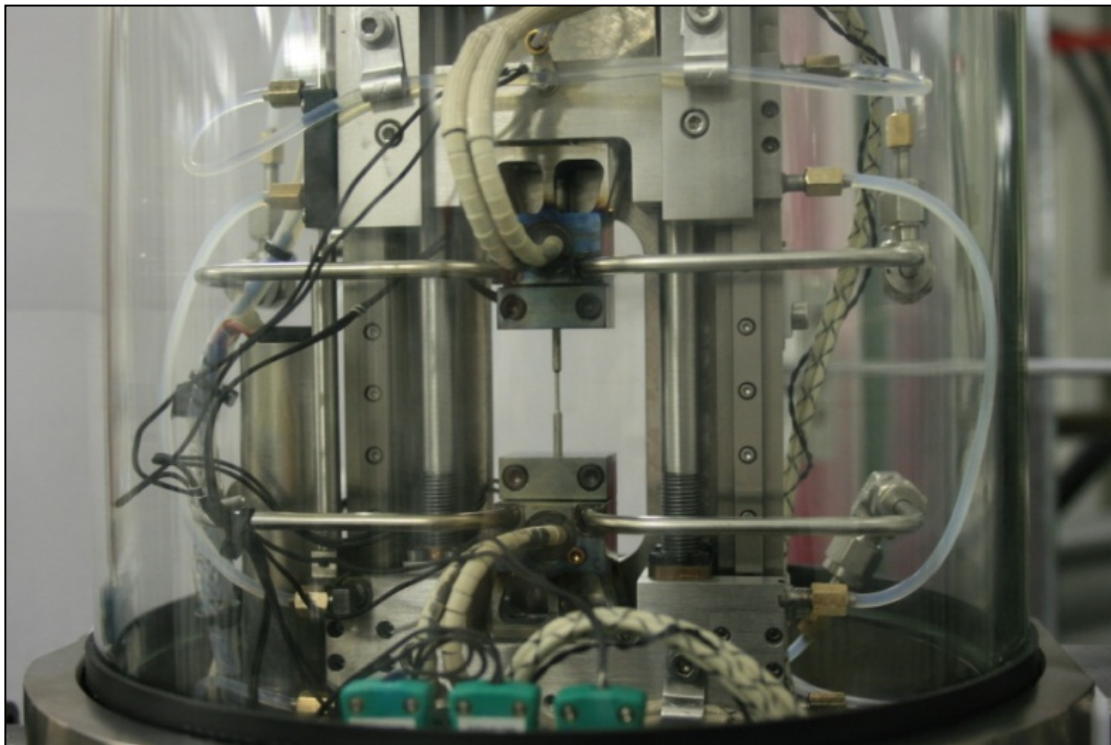


Figure 2.3: *Low-alloyed TRIP steels sample mounted on the 2kN Deben tensile microtester. The glass dome allows for temperature dependent experiments under vacuum. The grips can be heated by cartridge heaters or cooled with cold N_2 gas.*

Fig 2.4a shows the 2D X-ray diffraction pattern of the powder experiments of the multiphase TRIP microstructure. Full diffraction rings are observed due to a high number of grains monitored simultaneously during the experiment. For single grain experiments, separate diffraction spots appear on the recorded diffraction pattern, as shown in Fig 2.4b. It is possible to detect separate reflections by choosing a relatively small beam size of $20 \times 20 \mu\text{m}^2$ corresponding to a size about 4 times bigger than the average austenite grain size in the sample. As a consequence, a limited number of grains contribute to the diffraction pattern. The recording time of the diffraction patterns for these experiments was 0.2 s. To verify that particular grains are not partly monitored and then completely positioned within the illuminated volume, 2 bigger beam sizes of $30 \times 30 \mu\text{m}^2$ and $40 \times 40 \mu\text{m}^2$ were also used for each single grain measurement. In the case that a grain would be partly monitored, an increase in Bragg intensity of the corresponding diffraction spots is observed when a bigger beam sizes is used.

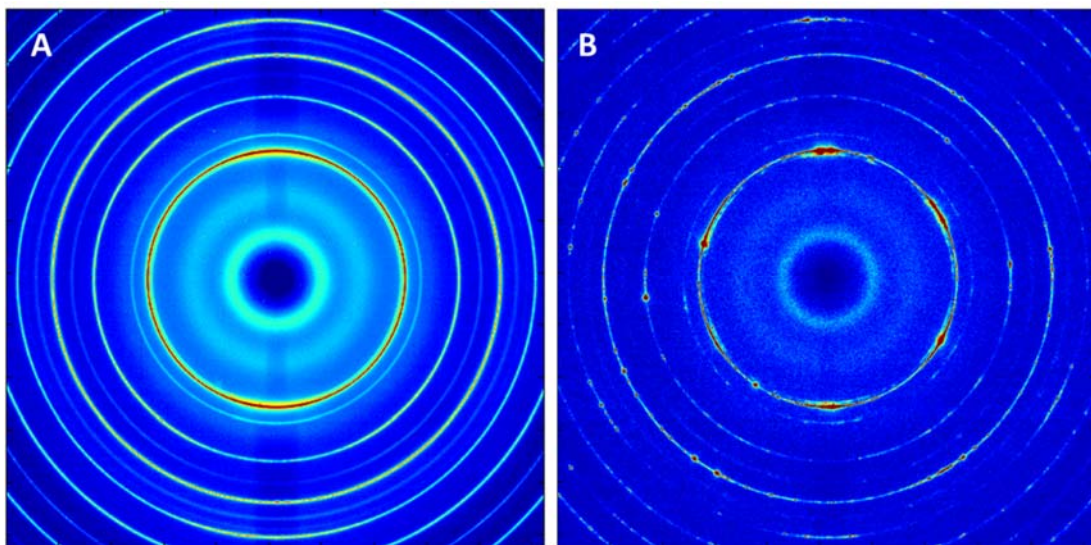


Figure 2.4: (a) Two-dimensional X-ray diffraction pattern using a beam of $100 \times 100 \mu\text{m}^2$ showing a powder pattern (b) and a beam of $20 \times 20 \mu\text{m}^2$ showing single reflections.

In addition, it is also necessary to verify that the monitored volume within the sample remains identical during the mechanical test. The mechanical stability of the austenite grains is investigated by applying macroscopic deformation. To verify that the same grains are monitored after each macroscopic strain step, the coordinate of an untransforming reference ferrite grain within the sample is tracked. The X-ray beam is realigned on this grain for each deformation step.

2.2 Theory of three-dimensional x-ray diffraction microscopy

For each of the diffraction spots, the integrated intensity I_g is related to the volume of the grain V_g by the following equation [1,2]:

$$I_g = \Phi_0 r_0^2 \frac{\lambda^3 |F_{hkl}|^2 V_g}{\Delta\omega |\sin\eta| v^2} L_g P T_r \exp(-2M) \quad (1)$$

where Φ_0 is the incident flux of photons, F_{hkl} is the structure factor of the $\{hkl\}$ reflection, λ is the photon wavelength, $\Delta\omega$ is the angular range over which the grain is rotated, v is the volume of the unit cell, P is the polarization factor, and T_r is the transmission factor. The Lorentz factor of the grain is given by $L_g = 1/\sin(2\theta)$, where 2θ is the scattering angle. The angles η and ω are the azimuthal angle and sample rotation angle respectively. The Thomson scattering length r_0 is given by:

$$r_0 = \frac{e^2}{4\pi\epsilon_0 m_e c^2} = 2.82 \times 10^{-15} \text{ m} \quad (2)$$

where $e = 1.602 \times 10^{-19} \text{ C}$ is the electron charge, $m_e = 9.1094 \times 10^{-31} \text{ kg}$ is the electron mass, $c = 2.9979 \times 10^8 \text{ m/s}$ is the velocity of light, and $\epsilon_0 = 8.85419 \times 10^{-12} \text{ F/m}$ is the permittivity of vacuum.

The Debye-Waller factor $\exp(-2M)$ accounts for the thermal vibrations of the atoms [3],

$$M = \frac{6h^2 T}{m k_B \Theta^2} \left[\phi(x) + \frac{x}{4} \right] \left(\frac{\sin\theta}{\lambda} \right)^2 \quad (3)$$

where $h = 6.62608 \times 10^{-34} \text{ Js}$ is the plank constant, m is the mass of the vibrating atom, $k_B = 1.381 \times 10^{-23} \text{ J/K}$ is the Boltzman constant, Θ is the Debye temperature, $x = \Theta/T$ is the relative

temperature, T is the temperature, and ϕ is given by:

$$\phi(x) = \frac{1}{x} \int_0^x \frac{\zeta}{\exp(\zeta) - 1} d\zeta \quad (4)$$

For a powder diffraction experiment, the integrated intensity I_p of a $\{hkl\}$ -diffraction ring of a polycrystalline material with randomly oriented grains is given by:

$$I_p = \Phi_0 r_0^2 \frac{m_{hkl} \lambda^3 |F_{hkl}|^2 V}{v^2} L_g P \exp(-2M) \quad (5)$$

where m_{hkl} is the multiplicity factor of the $\{hkl\}$ -ring and V is the volume of the diffracting phase. The Lorentz factor for a powder is given by $L_p = 1/(4 \sin(\theta))$. The volume of the diffraction phase is given by:

$$V = f_i V_{gauge} \quad (6)$$

where f_i is the volume fraction of the diffraction phase and V_{gauge} is the gauge volume, which is defined by the beam size and the thickness of the sample.

The volume of an individual grain is calculated from the integrated Bragg peak intensity of a grain I_g normalized by the powder intensity of the $\{hkl\}$ -ring in which the reflection from the individual grain appeared.

$$V_g = \frac{1}{2} m_{hkl} \Delta\omega |\sin \eta| \cos(\theta) f_i V_{gauge} \frac{I_g}{I_p} \quad (7)$$

2.3 References

- [1] J. Als-Nielsen and D. McMorrow, Elements of Modern X-ray Physics, Wiley, West Sussex (2001).
- [2] B. E. Warren, X-ray Diffraction, Dover Publications, New York, (1990).
- [3] B. D. Cullity and S. R. Stock, Elements of X-ray Diffraction, Prentice-Hall, New Jersey, (2001).

Chapter 3

Optimisation of the fraction of metastable austenite in TRIP steels

We have performed in-situ magnetization and high-energy X-ray diffraction measurements on two aluminum-based TRIP steels from room temperature down to 100 K in order to evaluate amount and stability of the retained austenite for different heat treatment conditions. We have found that the bainitic holding temperature affects the initial fraction of retained austenite at room temperature but does not to influence significantly the rate of transformation upon cooling.

3.1 Introduction

Low-alloyed transformation-induced plasticity (TRIP) steels have attracted significant interest for automotive applications due to their high strength and formability [1]. A relatively complex two-stage heat treatment leads to the presence of a significant amount of austenite (<20%) in a metastable condition at room temperature [2]. The transformation of this metastable austenite into martensite can be induced by changes in temperature and/or an applied stress [3,4]. This transformation seems to constitute the key process to obtain a high work hardening rate and a large uniform elongation in these materials [2,4]. We have recently derived a new equation that links the martensitic transformation temperature not only to the carbon content of the austenite grains but also to the grain size [5]. These two microstructural parameters are controlled by the heat treatment and the chemical composition of the material. The aim of this work is to maximize the amount of metastable austenite present in the room-temperature TRIP microstructure in order to improve the strength/ductility combination in these materials. To achieve this goal, we have varied the heat treatment parameters systematically in two aluminum-based TRIP steel grades. We have subsequently studied the thermal stability of the retained

austenite by using two in-situ bulk techniques: magnetization measurements using a SQUID magnetometer [6] and high-energy X-ray diffraction at a synchrotron source [5,7].

3.2 Experimental methods

Two TRIP steels grades with a different aluminum content were used: 0.188C-1.502Mn-0.254Si-0.015P-0.443Al ($Al_{0.4}$) and 0.218C-1.539Mn-0.267Si-0.018P-1.750Al ($Al_{1.8}$) in wt.%. Cylindrical samples with a length of 10 mm and a diameter of 5 mm were machined from the hot-rolled steel material and heat treated under vacuum using a Bähr 850a dilatometer. The samples were first annealed during 30 minutes at an intercritical temperature of 1098 K for $Al_{0.4}$ and 1143 K for $Al_{1.8}$, corresponding to approx. equal fractions of austenite and ferrite. The second stage was to quench the samples to a lower temperature where part of the intercritical austenite transformed into bainite. In order to assess the influence of the bainitic holding temperature (T_{bh}) on the resultant TRIP microstructure at room temperature, we have prepared samples at three different temperatures: 623, 648 and 673 K. At each temperature, the holding time was varied systematically from 30 s to 10 min. Finally, the material was quenched to room temperature. The austenite grains with sufficient stability did not transform into martensite during the final quenching step and remained in the room-temperature microstructure in a metastable condition. This specific heat treatment yielded a multiphase microstructure composed of ferrite, bainite and retained austenite. Fig. 3.1 shows the resultant microstructure of $Al_{0.4}$ and $Al_{1.8}$ at room temperature for two bainitic holding temperatures: 623 and 673 K, and a holding time of 2 min. The thermal stability of retained austenite was studied by magnetization measurements using a SQUID magnetometer while cooling the material down to 100 K and heating back to room temperature in the presence of magnetic field of 5 T. The difference in saturation magnetization of the TRIP steel containing the metastable austenite and the as-received ferritic steel is directly related to the volume fraction of the non-magnetic austenite [6]. The magnetization results are compared with those of our earlier in-situ high-energy ($E = 80$ keV) X-ray diffraction measurements performed in transmission geometry at the beam line ID11 of the European Synchrotron Radiation Facility (Grenoble, France) [5,7]. In this experiment, the sample was cooled from room temperature to 100 K in steps of 20 K using a nitrogen

gas cryostream cooler. For each temperature step, the diffracted intensity from the different phases present in the microstructure was recorded on a two-dimensional detector placed behind the sample.

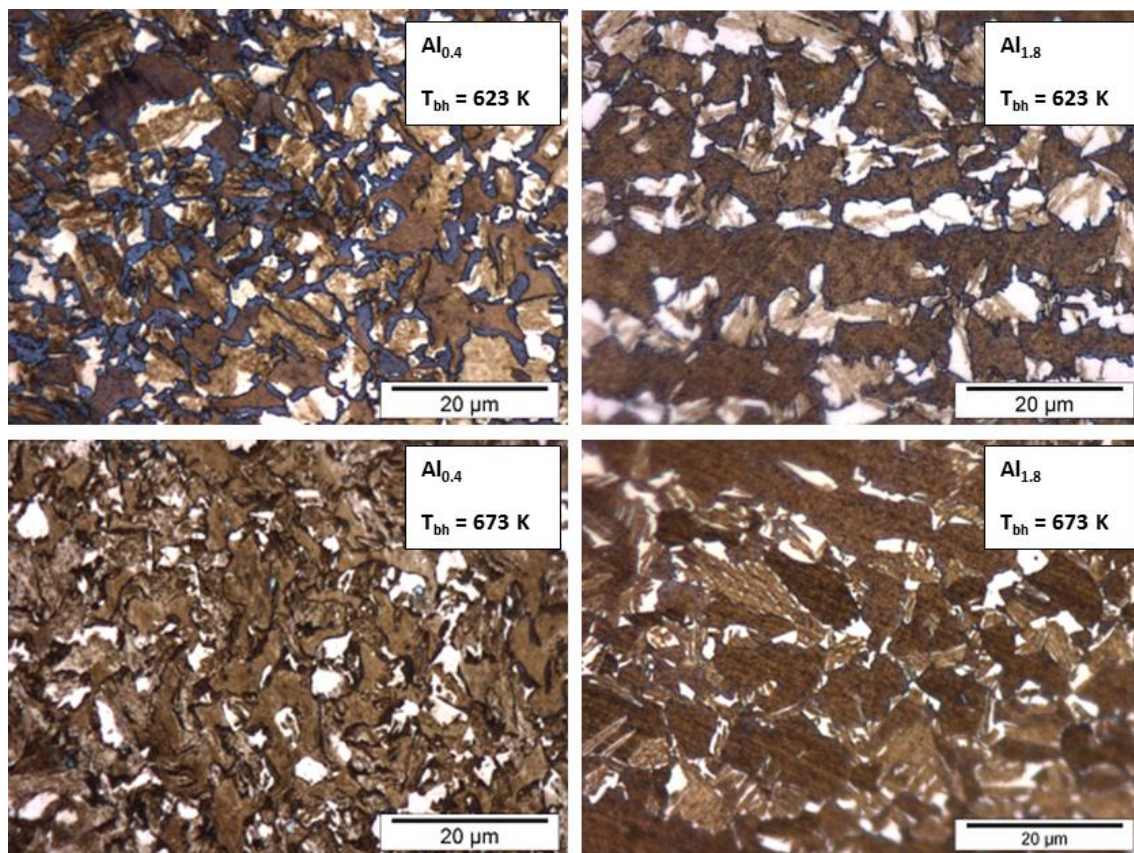


Figure 3.1: Room-temperature microstructure of the two studied TRIP steel grades as revealed by optical microscopy. The micrographs correspond to a bainitic holding temperature of $T_{bh} = 623$ and 673 K and a holding time of 2 min. Austenite and martensite appear in white, while bainite and ferrite grains are shown in brown.

3.3 Results and discussion

3.3.1 Austenite fraction at room temperature

Fig. 3.2 shows the austenite fraction present at room temperature as a function of the bainitic holding temperature and time for the two studied TRIP compositions. Fig. 3.2b shows that for the $Al_{1.8}$ sample and $T_{bh} = 673$ K, the austenite fraction increases with the holding time up to 2 min and then decreases slowly at longer times. By decreasing the bainitic temperature from 673 to 623 K, the austenite fraction is reduced and the maximum in the austenite fraction is shifted towards longer times. By comparing Fig. 3.2a and b, the austenite fraction at room temperature turns out to be lower for the $Al_{0.4}$ sample than

for the $Al_{1.8}$ sample at the same T_{bh} . The shape of the curve is similar for both compositions, but in the case of $Al_{0.4}$ the maximum in austenite fraction appears at a shorter holding time of 1 min at 673 K and 2 min at 648 K and 623 K. The retained austenite fraction decreases faster at longer holding times in the $Al_{0.4}$ sample.

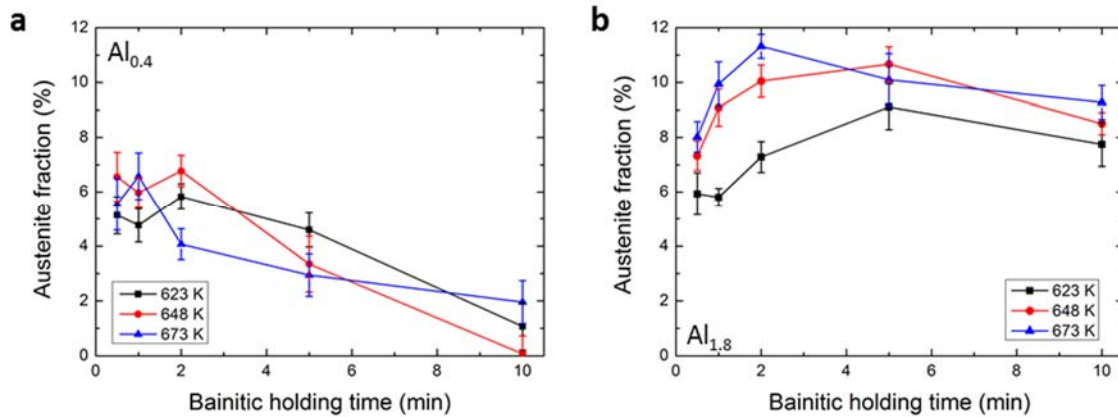


Figure 3.2: Variation of the austenite fraction at room temperature with the bainitic holding temperature and time for (a) $Al_{0.4}$ and (b) $Al_{1.8}$.

The microstructure of TRIP steels depends on the bainitic holding time. For short holding times, the austenite fraction at room temperature is relatively low due to a limited carbon enrichment during the bainitic transformation. Consequently, part of the austenite transforms into martensite during the quenching to room temperature. By increasing the holding time, the austenite fraction increases to reach a maximum value, which indicates the minimum degree of bainitic transformation necessary to hinder the partial transformation of the remaining austenite into martensite above room temperature. The position of this maximum depends on the bainitic holding temperature due to the influence of temperature on carbon diffusion. For longer times, a significant amount of bainite plates have grown into the austenite grains leading to a reduction in the austenite fraction with time. A second parameter that affects the austenite fraction at room temperature is the aluminum content. Aluminum increases the driving force of the bainitic transformation and retards the cementite formation during the bainitic holding step [5]. As shown in Fig. 3.2, the austenite fraction decreases with the aluminum content due to a reduced degree of bainite formation. Consequently, a lower carbon enrichment in austenite is expected. For longer holding times, the austenite fraction seems to tend to zero. This may indicate the

possible formation of carbides in the TRIP sample with only 0.4 wt.% Al at long holding times. A higher bainitic holding temperature leads to faster bainite transformation kinetics, and therefore induces a faster austenite stabilization with a maximum point at 673 K for 1 min instead of 2 min for the Al_{0.4} sample.

3.3.2 Austenite stability below room temperature

The heat treatment leading to the highest fraction of retained austenite at room temperature ($T_{bh} = 673\text{K}$ for 2 min in Al_{1.8}) was selected as base material to study the thermal stability of the retained austenite at lower temperatures. For comparison, the bainitic holding temperature was varied from 673 to 623 K for a fixed holding time of 2 min for both chemical compositions. Fig. 3.3a and b shows the austenite fraction as a function of the temperature during cooling down to 100 K. In all cases, the austenite fraction decreases during the cooling process, what indicates that part of the metastable austenite has transformed into martensite. The transformation starts at 250-275 K irrespective of the bainitic holding temperature and the chemical composition, and stops in the temperature range of 120-150 K. As expected, the austenite fraction does not change any further upon heating the material back to room temperature. An austenite fraction of 1.4% transforms thermally into martensite in the Al_{0.4} sample for all bainitic holding temperatures, while the transformed austenite fraction is around 2.3% in the Al_{1.8} sample. The bainitic temperature turns out to have a weak influence on the austenite stability when varied from 623 to 673 K, only on the initial austenite fraction before cooling. Moreover, a fraction of the initial metastable austenite grains still remain untransformed at the lowest temperature of 100 K in all samples. The average austenite carbon content ($\langle x_c^\gamma \rangle$) and grain volume ($\langle V_\gamma \rangle$) have been compared before and after cooling down to 100 K using high-energy X-ray diffraction [5], see Table 3.1. These data indicate that only small grains with a high carbon content remain untransformed at 100 K.

Finally, in Fig. 3.3c and d the comparison between the results of the magnetization measurements and those of the in-situ X-ray diffraction experiment is displayed. A very satisfactory agreement is obtained between both techniques. All the curves have the same slope, what means that the transformation

behaviour is similar for all process routes for a selected chemical composition. The martensitic transformation occurs in a narrower temperature range between 150 K and 250 K for $Al_{0.4}$ sample. A higher aluminum content is found to induce a more gradual transformation of the austenite during cooling down to 100 K.

Table 3.1: Average grain volume ($\langle V_\gamma \rangle$) and carbon content ($\langle x_c^\gamma \rangle$) of austenite before and after cooling down to 100 K for both compositions, taken from ref. [5]. The width of the distribution (standard deviation) is indicated in parenthesis.

Material	$\langle V_\gamma \rangle$ (μm^3)		$\langle x_c^\gamma \rangle$ (wt.%)	
	Before	After	Before	After
$Al_{0.4}$	11.8 (6.5)	7.8 (2.9)	0.92 (0.10)	1.01 (0.16)
$Al_{1.8}$	20.9 (12.2)	11.5 (7.2)	0.81 (0.14)	1.02 (0.11)

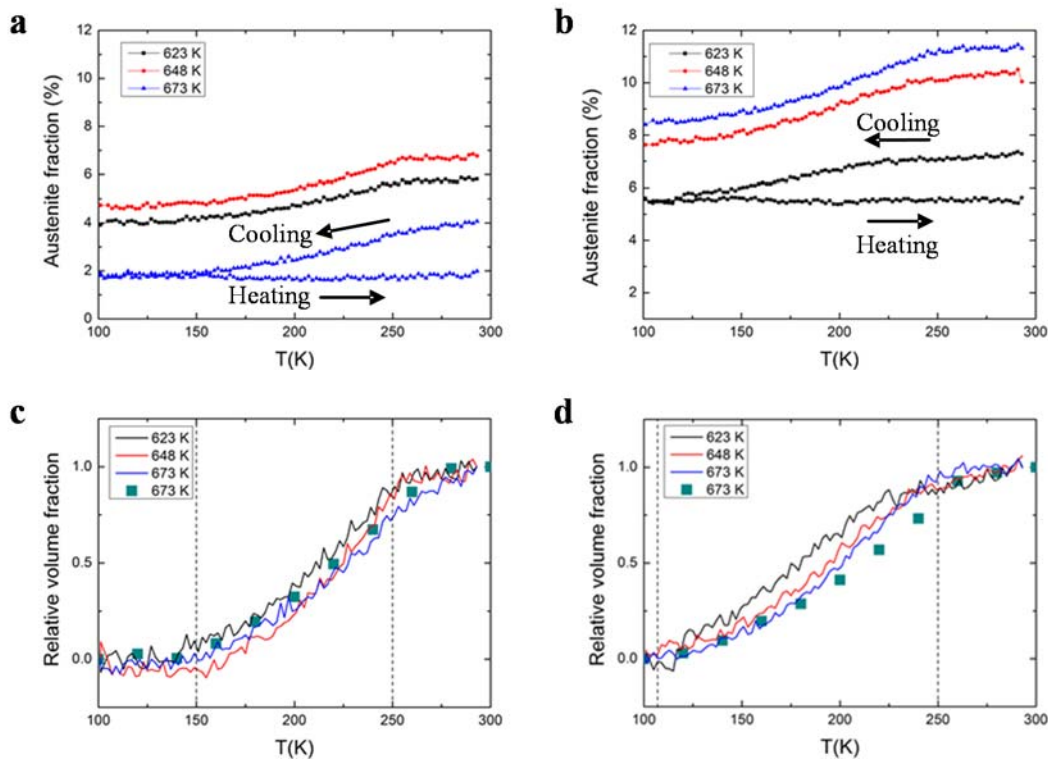


Figure 3.3: Evolution of the austenite fraction as a function of the temperature for (a) $Al_{0.4}$ and (b) $Al_{1.8}$. The relative volume fraction as a function of the temperature is shown in (c) and (d) for both chemical compositions and for a bainitic holding time of 2 min. The green dots correspond to the data obtained by in-situ X-ray diffraction (taken from ref. [7]). The dashed line indicates the temperature region where the austenite transforms into thermal martensite.

3.4 Conclusions

The thermal stability of retained austenite in two aluminum-based TRIP steels was studied by a combination of two in-situ bulk experimental techniques: magnetization measurements and high-energy X-ray diffraction. The main conclusions of the present study are:

1. The austenite fraction at room temperature increases with the bainitic holding time up to a maximum value, and then decreases slowly for longer times. If the bainitic holding temperature is lowered, this maximum is shifted towards longer holding times. A decrease in the aluminum content causes a reduction in the austenite fraction and the maximum occurs at shorter holding times.
2. The thermal stability of the retained austenite does not vary significantly with the bainitic holding temperature in the range of 623-673 K for each of the two studied TRIP steels. An increase in the aluminum content leads to a more gradual transformation of the metastable austenite.
3. A certain amount of austenite remains untransformed at 100 K in all the studied samples. These remaining austenite grains are too stable due to a high carbon content and a small grain size that gives a very low value for their martensite transformation temperature.
4. In-situ magnetization and high-energy X-ray diffraction measurements show similar results with respect to the transformation behavior of the metastable austenite below room temperature. Both techniques are successful in monitoring in-situ the martensite transformation of a small amount of retained austenite.

3.5 References

- [1] M. Militzer, *Science* 298 (2002) 975.
- [2] P.J. Jacques, *Curr. Opin. Solid State Mater. Sci.* 8 (2004) 259.
- [3] M.R. Berrahmoune, S. Berveiller, K. Inal, A. Moulin, E. Patoor, *Mater. Sci. Eng. A* 378 (2004) 304.
- [4] I.B. Timokhina, P.D. Hodgson, E.V. Pereloma, *Metall. Mater. Trans. A* 35 A (2004) 2331.
- [5] E. Jimenez-Melero, N.H. van Dijk, L. Zhao, J. Sietsma, S.E. Offerman, J.P. Wright, S. van der Zwaag, *Acta Mater.* 57 (2009) 533.
- [6] L. Zhao, N.H. van Dijk, E. Brück, J. Sietsma, S. van der Zwaag, *Mater. Sci. Eng. A* 313 (2001) 145.
- [7] N.H. van Dijk, A.M. Butt, L. Zhao, J. Sietsma, S.E. Offerman, J.P. Wright, S. van der Zwaag, *Acta Mater.* 53 (2005) 5439.



Chapter 4

Tensile experiments at variable temperatures

The stability of the retained austenite has been studied in situ in low-alloyed TRIP steels using high-energy X-ray diffraction during tensile tests at variable temperatures down to 153 K. A detailed powder diffraction analysis has been performed to probe the austenite to martensite transformation by characterizing the evolution of the phase fraction, load partitioning and texture of the constituent phases simultaneously. Our results show that at lower temperatures the mechanically induced austenite transformation is significantly enhanced and extends over a wider deformation range, resulting in a higher elongation at fracture. Low carbon content grains transform first leading to an initial increase in average carbon concentration of the remaining austenite. Later the carbon content saturates while the austenite still continues to transform. In the elastic regime the probed $\{hkl\}$ planes develop different strains reflecting the elastic anisotropy of the constituent phases. The observed texture evolution indicates that the austenite grains oriented with the $\{200\}$ along the loading direction are transformed preferentially as they show the highest resolved shear stress. For increasing degrees of plastic deformation the combined preferential transformation and grain rotation results in the standard deformation texture for austenite with the $\{111\}$ component along the loading direction. The mechanical stability of retained austenite in TRIP steel is found to be a complex interplay between carbon concentration in the austenite, grain orientation, load partitioning and temperature.

4.1 Introduction

Low-alloyed TRansformation Induced Plasticity (TRIP) steels were developed in the late 80s [1-4] and have attracted significant interest for automotive applications due to their outstanding combination of

high strength and formability [5-7]. A typical TRIP steel microstructure contains three phases at room temperature: ferrite, bainite and metastable austenite [8,9]. The remarkable mechanical properties of this material are attributed to the multiphase microstructure as well as to the transformation of the soft metastable austenite phase into the hard martensite phase upon activation by mechanical and/or thermal stimuli. This phenomenon, called the TRIP effect, increases the work-hardening rate during plastic deformation and delays necking [10,11].

A lot of effort has been devoted in recent years to maximize and tune the retention of austenite at room temperature in order to enhance the TRIP effect [12-15]. In order to create a sufficient amount of retained austenite in the TRIP microstructure, a three step heat treatment (intercritical annealing, bainitic holding and finally quenching to room temperature) is imposed [16]. This heat treatment is only effective if a sufficient concentration of alloying elements (such as Si, Al and P) retarding the cementite formation during the bainitic holding treatment is present [17,18]. An optimized composition and heat treatment leads to a retained austenite fraction of 10-15%. The carbon concentration of the retained austenite is about 6-9 times the nominal carbon concentration, but varies from grain to grain [19-21].

In previous in-situ studies the average retained austenite behavior was either studied as a function of the undercooling (defining the thermal stability) [22-24] or as a function of the applied load at room temperature (defining the mechanical stability) [25-32]. In these studies some attention was paid to the behavior of the non-transforming ferritic phase as well. These experimental results led to the development of micro-mechanical models for the TRIP multiphase microstructure [33-36]. An accurate prediction of the material's mechanical response at variable temperatures requires detailed knowledge about the interplay between the transformation behavior, the local load redistribution between the phases, the texture evolution and the deformation behavior of the non-transforming ferritic matrix as a function of both temperature and uniaxial load.

Recent advances at synchrotron radiation sources have provided material scientists with intense high-energy X-ray beams of micron dimensions that are a valuable tool for in-situ studies during the thermo-mechanical processing of advanced engineering materials [37]. In our previous synchrotron X-ray

diffraction studies we have probed the austenite transformation behavior in the bulk TRIP microstructure during deformation at room temperature [38] and during cooling down to 100 K [21,24,39,40]. We found that the austenite stability depends on both the local carbon content and the grain size. In this work, a complete in-situ characterization of the combined thermal and mechanical stability of the retained austenite has been performed by high energy synchrotron X-ray diffraction (XRD) during temperature-dependent tensile tests. The interplay between tensile deformation, the orientation-dependent austenite to martensite transformation and grain rotation has been analyzed by a Rietveld refinement of the diffraction data characterizing the relevant phases and their textures simultaneously.

4.2 Experimental methods

4.2.1 Sample preparation

The chemical composition of the studied TRIP steel is shown in Table 4.1. Cylindrical dog-bone tensile specimens with a gauge length of 10 mm and a diameter of 1 mm were machined from hot rolled sheet material. The cylindrical axis of the samples was chosen parallel to the rolling direction (RD). A mark parallel to the normal direction of the sheet material was made on the top part of the cylindrical sample in order to keep track of the sample orientation.

Table 4.1: *Chemical composition of the studied samples in wt.% with balance Fe.*

C	Mn	Si	Al	P
0.218	1.539	0.267	1.75	0.018

First, the samples were annealed in a salt bath for 30 min at an intercritical temperature of 1143 K in order to obtain equal fractions of austenite and ferrite. Then the samples were quenched in a second salt bath to a temperature of 673 K and held for 2 min. During this holding time part of the intercritical austenite transformed into bainite and the remaining austenite was enriched in carbon. The carbon-enriched austenite remained in a metastable state after a final water quench to room temperature. This

heat treatment yielded a multiphase microstructure composed of ferrite (α), bainite (α_b) and metastable austenite (γ), as shown in the optical micrograph of Fig. 4.1.

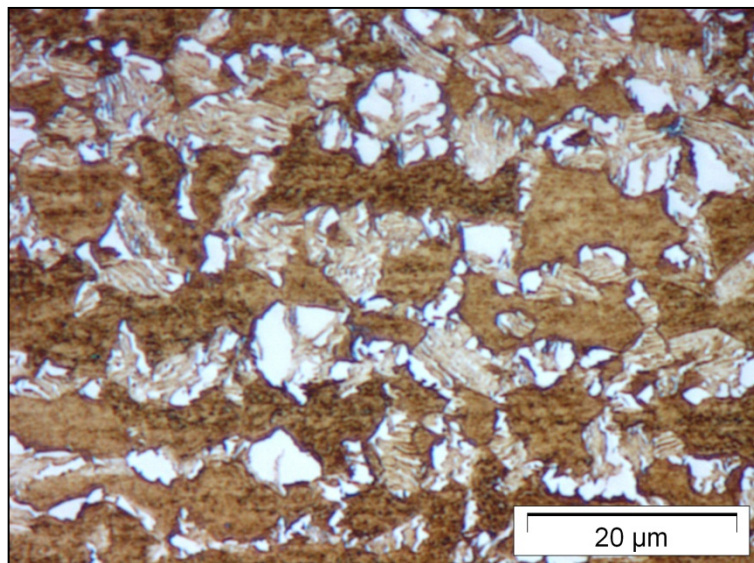


Figure 4.1: *Optical micrograph of the low-alloyed TRIP steel (etched by LePera). The room temperature multiphase microstructure contains a metastable austenite phase (white) within a matrix of ferrite (dark brown) and bainite (light brown) phases.*

4.2.2 In-situ high-energy X-ray diffraction

The in-situ XRD experiments were performed at the 3D X-ray diffraction microscope at the ID11 beam line of the European Synchrotron Radiation Facility (Grenoble, France). Fig. 4.2 shows the experimental setup used for the experiments. A monochromatic X-ray beam of 88 keV (wavelength of 0.141 Å) and a beam size of 100 x 100 μm² illuminated the cylindrical sample. For these high-energy X rays the absorption is relatively small making it possible to study even 1 mm thick samples in transmission geometry. The diffracted beam was recorded on a two dimensional CCD detector (FRELON) [41] placed behind the sample. The sample was continuously rotated around the cylindrical axis perpendicular to the X-ray beam in steps of $\Delta\omega = 0.25^\circ$ covering an angular range of 84°. During each rotation step a 2D diffraction pattern was continuously recorded using an exposure time of 0.2 s. The instrument parameters of the 3D X-ray diffraction microscope were determined using a CeO₂ calibrant (NIST SRM 674b).

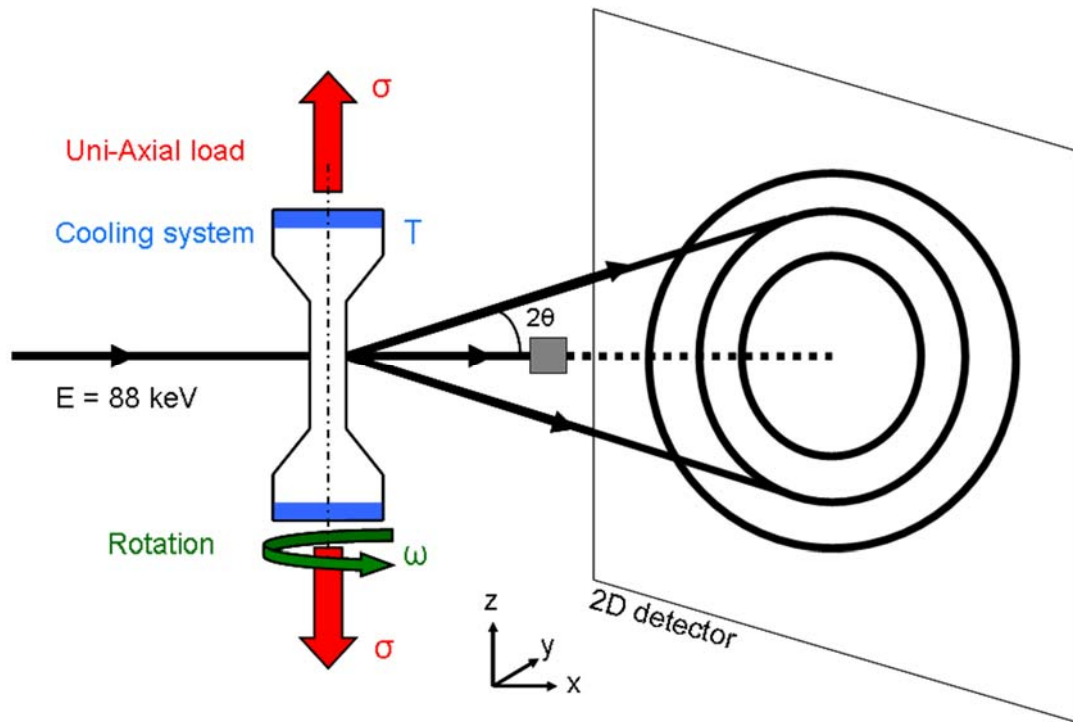


Figure 4.2: Schematic representation of the experimental setup used for the high-energy microbeam X-ray diffraction experiments on low-alloyed TRIP steels. The sample is under a tensile stress (σ) and cooled from both ends. During exposure the sample was continuously rotated around the vertical axis.

To study the mechanical stability of the retained austenite, the sample was mounted on a 2-kN micro tensile tester placed on a translation table that provided alignment of the sample in three directions with respect to the X-ray beam and ω rotation along the cylindrical axis of the sample (the loading direction was along the sample axis). The samples were aligned with the top mark parallel to the frame of the tensile tester. For each deformation step, the strain was held constant during a complete set of measurements for the full ω range. The mechanical stability of the austenite phase was studied at selected temperatures of 293, 213 and 153 K. The sample was cooled via the grips of the tensile tester by a flow of cold N_2 gas. During cooling additional XRD patterns were recorded every 10 K. The temperature was regulated by a temperature controller (Oxford Instruments). The tester and cooling system were placed in a borosilicate glass dome put under vacuum (10^{-5} mbar). Possible variations in sample-detector distance during deformation were checked by analyzing of the X-ray diffraction pattern of a calibrant placed on the sample surface.

4.2.3 Data analysis

The measured data consisted of a series of two-dimensional diffraction patterns as a function of temperature, sample elongation and ω -angle. The two-dimensional diffraction patterns for the complete ω range covered in this experiment were summed. Afterwards, an integration over the azimuthal angles at constant scattering angle was performed using the FIT2D software package [42] to obtain the corresponding one-dimensional diffraction patterns. A Rietveld refinement of the resulting one-dimensional X-ray diffraction patterns was performed using the Fullprof package [43] in order to determine the phase fraction and lattice parameter of the constituent phases as a function of the macroscopic strain. Fig. 4.3 shows two examples of the two-dimensional X-ray diffraction patterns with the corresponding one-dimensional patterns analyzed by the Rietveld method before and after applying a load. Deformation leads to a reduction in intensity for the austenite peaks, and an increase in the diffraction peaks from the ferritic matrix.

In addition to the study of the average phase behavior, we also studied the change in lattice parameter of the constituent phases oriented along and perpendicular to the loading direction. The evolution of these two families of grains has been determined by studying a specific angular section of 15 degrees on the detector. A mask has been generated to obtain the one-dimensional pattern for these zones of the two-dimensional patterns. A fit of individual reflections to a pseudo-Voigt profile function was used in order to study the stress partitioning between subsets of grains having specific $\{hkl\}$ plane normals oriented along and perpendicular to the loading direction [44].

A texture analysis has been performed using the MAUD software [45] to monitor the evolution of the preferred $\{hkl\}$ plane orientation with respect to the rolling (RD), normal (ND) and transverse (TD) sample directions. For each elongation step, 16 individual two-dimensional patterns were obtained by summing the measured data over a ω range of 5° . These summed patterns were then integrated over 5° of the azimuth angle. The 16×72 resulting 1D patterns were analyzed by the Rietveld method using MAUD and the E-WIMV algorithm [46] for the texture refinement.

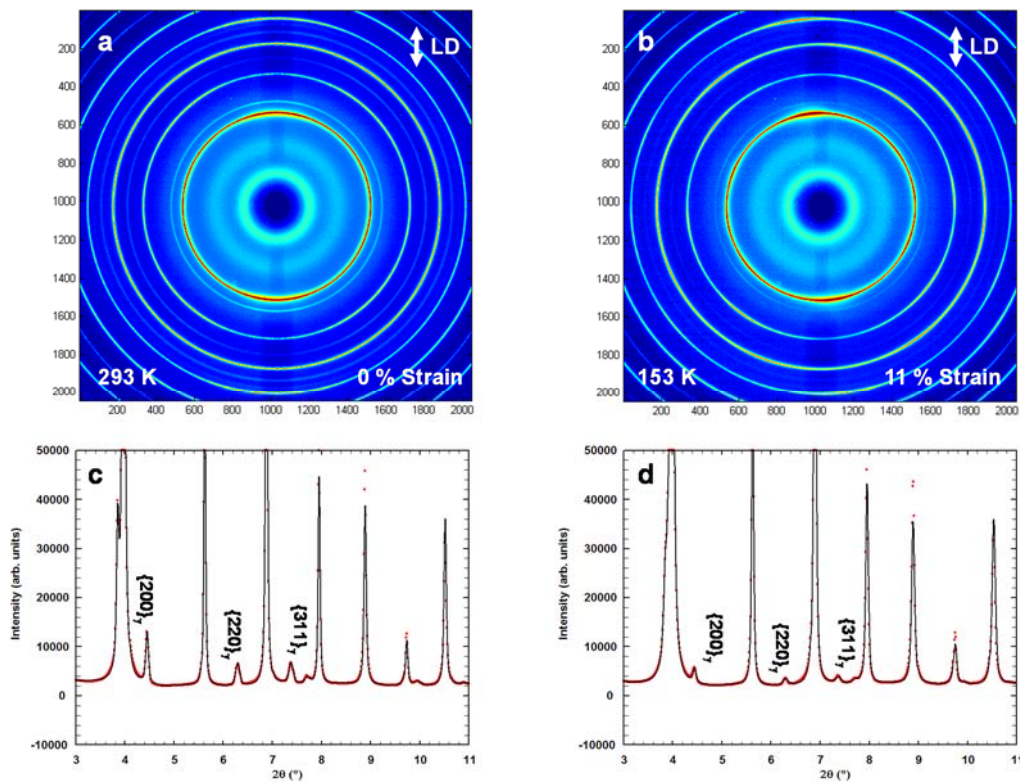


Figure 4.3: Two-dimensional X-ray diffraction patterns at (a) no strain and (b) the ultimate tensile strength (UTS). These patterns have been obtained by summing all the measured patterns for the whole ω -range used in the experiments. The loading direction is indicated in the figure (LD). The 2D patterns have been subsequently integrated over the azimuth angles to obtain the one-dimensional X-ray patterns as a function of the scattering angle at (c) no strain and (d) the ultimate tensile strength. The corresponding Rietveld refinement of the one-dimensional X-ray patterns is shown at the different strain stages.

4.3 Results and discussion

4.3.1 Macroscopic behaviour

Fig. 4.4a shows the macroscopic (engineering) stress-strain curve of the low-alloyed TRIP steel measured step-wise at a temperature of 293, 213 and 153 K. Each data point on the curves represents a set of X-ray diffraction measurements for the covered ω -rotation range while the macroscopic strain is held constant. We recorded the diffraction patterns for a series of elongation steps up to the ultimate tensile strength. Table 4.2 contains the relevant parameters that characterize the mechanical behavior of the studied TRIP steel samples at the three selected temperatures. Both the yield stress and the ultimate tensile strength show an increase of more than 200 MPa when cooling the sample from 293 to 153 K. The uniform elongation also shows a significant increase when lowering the temperature, taking a value of about 6.6% at 293 K and 11% at the lowest temperature of the experiments. This effect does not

agree with the expected temperature-dependent mechanical behaviour of metals and multiphase alloys where plastic deformation takes place primarily by dislocation glide and dislocation interactions [47]. The reverse phenomenon observed in these TRIP steel samples with respect to the variation of the uniform elongation with temperature may be ascribed to the presence of the TRIP effect.

Table 4.2: *Characteristic values for the macroscopic mechanical response of the TRIP steel at three selected temperatures.*

Temperature (K)	Yield Stress (MPa)	Ultimate Tensile Strength (MPa)	Uniform Elongation (%)	Elongation at fracture (%)
293	206	519	6.61	8.14
213	405	660	9.28	11.53
153	471	754	10.96	14.42

4.3.2 Evolution of the austenite phase fraction

The austenite phase fraction was derived from the Rietveld refinement of the 1D diffraction patterns at the selected deformation steps and temperatures, assuming the presence of the austenite phase within a ferritic matrix (consisting of ferrite, bainite, and the formed martensite). In previous diffraction studies [24,31,32] an attempt has been made to separate the phase contributions within the ferritic matrix. For our steels the formed martensite shows no indication of a tetragonal distortion and is indistinguishable from ferrite and bainite (see also [38-40]). Fig. 4.3c and 4.3d show the fitted pattern of the original material and for the ultimate tensile strength at 153 K, respectively. The austenite reflections show a significant reduction in intensity caused by the combined effect of deformation and cooling.

Fig. 4.4b shows the austenite fraction as a function of the macroscopic strain at the selected temperatures. The difference in the initial austenite fraction at the selected temperatures is caused by the austenite-to-martensite transformation during cooling. The austenite fraction decreases progressively with increasing strain due to the mechanically induced austenite transformation. At all studied temperatures the austenite starts to transform well before the macroscopic yield stress is reached. The stability of the retained austenite phase strongly depends on the chemical composition and the applied heat treatment. It was found that for short bainitic holding times the least stable

austenite grains can be destabilized by cooling [39] or by adding strain energy in the elastic regime [38]. At room temperature the austenite fraction decreases continuously (by maximum 1.8 %) for strains up to 2.5% and then remains roughly constant until fracture. At lower temperatures the transformation continues until fracture. As indicated in Table 4.3, the amount of austenite transformed by deformation is 4.3% at 213 K and 4.5% at 153 K. At fracture a finite amount of austenite is still present and cannot be transformed mechanically for these experimental conditions. The increase in the austenite fraction transformed by deformation at lower temperatures shows a strong correlation to the increase in maximum elongation. The TRIP effect clearly becomes more effective at lower temperatures.

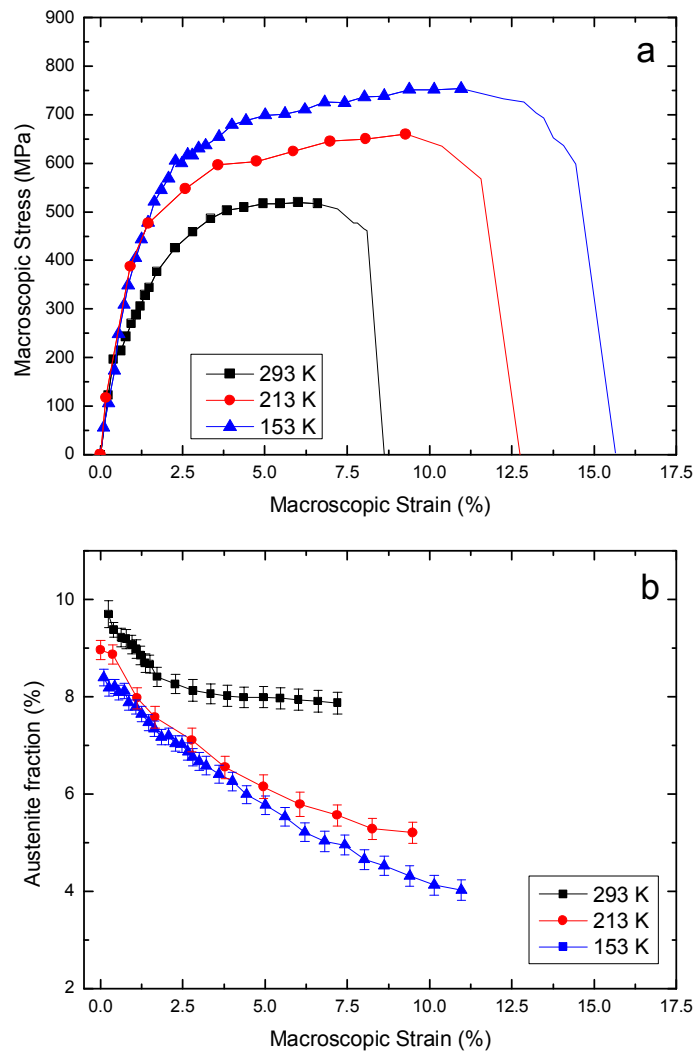


Figure 4.4: (a) Macroscopic (engineering) stress-strain curves of TRIP steel measured step-wise during the *in situ* X-ray diffraction experiments at temperatures of 293, 213 and 153 K. (b) Austenite fraction as a function of the macroscopic strain for the different temperatures. The variations in the initial austenite fraction are due to the transformation during cooling.

This observation is consistent with recent temperature-dependent studies on the austenite stability above [48] and below [49] room temperature.

Prior to the deformation at 213 and 153 K the material was cooled from room temperature. In order to evaluate the austenite stability as a function of temperature a diffraction pattern was collected every 10 K during the cooling process. Fig. 4.5 shows the austenite fraction as a function of temperature during continuous cooling from room temperature to 153 K. The austenite fraction decreases gradually when the temperature is lowered and reached a constant value below 180 K. This is consistent with earlier observations [24]. After cooling 0.4% of austenite has transformed at 213 K and 1.1% at 153 K (see Table 4.3).

Table 4.3: Austenite fraction for the TRIP steel measured for different strain stages at three selected temperatures.

Temperature (K)	Initial Austenite fraction (%)	Austenite fraction after cooling (%)	Austenite fraction at fracture (%)
293	9.8(3)	-	8.0(2)
213	9.4(2)	9.0(2)	4.7(2)
153	9.5(2)	8.4(2)	3.9(2)

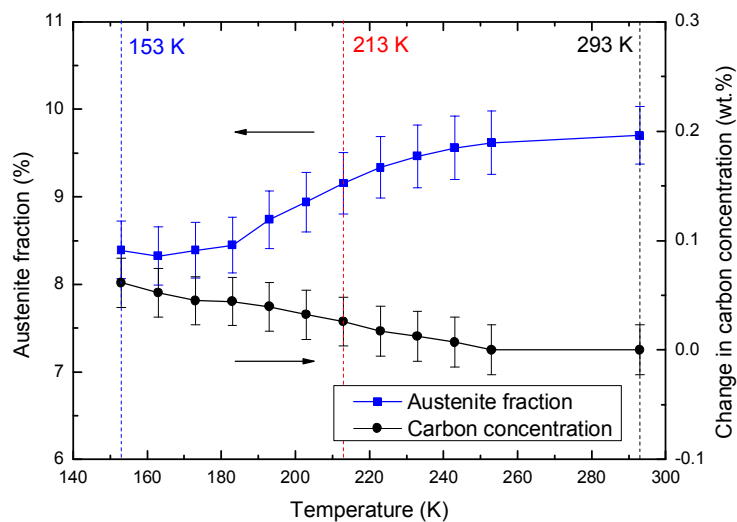


Figure 4.5: Phase fraction and carbon enrichment of the austenite as a function of the temperature during cooling from 293 to 153 K. The increase in the average carbon content in the remaining austenite is caused by the preferred transformation of the less stable austenite grains.

4.3.3 Relative change in lattice parameter

In addition to the austenite phase fraction, we can simultaneously analyse the carbon enrichment of the remaining austenite from the relative change in lattice parameter during cooling. At room temperature, the lattice parameter of austenite depends on the chemical composition according to [24,50]:

$$a_\gamma = 3.556 + 0.0453x_c + 0.00095x_{Mn} + 0.0056x_{Al} \quad (1)$$

where a_γ is the austenite lattice parameter in Å and x_c , x_{Mn} and x_{Al} are the alloying concentrations in wt.%. The presence of Si and P is considered to have a negligible effect on the lattice parameter of austenite. Using this equation and the measured initial lattice parameter, the carbon content at room temperature amounts to 1.31(2) wt.%. During cooling the austenite lattice parameter is affected by the thermal contraction. Below room temperature the thermal contraction of austenite shows a coefficient of thermal expansion that linearly depends on temperature [21]:

$$\frac{a(T) - a(T_0)}{a(T_0)} = \int_{T_0}^T \alpha(T) dT \quad (2)$$

where $a(T_0)$ is the lattice parameter at room temperature ($T_0 = 293$ K) and $\alpha(T)$ is the coefficient of the thermal expansion. The thermal expansion at $T = 300$ K is equal to $16.0 \times 10^{-6} \text{ K}^{-1}$ for austenite and $11.7 \times 10^{-6} \text{ K}^{-1}$ for ferrite [24].

In Fig. 4.5 the increase in average carbon concentration in the untransformed austenite is shown as a function of temperature during cooling. These values have been obtained from the relative change in lattice parameter corrected for the thermal contraction. The average carbon concentration increases during cooling as only the least stable grains, with a lower carbon content, transform into martensite. According to Andrews' law [51] the martensite start temperature M_s depends linearly on the carbon concentration x_c in the austenite phase:

$$M_s = M_0 - Ax_c \quad (3)$$

where M_0 and A are constants.

In our previous XRD experiments on the stability of individual austenite grains [39] it was found that M_s also depends on the austenite grain size V_γ : $M_0 = M_{s0} - BV_\gamma^{-\frac{1}{3}}$, where M_{s0} and B are constants. For our composition the experimental constants are determined to be: $M_{s0} = 702$ K, $A = 425$ K/wt.% and $B = 475$ $\mu\text{m}\cdot\text{K}$. As the least stable grains will transform first, the average carbon concentration of the remaining austenitic fraction is higher at low temperature.

The relative change in lattice parameter due to deformation originates from the elastic strain and the carbon enrichment of the austenite resulting from the mechanically induced martensite transformation. The elastic strains have been determined by the lattice strain ε for each phase [27]:

$$\varepsilon = \frac{a - a_0}{a_0} \quad (4)$$

where a_0 is the lattice parameter of the considering phase at zero deformation and a the lattice parameter at a given deformation. In Fig. 4.6 the development of the relative change in lattice parameters is shown as a function of the applied macroscopic stress. During deformation, the load is distributed between the austenite and the ferritic matrix. In each phase the load distribution depends on the grain orientation.

The grains with their plane normal oriented along the loading direction (axial) will be in a tensile condition and the ones with their plane normal perpendicular to the loading direction (radial) in compression. To distinguish the response of the axial and radial orientations for the diffracting planes we have selected the two relevant parts of the recorded 2D diffraction patterns (see experimental section for details). Fig. 4.6 shows the relative change in lattice parameter for austenite and ferrite at the selected temperatures. For austenite the relative change in lattice parameter originates from two contributions: the lattice strain and a change in average carbon content caused by the mechanically induced martensite formation. By comparing the relative change in lattice for the axial and radial orientations we can separate both contributions.

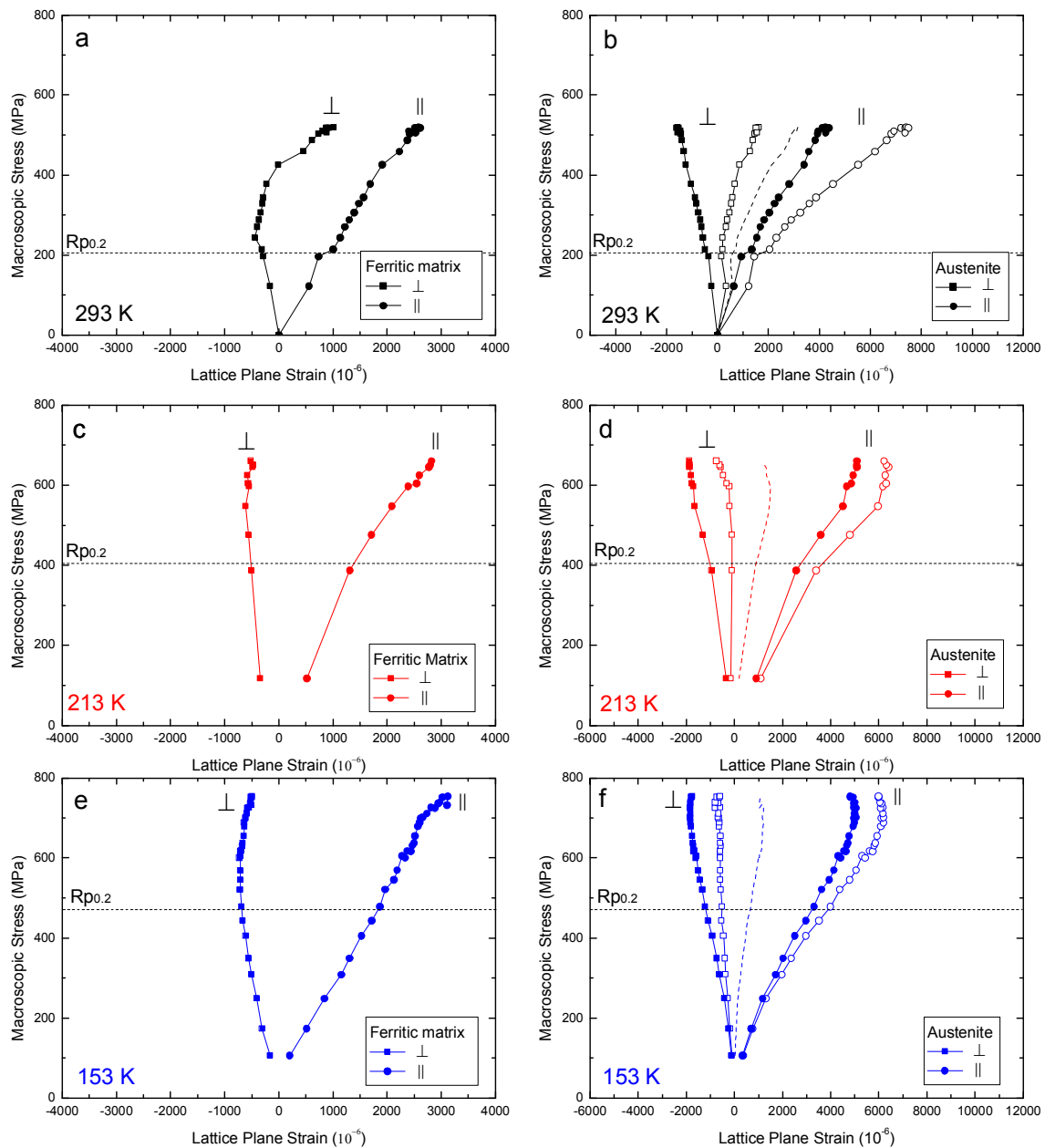


Figure 4.6: Lattice plane strain of the ferritic matrix and austenite (close symbols) as a function of the macroscopic stress for selected grain orientations at temperatures of 293, 213 and 153 K. For the axial orientation (||) the plane normal is parallel to the loading direction while for the radial (\perp) direction it is perpendicular to the loading direction. For austenite the open symbols correspond to the relative change in lattice parameter ($\Delta a/a$). This change is due to the elastic strains and the carbon enrichment. Both contributions have been separated by using the Poisson ratio for austenite (see text). The effect of carbon enrichment (ϵ_C) is indicated by the dashed line. The horizontal dotted-lines correspond to the macroscopic yield point ($R_{p0.2}$).

The carbon enrichment has a isotropic effect, while the orientation dependence for the elastic strains is defined by the Poisson ratio $\nu = 0.367$ [35,52]. The relative change in lattice parameter due to the

carbon enrichment ε_C can now be estimated by $\varepsilon_C = [(\Delta a_{\perp} / a) + \nu(\Delta a_{\parallel} / a)] / (1 + \nu)$, where $\Delta a_{\perp} / a$ and $\Delta a_{\parallel} / a$ are the relative changes in lattice parameter for the radial and axial orientations, respectively. The resulting lattice plane strain is now obtained by subtracting ε_C from the relative change in lattice parameter for the axial and radial orientations. In Fig. 4.6 the resulting value of ε_C is indicated by the dashed line and the lattice plane strains by the closed symbols.

Fig. 4.7 shows carbon enrichment Δx_C in the austenite obtained from the relative change in lattice parameter ε_C and the corresponding the austenite fraction as a function of the macroscopic strain at the selected temperatures. The carbon enrichment due to mechanically induced martensite formation is lower at 153 K than at 293 K. As listed in Table 4.4, the carbon enrichment varies from $\Delta x_C = 0.24$ wt.% for 1.8% transformed austenite at 293 K to $\Delta x_C = 0.16$ wt.% for 4.5% transformed austenite at 153 K. The lower carbon enrichment during deformation at lower temperatures may be due to the carbon enrichment during the prior cooling step (Fig. 4.5). Larger amount of austenite transformation did not result in a higher carbon enrichment. Even though we observe a continuous austenite transformation up to the maximum uniform elongation for temperatures of 213 and 153 K no further carbon enrichment is observed for macroscopic strains beyond about 2.5%.

In Fig. 4.6a and 4.6b the obtained lattice strain is shown for austenite and the ferritic matrix at room temperature. Below the macroscopic yield point ($R_{p0.2}$), the lattice plane strains of austenite and ferritic matrix evolve roughly linearly with the stress. At room temperature austenite shows a Young's modulus of $E_{\gamma} = 167$ GPa, while for the ferritic matrix a value of $E_{\alpha} = 225$ GPa is obtained. In Fig. 4.6c to 4.6f the obtained lattice strain is shown for austenite and the ferritic matrix below room temperature. At the lowest temperature of 153 K the Young's modulus of austenite and the ferritic matrix increases to $E_{\gamma} = 185$ GPa and $E_{\alpha} = 233$ GPa, respectively. In Table 4.5 the temperature dependence of the Young's modulus is reported for both phases. Based on the reported elastic constants at room temperature [35] values of $E_{\gamma} = 164$ GPa and $E_{\alpha} = 134$ GPa are predicted for fcc and bcc iron, respectively.

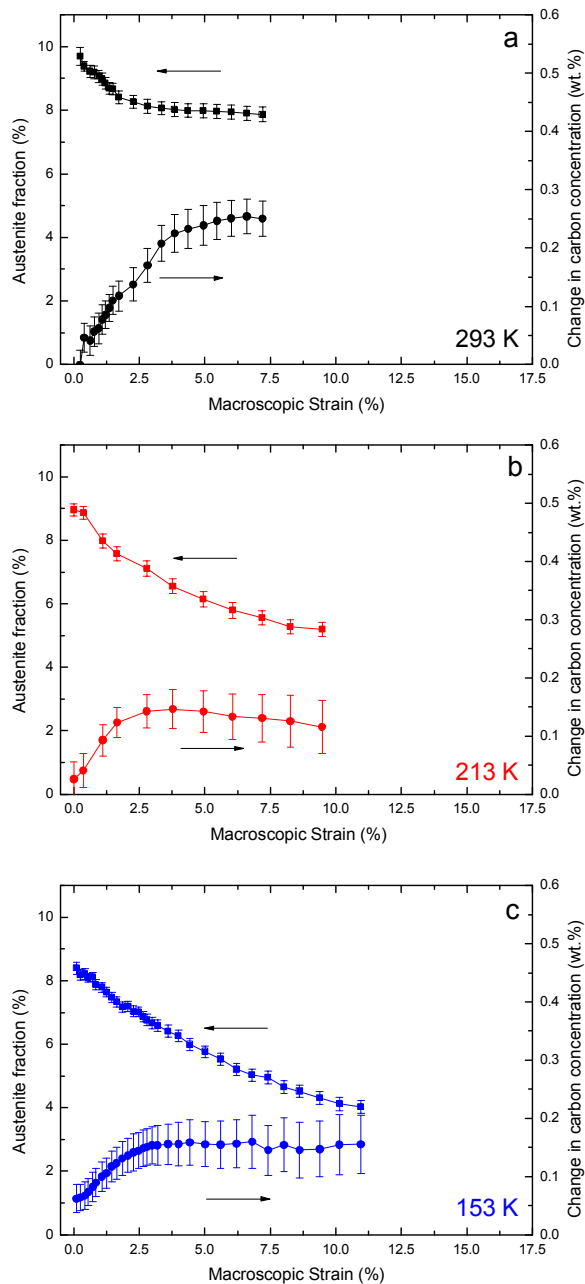


Figure 4.7: Austenite fraction and carbon enrichment as a function of the macroscopic strain at a constant temperature of 293, 213 and 153 K. The initial carbon concentration corresponds to the value after cooling.

A good agreement is observed for austenite, while the difference for the ferritic matrix probably originates from the presence of bainite and the newly formed martensite. For bcc iron the temperature dependence of the elastic constants [52] indicates an increase in Young's modulus of about 5% for cooling to 153 K in line with the observed behavior. In the plastic regime the load is redistributed over the austenite and the ferritic matrix, which is mainly a result of the austenite transformation. The deviation from linearity in the stress strain curves is observed at all temperatures, but more pronounced below room temperature. This is probably due to the enhanced TRIP effect at low temperatures.

Table 4.4: *Change in the carbon concentration of austenite before and after deformation at three selected temperatures. The initial carbon content in austenite at room temperature is 1.31(2) wt.%.*

Temperature (K)	Change in carbon concentration after cooling (wt. %)	Change in carbon concentration at fracture (wt. %)
293	-	0.24(3)
213	0.03(2)	0.12(4)
153	0.06(2)	0.16(5)

Table 4.5: *Young's modulus of the ferritic matrix and austenite at selected temperatures.*

Temperature (K)	Ferritic Matrix (GPa)	Austenite (GPa)
293	225(31)	167(28)
153	233(6)	185(7)

4.3.4 Lattice plane strain for individual $\{hkl\}$ planes

The high-energy X-ray diffraction experiments allow us to follow not only the load partitioning between the phases and their main orientations, but also for the specific $\{hkl\}$ planes of each phase. In this section, the lattice plane strain of grains having specific $\{hkl\}$ planes oriented axial and radial to the tensile direction are analyzed independently. In Fig. 4.8 the strain of individual $\{hkl\}$ planes is shown for each subset of grains at the studied temperatures. The plane strain ε_{hkl} is defined as:

$$\varepsilon_{hkl} = \frac{d_{hkl} - d_{hkl}^0}{d_{hkl}^0} \quad (5)$$

where d_{hkl} is the d -spacing of the diffracting $\{hkl\}$ plane and d_{hkl}^0 its unstrained value. The curves of the plane strain for austenite have been corrected for the carbon enrichment obtained from Fig. 4.6. Significant variations in the stiffness of all the $\{hkl\}$ planes are observed for the radial and axial orientations.

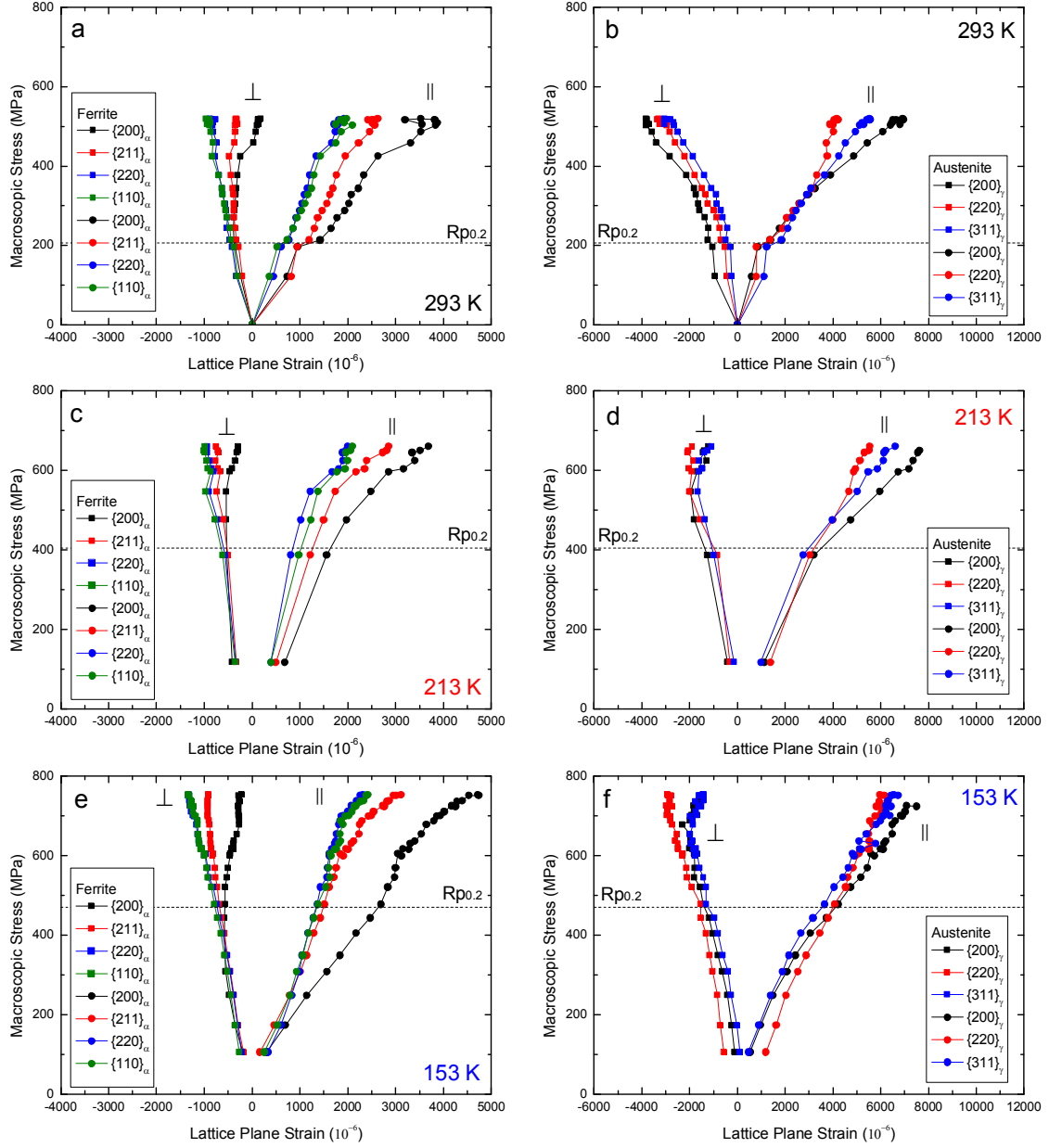


Figure 4.8: Austenite fraction and carbon enrichment as a function of the macroscopic strain at a constant temperature of 293, 213 and 153 K. The initial carbon concentration corresponds to the value after cooling.

For a cubic single crystal the orientation-dependent variation in elastic strain caused by a tensile stress

σ is characterized by the cubic elastic anisotropy factor A_{hkl} [53]:

$$A_{hkl} = \frac{h^2k^2 + k^2l^2 + l^2h^2}{(h^2 + h^2 + l^2)^2} \quad (6)$$

where h, k, l are the Miller indices of the diffracting plane. The elastic strain for a family of grains with a

plane normal $\langle hkl \rangle$ aligned along (\parallel) or perpendicular (\perp) to the loading axis is given by [54]:

$$\frac{\varepsilon_{hkl}^{\parallel}}{\sigma} = S_{11} - 2 \left[S_{11} - S_{12} - \frac{1}{2} S_{44} \right] A_{hkl} \quad (7)$$

$$\frac{\varepsilon_{hkl}^{\perp}}{\sigma} = S_{12} + \left[S_{11} - S_{12} - \frac{1}{2} S_{44} \right] A_{hkl} \quad (8)$$

where S_{ij} are the elastic compliances. For planes aligned with the plane normal along the loading axis a greater value of A_{hkl} implies a greater stiffness $E_{hkl} = \sigma / \varepsilon_{hkl}^{\parallel}$. Hence, for the austenite phase the $\langle 200 \rangle$ direction is the most compliant crystallographic direction in the axial loading direction with $A_{200} < A_{311} < A_{220}$ ($A_{200} = 0.00$, $A_{311} = 0.16$, $A_{220} = 0.25$) and therefore $E_{200}^{\gamma} < E_{311}^{\gamma} < E_{220}^{\gamma}$. For ferrite the $\langle 200 \rangle$ directions are also the most compliant crystallographic directions in the axial loading direction with $A_{200} < A_{110} = A_{220} = A_{211}$ ($A_{200} = 0.00$, $A_{110} = A_{220} = A_{211} = 0.25$) and therefore $E_{200}^{\alpha} < E_{110}^{\alpha} = E_{220}^{\alpha} = E_{211}^{\alpha}$.

Our results shown in Fig. 4.8 confirm these predictions: along the loading direction the $\{200\}$ plane of the ferritic matrix is the most strained by the applied stress at all temperatures. A comparable strain development for the $\{110\}$, $\{220\}$ and $\{211\}$ planes of the ferritic matrix is observed up to the yield point. For austenite the lattice strain of the $\{200\}$ plane shows the fastest growth for increasing applied stress. The $\{220\}$ plane of austenite shows the weakest strain development for increasing applied stress, but demonstrates the highest initial strain at low stress levels. The Young's modulus for the individual $\{hkl\}$ planes is shown in Table 4.6 for both phases. Along the radial axis, the resulting contraction due to the axial stress also varies with the $\{hkl\}$ plane. Again the cubic anisotropy factor predicts that the stiffness of the $\{200\}$ plane is the highest for both the austenite and the ferritic matrix. The qualitative elastic response observed experimentally is well predicted by the cubic elastic anisotropy factor. However, quantitative estimates of the macroscopic hkl Young's modulus for the multiphase polycrystalline aggregate need to be obtained using a homogenization scheme of the single crystalline values [55].

Table 4.6: $\{hkl\}$ dependent Young's modulus E_{hkl} (in GPa) for the ferritic matrix and austenite at a temperature of 293 and 153 K.

Temperature (K)	Ferritic Matrix			Austenite		
	{200}	{211}	{220}	{200}	{311}	{220}
293	159(29)	183(28)	309(45)	161(36)	121(25)	160(45)
153	156(2)	268(10)	330(16)	127(7)	141(4)	145(7)

4.3.5 Austenite stability for different $\{hkl\}$ planes

Fig. 4.9 shows the relative peak intensity of the $\{hkl\}$ reflections of austenite and the ferritic matrix as a function of the macroscopic stress for grains with plane normals oriented parallel to the loading direction. For the ferritic matrix the variation in peak intensity is mainly caused by grain rotation and start around the macroscopic yield stress. For the ferritic matrix the most pronounced effect is observed for the {200} planes oriented with the plane normals along the loading.

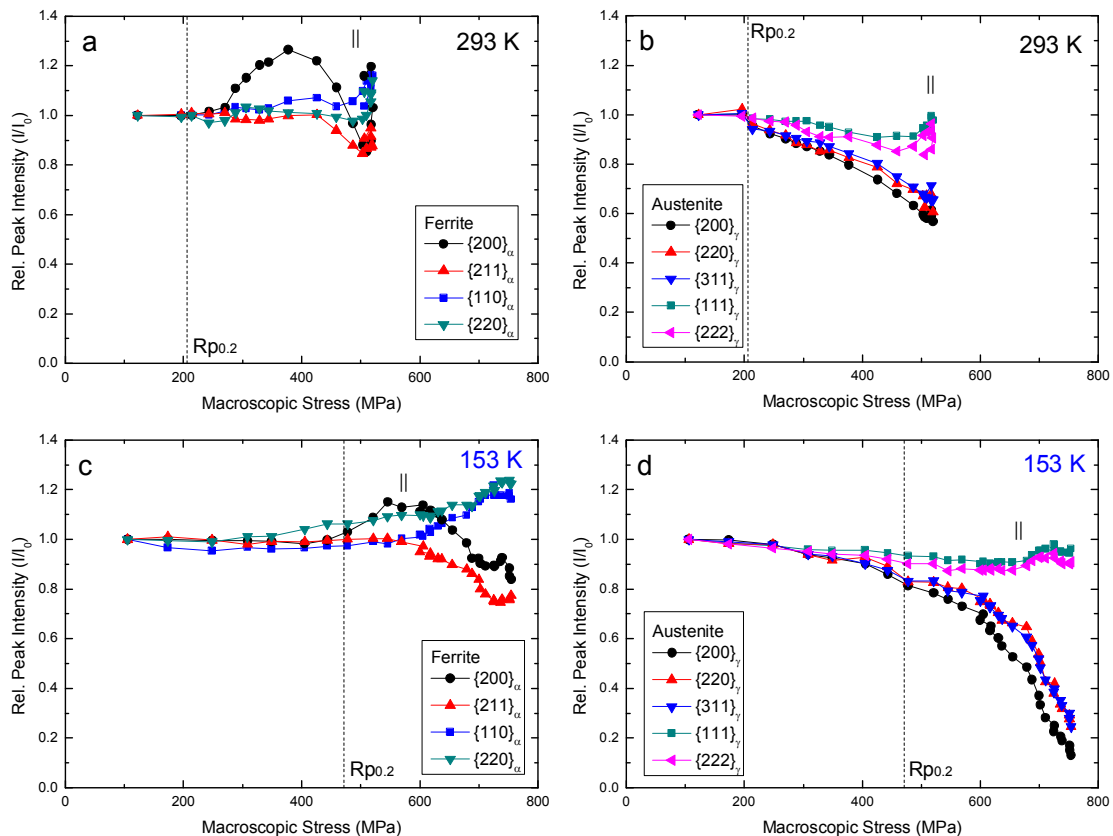


Figure 4.9: Relative peak intensity of the ferritic matrix and austenite as a function of the macroscopic stress at 293 and 153 K for the grains with a plane normal oriented along the loading direction. The vertical dotted-lines correspond to the macroscopic yield point ($R_{p0.2}$).

For the austenite phase the diffracted intensity is affected by grain orientation and the austenite transformation. The largest change in intensity is observed for the {200} orientation, while the intensity of the {*hhh*} reflection is hardly affected. Again the effect of deformation is most pronounced beyond the macroscopic yield stress, although for austenite minor variations are also observed at lower stresses. This is probably caused by the austenite transformation taking place below the macroscopic yield point. The reduction in intensity for the {200}, {220}, and {311} reflections is strongly enhanced at low temperatures. The preferential martensite transformation of the {200} austenite grains is in agreement with previous diffraction studies [31,38,56]. The orientation-dependent stability of the austenite phase is defined by the Schmid factor m , which relates the maximum resolved shear stress $\tau = m\sigma = \cos(\lambda)\cos(\phi)\sigma$ to the applied tensile stress σ , where λ is the angle between the tensile orientation and the {111} slip plane normal and ϕ the angle between the tensile orientation and the <110> slip direction. For the diffracted intensity shown in Fig. 4.9 for the grains with their plane normal oriented along the tensile direction the Schmid factor m can be determined.

The Schmid factor amounts to: $m_{\{111\}}^{\parallel} = m_{\{222\}}^{\parallel} = (2/3)/\sqrt{6} = 0.272$, $m_{\{311\}}^{\parallel} = (10/11)/\sqrt{6} = 0.371$ and $m_{\{200\}}^{\parallel} = m_{\{220\}}^{\parallel} = 1/\sqrt{6} = 0.408$ for the studied {*hkl*} austenite planes. The elastic shear strain

Gibbs free energy per unit volume corresponds to: $\Delta g_{shear} = \frac{1}{2} S_{44} \tau^2 = \frac{1}{2} S_{44} m^2 \sigma^2$. This shear strain energy suggests a stress dependence of the martensite start temperature of the form:

$$M_s(\sigma) = M_s(0) + Cm^2\sigma^2 \quad (9)$$

where $C = (S_{44}/2)(d\Delta g_v/dT)^{-1}$ is a constant and Δg_v the difference in Gibbs free energy per unit volume between austenite and martensite. The orientation dependent stability of the {*hkl*} diffraction planes is governed by the relative strength of the Schmid factor for the relevant planes. The reduced stress dependence of the {220} intensity compared to the {200} intensity is expected to be caused by the lower number of potentially active slip systems. Our proposed model considers an elastic energy

criterion for the transformation of austenite into martensite, since we experimentally observe that the transformation already starts in the elastic regime. In comparison, the Patel-Cohen model [57] considers an energy criterion for the mechanical work done by the transformation that leads to a linear stress dependence of the martensite start temperature.

4.3.6 Texture analysis

A texture analysis has been performed using the MAUD software on the constituent phases for selected macroscopic strains and temperatures. Fig. 4.10 shows the texture evolution at characteristic stages: before cooling, after cooling, close to the yield strength and at ultimate tensile strength (UTS). The grain orientation of the TRIP steel has been represented by inverse pole figures as a function of the rolling (RD), transverse (TD) and normal (ND) directions. The initial preferred orientation of the ferritic matrix is the $\{111\}\langle 110 \rangle$. For austenite there are two components: a weak $\{110\}\langle 001 \rangle$ and a strong $\{110\}\langle 111 \rangle$. Cooling the material does not significantly affect the texture. The grains do not rotate during cooling although the transformation induced by cooling can activate some grain rotations. By applying the mechanical load, the $\{111\}\langle 110 \rangle$ component of the ferritic matrix is further enhanced. In the austenite phase two types of texture evolution have been observed. The strong $\{110\}\langle 111 \rangle$ component increases, which means that the grains rotate during the loading, while the $\{110\}\langle 001 \rangle$ component tends to disappear because these austenite grains have been transformed mechanically. This is in agreement with the results of Fig. 4.8 and 4.9 where the $\{110\}\langle 001 \rangle$ component decreases by straining the TRIP steel due to transformation. At low temperature the texture evolution is more pronounced than at room temperature but shows the same characteristic behavior.

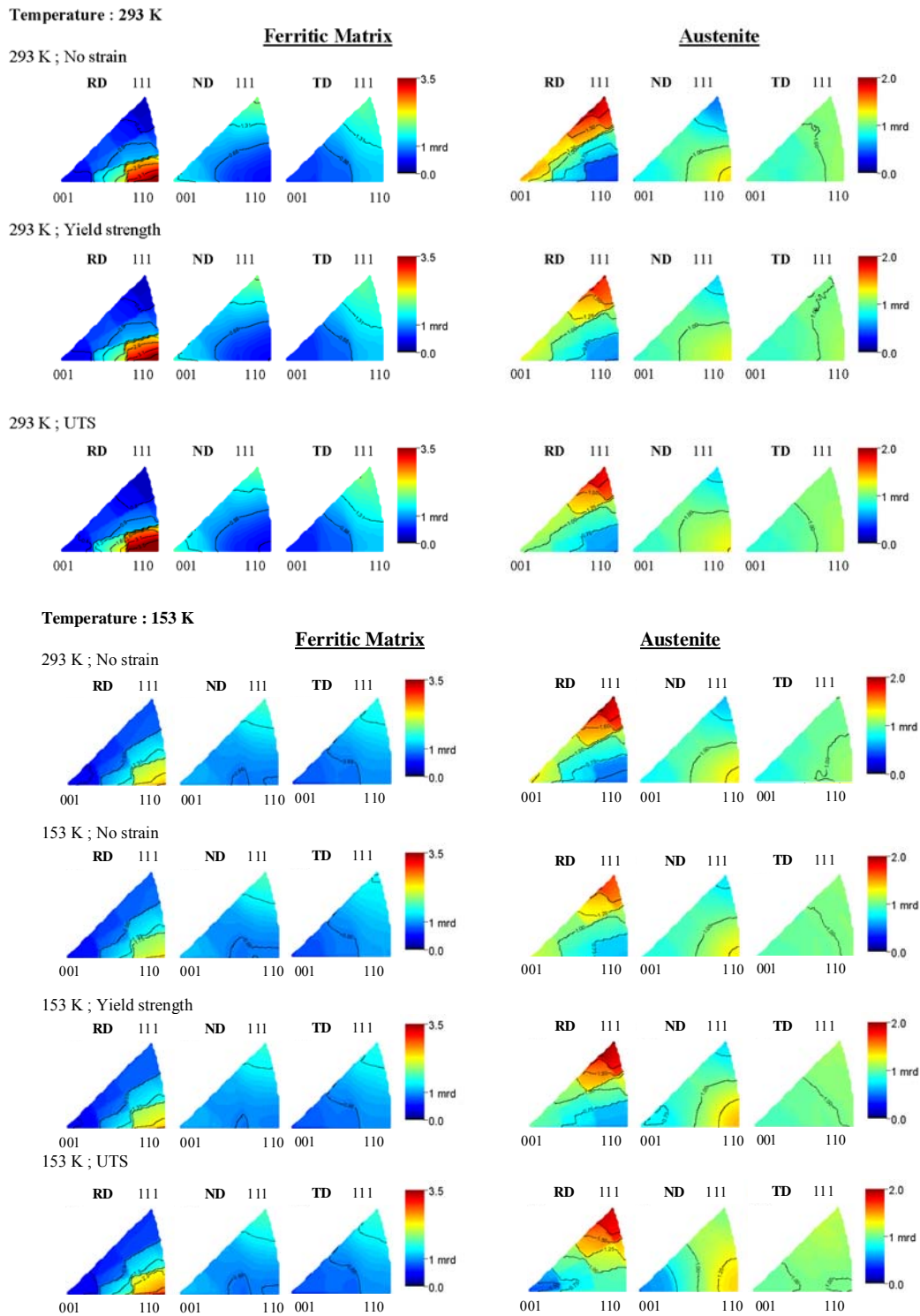


Figure 4.10: Texture evolution of the ferritic matrix and austenite represented as inverse pole figures reconstructed from the ODFs for different strain steps at a temperature of 293 K (top) and 153 K (bottom). The scale is in multiples of random distribution (mrd).

4.4 Conclusions

We have performed in-situ high-energy X-ray diffraction experiments at a synchrotron source in order to study the austenite stability in a low-alloyed TRIP steels during tensile tests at three selected temperatures. A detailed analysis of the diffraction data reveals the relevant characteristics of the temperature dependent austenite-to-martensite transformation during deformation. The main conclusions are:

1. At lower temperatures the mechanically induced austenite transformation is significantly enhanced and extends over a wider deformation range. At room temperature the austenite transformation is only observed for strains up to 2.5%, while it extends over the full deformation range at temperatures of 213 and 153 K. At lower temperatures both the ultimate tensile strength and the elongation at fracture show an increase. The higher elongation at fracture is expected to be caused by the more efficient TRIP effect for lower temperatures. At all temperatures the austenite transformation starts well below the macroscopic yield stress.
2. By selecting subsets of grains with plane normals along and perpendicular to the tensile load we can decouple the carbon enrichment in the austenite and the elastic phase strain from the derived relative change in lattice parameter during deformation. The carbon concentration in the remaining austenite due to the progressive transformation to martensite first increases but stabilizes well before the TRIP effect is depleted.
3. In the elastic regime the probed $\{hkl\}$ planes develop different strains reflecting the elastic anisotropy of the constituting phases. The Young's modulus for the $\{hkl\}$ planes has been determined at room temperature and at 153 K. At both temperatures the relative strength of the elastic strains on the $\{hkl\}$ planes is in good agreement with the predictions from the cubic elastic anisotropy factor.
4. The observed texture evolution indicates that the austenite grains oriented with the $\{200\}$ along the loading direction are transformed preferentially as they show the highest resolved shear stress. For increasing plastic deformation the combined preferential transformation and grain rotation results in the standard deformation texture for austenite with the $\{111\}$ component along the loading direction.

5. The mechanical stability of retained austenite in TRIP steel is found to be a complex interplay between carbon concentration in the austenite, grain orientation, load partitioning and temperature. A model is proposed to describe the effect of applied tensile stress on the M_s temperature.

4.5 References

- [1] Matsumura O, Sakuma Y, Takeshi H. ISIJ Int 27 (1987) 570.
- [2] Matsumura O, Sakuma Y, Takeshi H. Scr Metall 21 (1987) 1301.
- [3] Y. Sakuma, O. Matsumura, H. Takeshi, Metall. Trans. A 22 (1991) 489.
- [4] K. I. Sugimoto, N. Usui, M. Kobayashi, S. Hashimoto, ISIJ Int 32 (1992) 1311.
- [5] De Cooman BC. Curr Opin Solid State Mater Sci 8 (2004) 285.
- [6] Oliver S, Jones TB, Fournalis G. Mat Sci Tech 23 (2007) 423.
- [7] Kwon O, Lee K, Kim G, Chin KG. Mat Sci Forum 638-642 (2010) 136.
- [8] Zaefferer S, Olhert J, Bleck W. Acta Mater 52 (2004) 2765.
- [9] Timokhina IB, Hodgson PD, Pereloma EV. Metall Mater Trans A 35A (2004) 2331.
- [10] Jacques PJ, Furnémont Q, Lani F, Pardoën T, Delannay F. Acta Mater 55 (2007) 3681.
- [11] Dan WJ, Zhang WG, Li SH, Lin ZQ. Comp Mat Sci 40 (2007) 101.
- [12] Srivastava AK, Jha G, Gope N, Singh SB. Mat Charact 57 (2006) 127.
- [13] Skálová L, Divišová, Jandová. J Mat Proc Tech 175 (2006) 387.
- [14] Kammouni A, Saikaly W, Dumont M, Marteau C, Bano X, Charai A. Mat Sci Eng A 518 (2009) 89.
- [15] Chiang J, Lawrence B, Boyd JD, Pilkey AK. Mat Sci Eng A 528 (2011) 4516.
- [16] Jacques PJ. Curr Opin Solid State Mater Sci 8 (2004) 259.
- [17] Traint S, Pichler A, Hauzenberger K, Stiaszny P, Werner E. Steel Res 73 (2002) 259.
- [18] Suh DW, Park SJ, Oh CS, Kim SJ. Scripta Mater 57 (2007) 1097.
- [19] Jacques PJ, Girault E, Harlet Ph, Delannay F. ISIJ Int 41 (2001) 1061.
- [20] Jun HJ, Park SH, Choi SD, Park CG. Mat Sci Eng A 379 (2004) 204.
- [21] Jimenez-Melero E, van Dijk NH, Zhao L, Sietsma J, Offerman SE, Wright JP, et al. Acta Mater 55 (2007) 6713.
- [22] Zhao L, van Dijk NH, Brück E, Sietsma J, van der Zwaag S. Mat Sci Eng A 313 (2001) 141.
- [23] Blondé R, Jimenez-Melero E, van Dijk NH, Brück E, Zhao L, Sietsma J, et al. Solid State Phenom 172-174 (2011) 196.
- [24] van Dijk NH, Butt AM, Zhao L, Sietsma J, Offerman SE, Wright JP, et al. Acta Mater 53 (2005) 5439.
- [25] Kruijver S, Zhao L, Sietsma J, Offerman E, van Dijk N, Margulies L, et al. Steel Res 73 (2002) 236.
- [26] Park KK, Oh ST, Kim DI, Han JH, Han HN, Park SH, et al.

Mat Sci Forum 408-412 (2002) 571.

[27] Muránsky O, Šittner P, Zrník J, Oliver EC. Metall Mater Trans A 39A (2008) 3097.

[28] Jia N, Cong ZH, Sun X, Cheng S, Nie ZH, Ren Y, et al. Acta Mater 57 (2009) 3965.

[29] Jung J, Kim H, De Cooman BC. ISIJ Int 50 (2010) 620.

[30] Tomota Y, Tokuda H, Adachi Y, Wakita M, Minakawa N, Moriai A, Morii Y.

Acta Mater 52 (2004) 5737.

[31] Asoo K, Tomota Y, Harjo S, Okitsu Y. ISIJ Int 51 (2011) 145.

[32] Cong ZH, Jia N, Sun X, Ren Y, Almer J, Wang YD. Metall Trans A 40A (2009) 1383.

[33] Lani F, Furnémont Q, Van Rompaey T, Delannay F, Jacques PJ, Pardoën T.

Acta Mater 55 (2007) 3695.

[34] Choi KS, Liu WN, Khaleel MA, Ren Y, Wang YD. Metall Mater Trans A 39A (2008) 3089.

[35] Tjahjanto DD, Turteltaub S, Suiker ASJ, van der Zwaag S. Phil Mag 88 (2008) 3369.

[36] Choi KS, Liu WN, Sun X, Khaleel MA. Acta Mater 57 (2009) 2592.

[37] Liss KD, Yan K. Mat Sci Eng A 528 (2010) 11.

[38] Jimenez-Melero E, van Dijk NH, Zhao L, Sietsma J, Wright JP, van der Zwaag S.

Mater Sci Eng A 528 (2011) 6407.

[39] Jimenez-Melero E, van Dijk NH, Zhao L, Sietsma J, Offerman SE, Wright JP, et al.

Scripta Mater 56 (2007) 421.

[40] Jimenez-Melero E, van Dijk NH, Zhao L, Sietsma J, Offerman SE, Wright JP, et al.

Acta Mater 57 (2009) 533.

[41] Labiche JC, Mathon O, Pascarelli S, Newton MA, Ferre GG, Curfs C et al.

Rev Sci Instr 78 (2007) 091301.

[42] Hammersley AP, Svensson SO, Hanfland M, Fitch AN, Hausermann D.

High Pressure Res 14 (1996) 235.

[43] Rodríguez-Carvajal J. Physica B 192 (1993) 55.

[44] Daymond MR, Bourke MAM, von Dreele RB, Clausen B, Lorentzen T.

J Appl Phys 82 (1997) 1554.

[45] Lutterotti L, Matthies S, Wenk HR. CPD Newsletter IUCr 21 (1999) 14.

[46] Lutterotti L, Bortolotti M, Ischia G, Lonardelli I, Wenk HR.

Z Kristallogr Suppl 26 (2007) 125.

[47] Curtze S, Kuokkala VT, Hokka M, Peura P. Mat Sci Eng A 507 (2011) 124.

[48] Muránsky O, Šittner P, Zrník J, Oliver EC. Acta Mater 56 (2008) 3367.

[49] Jiménez JA, Carsí M, Ruano OA, Frommeyer G. Mater Sci Eng A 508 (2009) 195.

[50] Scott CP, Drillet J. Scripta Mater 56 (2007) 489.

[51] Andrews KJ. J Iron Steel Inst 203 (1965) 721.

-
- [52] Adams JJ, Agosta DS, Leisure RG. *J Appl Phys* 100 (2006) 113530.
- [53] Nye JF. *Physical properties of crystals*. Oxford: Oxford University Press (1985).
- [54] Oliver EC. PhD Thesis, University of Manchester (2002).
- [55] Lorentzen T. *Analysis of residual stress by diffraction using neutron and synchrotron Radiation*. Eds. Fitzpatrick ME, Lodini A. Taylor & Francis (2003) p. 115.
- [56] Oliver EC, Withers PJ, Daymond MR, Ueta S, Mori T. *Appl Phys A* 74 (2002) S1143.
- [57] Patel JR, Cohen M. *Acta Metall* 1 (1953) 531.

Chapter 5

Shear experiments for different bainitic holding times

The microstructure evolution during shear loading of a low-alloyed TRIP steel with different amounts of the metastable austenite phase and its equivalent DP grade has been studied by in-situ high-energy X-ray diffraction. A detailed powder diffraction analysis has been performed to probe the austenite-to-martensite transformation by characterizing simultaneously the evolution of the austenite phase fraction and its carbon concentration, the load partitioning between the austenite and the ferritic matrix and the texture evolution of the constituent phases. Our results show that for shear deformation the TRIP effect extends over a significantly wider deformation range than for simple uniaxial loading. A clear increase in average carbon content during the mechanically-induced transformation indicates that austenite grains with a low carbon concentration are least stable during shear loading. The observed texture evolution indicates that under shear loading the orientation dependence of the austenite stability is relatively weak, while it has previously been found that under tensile load the $\{110\}\langle 001\rangle$ component transforms preferentially. The mechanical stability of retained austenite in TRIP steel is found to be a complex interplay between the interstitial carbon concentration in the austenite, the grain orientation and the load partitioning.

5.1 Introduction

Low-alloyed transformation-induced-plasticity (TRIP) steels were developed in the late 1980s [1–3] and have attracted significant interest for automotive applications due to their outstanding combination of high strength and formability [4–9]. At room temperature a typical TRIP steel microstructure contains three phases: ferrite, bainite and metastable austenite [10,11]. The remarkable mechanical properties of

this material are attributed to the multiphase microstructure as well as to the transformation of the soft metastable austenite phase into the hard martensite phase upon activation by mechanical and/or thermal stimuli. This phenomenon, called the TRIP effect, increases the work-hardening rate during plastic deformation and delays necking [12,13]. The understanding of the mechanical parameters controlling the austenite stability under complex loading conditions remains limited.

Previous in-situ studies have examined the austenite stability by cooling the material [14-19] or by applying an uniaxial tensile load at room temperature [20-28] and at selected low temperatures [29]. These experimental results led to the development of advanced micromechanical models for the TRIP multiphase microstructure [30-33]. The influence of shear loading and more complicated deformation states is still not investigated in detail. Understanding the mechanical response of the microstructure during shear deformation is an essential step to control the sheet forming process in TRIP steels for automotive application [34]. An accurate prediction of this process requires a better insight in the mechanical response in terms of the austenite-to-martensite transformation, the load partitioning between the constituent phases and the texture evolution during shear loading.

In this study, a detailed characterization of the austenite stability during shear loading has been made by in-situ high-energy synchrotron X-ray diffraction (XRD) experiments. In order to determine the effect of the austenite-to-martensite transformation on the mechanical response, a single low-alloyed steel composition with three different microstructures has been investigated: a dual-phase (DP) steel without austenite, a TRIP steel with stable austenite (TRIP-15min) and a TRIP steel with metastable austenite (TRIP-2min). The relation between the macroscopic stress, the orientation-dependent martensitic transformation and grain rotations has been determined by a Rietveld refinement of the high-energy XRD data. A complementary position-dependent mapping of the strain fields in the shear region will be presented elsewhere.

5.2 Experimental methods

5.2.1 Sample preparation

The chemical composition of the TRIP steel studied is shown in Table 5.1. Double-notched plate specimens [35] with a shear length of 1 mm and a thickness of 1 mm were machined for the shear experiments from hot-rolled sheet material by spark erosion. The slits are at 45° with respect to the loading direction and have a width of 0.2 mm. The loading axis of the samples was chosen parallel to the rolling direction (RD).

Table 5.1: *Chemical composition of the studied samples in wt.% with balance Fe.*

C	Mn	Si	Al	P
0.218	1.539	0.267	1.75	0.018

Three different microstructures have been generated by the applied heat treatment. To start, all samples were annealed in a salt bath for 30 min at an intercritical temperature of 1143 K in order to obtain about equal fractions of austenite and ferrite. The first microstructure was obtained by a direct quench to room temperature creating a dual phase steel (DP) containing about equal amounts of ferrite (α) and martensite (α'). The other two samples were quenched in a second salt bath to a temperature of 673 K and held for either 2 min (TRIP-2min) or 15 min (TRIP-15min), respectively. During this isothermal holding the intercritical austenite transformed partly into bainite, resulting in a continuous enrichment of the interstitial carbon content in the untransformed austenite. The carbon-enriched austenite remained in a metastable state after a final water quench to room temperature. This heat treatment for the TRIP-2min and the TRIP-15min samples yielded a multiphase microstructure composed of ferrite (α), bainite (α_b) and metastable austenite (γ). In Fig. 5.1 the formed microstructures are shown.

5.2.2 In-situ high-energy X-ray diffraction

The *in-situ* XRD experiments were performed at the high-energy materials science beamline (P07) of the PETRA III synchrotron radiation source at DESY (Hamburg, Germany). Fig. 5.2 shows the sample geometry and the experimental setup used for the experiments.

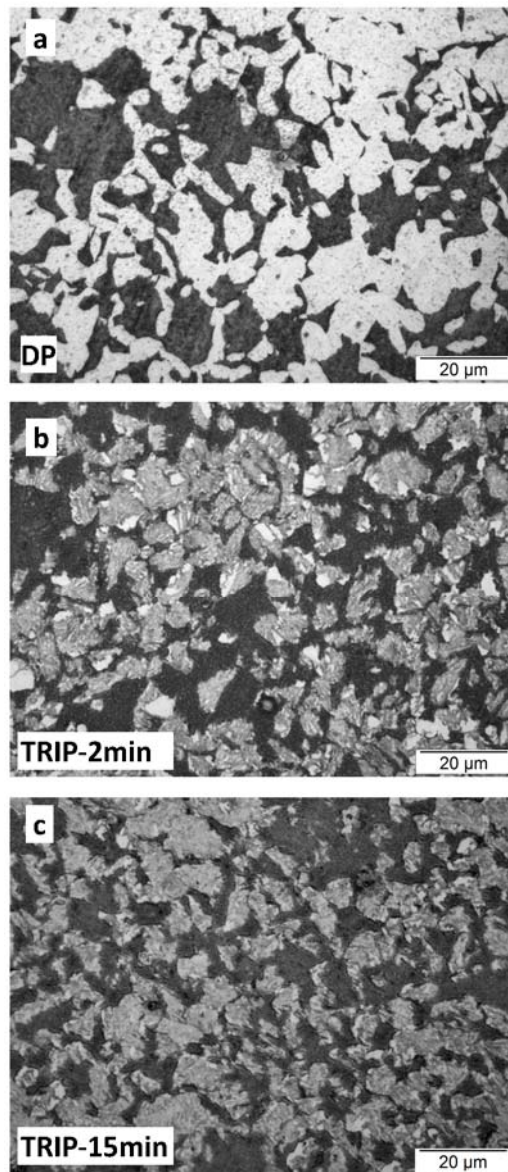


Figure 5.1: *Initial microstructure of the studied samples: (a) DP, (b) TRIP-2min and (c) TRIP-15min. The DP microstructure contains a matrix of ferrite (black) and martensite (white). The TRIP microstructure contains a metastable austenite phase (white) within a matrix of ferrite (black) and bainite (grey) phases.*

A monochromatic X-ray beam with an energy of 79.6 keV (wavelength of 0.156 Å) and a beam size of $100 \times 100 \mu\text{m}^2$ illuminated the plate sample. For the high-energy X rays the sample absorption is relatively small, making it possible to study even 1 mm thick samples in transmission geometry. The diffracted beam was recorded on a two-dimensional digital flat panel X-ray detector (Perkin Elmer XRD 1622) placed at 1025.1 mm behind the sample.

To study the mechanical response of the constituent phases, the sample was mounted on a 2-kN micro tensile tester (Deben) placed on a translation table that provided alignment of the sample in three directions with respect to the X-ray beam and ω rotation around the loading axis of the sample. The symmetric displacement of the grips of the micro tensile tester permits us to monitor the same sample volume during the tests.

During the experiment samples were continuously rotated around the loading axis perpendicular to the X-ray beam in steps of $\Delta\omega = 0.5^\circ$, covering a total angular range of 80° . For each deformation step the strain was held constant during a complete set of diffraction measurements over the full ω range. During each rotation step a two-dimensional (2D) diffraction pattern was recorded continuously using an exposure time of 0.5 s. The instrument parameters for the X-ray diffraction setup were determined using a CeO_2 calibrant (NIST SRM 674b).

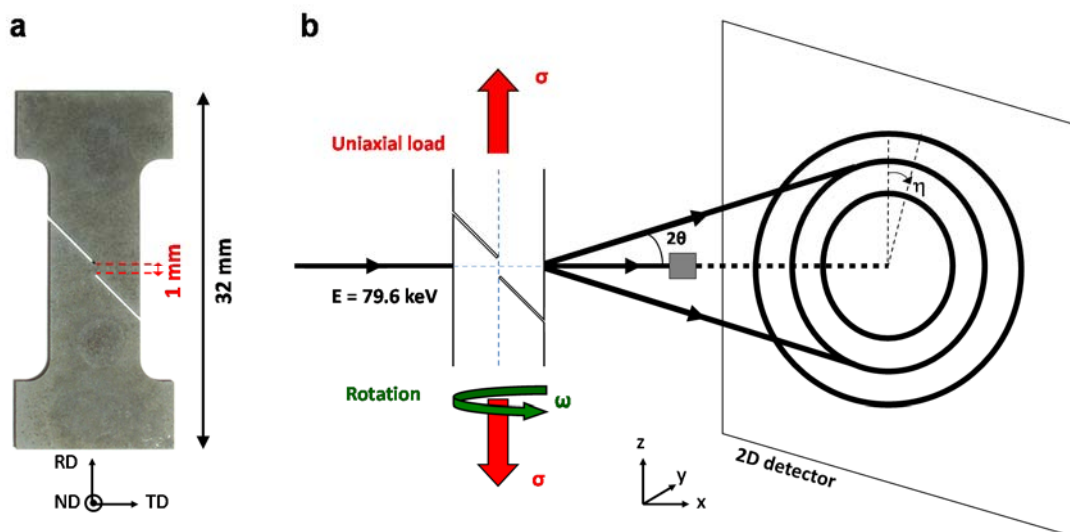


Figure 5.2: Schematic representation of (a) the sample geometry of the shear specimen and (b) the experimental setup used for the high-energy microbeam X-ray diffraction experiments. The monitored sample volume with a beam size of $100 \times 100 \mu\text{m}^2$ is positioned in the centre of the shear area indicated by the crossing of the dotted lines.

5.2.3 Data analysis

The measured data consist of a series of 2D diffraction patterns as a function of the sample elongation and ω angle. For each deformation step the individual ω -dependent 2D diffraction patterns were

summed for the covered ω range of 80° . An integration over the azimuth angles at constant scattering angle was performed using the FIT2D software package [36] to obtain the corresponding one-dimensional (1D) diffraction patterns. A Rietveld refinement of the resulting 1D X-ray diffraction patterns was performed using the Fullprof package [37] in order to determine the phase fraction and lattice parameter of the constituent phases as a function of the macroscopic strain. Fig. 5.3 shows two examples of the 2D X-ray diffraction patterns with the corresponding 1D patterns analysed by the Rietveld method before and after applying a shear load for the TRIP-2min sample. Shear deformation leads to a reduction in peak intensity for the metastable austenite phase having a face-centred cubic (fcc) structure, and an increase in the diffraction peaks for the ferritic matrix having a body-centred cubic (bcc) structure.

In addition to the study of the average phase behaviour, we integrated each summed 2D pattern for constant scattering angles over sections of the detector covering an azimuth angular range of 10° . Each 2D pattern then yielded 36 1D patterns. All the resultant 1D patterns were fitted using Fullprof in a batch processing mode. The variation of the lattice parameter as a function of the azimuth angle for each deformation step reveals the evolution of the elastic properties of the constituent phases with stress.

A texture analysis has been performed using the MAUD software [38] to monitor the evolution of the preferred $\{hkl\}$ plane orientation with respect to the rolling (RD), normal (ND) and transverse (TD) sample directions. For each elongation step 16 individual two-dimensional patterns were obtained by summing the measured data over an ω range of 5° . These summed patterns were then integrated over 5° of the azimuth angle. The 16×72 resulting 1D patterns were again analysed by the Rietveld method using MAUD and the E-WIMV algorithm [39] for the texture refinement.

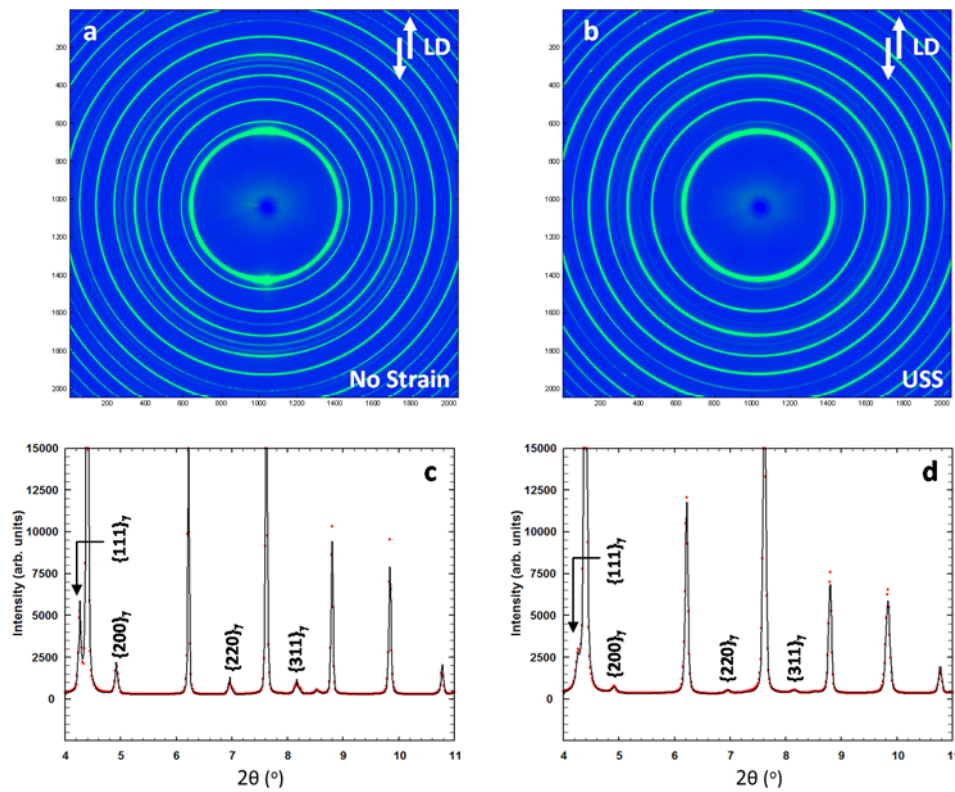


Figure 5.3: 2D X-ray diffraction patterns at (a) no strain and (b) ultimate shear strength (USS). These patterns have been obtained by summing all the measured patterns for the whole ω -range used in the experiments. The loading direction (LD) is indicated in the figure. The 2D patterns have been subsequently integrated over the azimuth angles to obtain the one-dimensional X-ray patterns as a function of the scattering angle at (c) no strain and (d) ultimate shear strength. The corresponding Rietveld refinement of the one-dimensional X-ray patterns is also shown. The studied $\{111\}_\gamma$, $\{200\}_\gamma$, $\{220\}_\gamma$ and $\{311\}_\gamma$ austenite reflections have been labeled on the 1D patterns.

5.3 Results and discussion

5.3.1 Macroscopic mechanical behaviour

Fig. 5.4a shows the mechanical response of the three steels deformed under shear load. The sample elongation corresponds to the displacement of the grips normalized to the length of the shear section in the sample. Table 5.2 contains the relevant parameters that characterize the macroscopic mechanical behaviour of the 3 samples. The difference in microstructure, resulting from the variation in bainitic holding time, results in a significant change in the mechanical response. The ultimate shear strength (USS) and the elongation at fracture vary respectively from 630 to 495 MPa and from 24.4% to 60.4% by varying the bainitic holding time from 0 to 15 min. Due to presence of about 50% of the strong martensite phase in the dual-phase steel the macroscopic stress-strain curve remains linear nearly up to

fracture. The two TRIP microstructures also show a different response: the TRIP-2min sample shows a higher ultimate shear stress and a lower elongation at fracture compared to the TRIP-15min. This difference is explained by the variation in fraction and carbon content of the metastable austenite phase. The strong sensitivity of the macroscopic mechanical response on the microstructural parameters highlights the need to understand the microstructural evolution in TRIP steels in order to control and predict their mechanical properties.

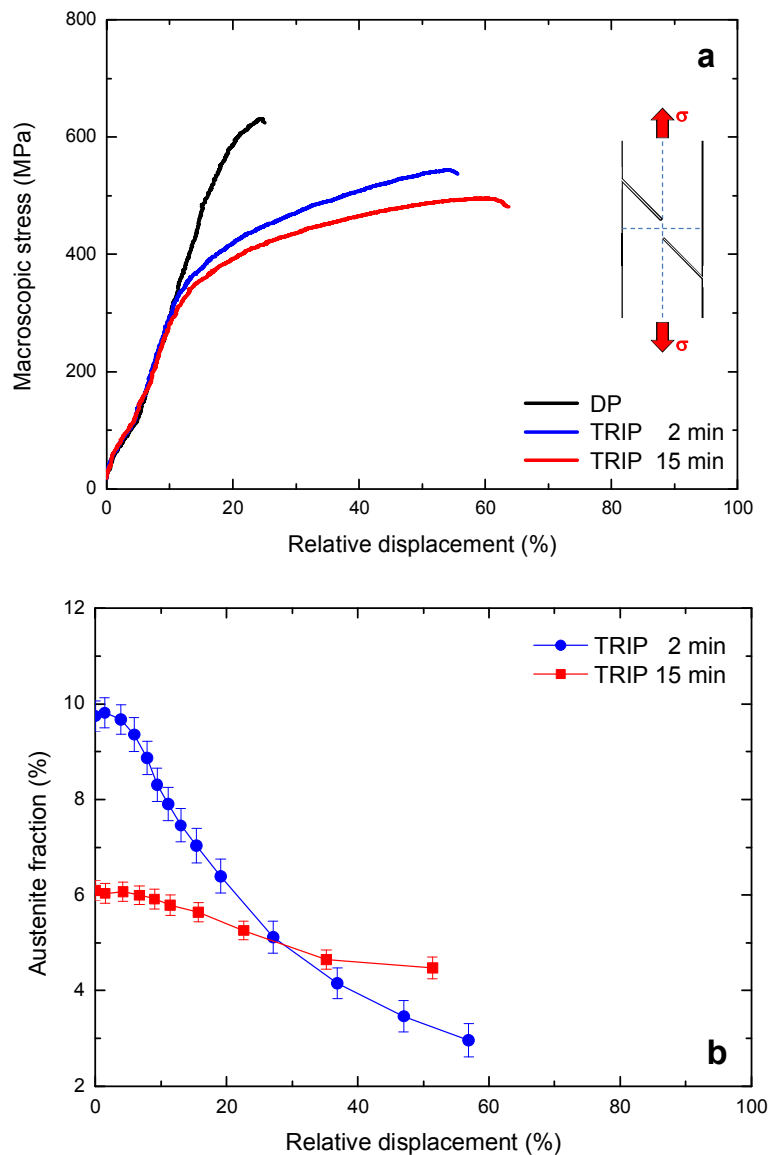


Figure 5.4: (a) Macroscopic shear stress as a function of the relative displacement of the DP, TRIP-2min and TRIP-15min steels during shear loading. (b) Austenite fraction as a function of the relative displacement under shear load for the TRIP-2min and TRIP-15min steels. The austenite fraction was obtained from the in-situ X-ray diffraction measurements at constant strain during step-wise deformation.

Table 5.2: Characteristic values for the macroscopic mechanical response of the steels deformed continuously under shear load for DP, TRIP-2min and TRIP-15min steels.

Steel	Yield Strength (MPa)	Ultimate Shear Strength (MPa)	Elongation at YS (%)	Elongation at fracture (%)
DP	527	630	17.1	24.4
TRIP-2min	324	543	10.9	54.1
TRIP-15min	290	495	10.1	60.4

5.3.2 Evolution of the austenite phase fraction

The austenite phase fraction was derived from the Rietveld refinement of the 1D diffraction patterns at the selected deformation steps, assuming the presence of two phases: an austenite phase embedded within a homogeneous ferritic matrix (consisting of ferrite, bainite, and martensite). Fig. 5.3c and 5.3d show the fitted patterns of the TRIP-2min sample at zero strain and at ultimate shear strength, respectively. The austenite reflections show a significant reduction in intensity as a result of the shear deformation. Fig. 5.4b shows the fitted austenite fraction as a function of the macroscopic strain for bainitic holding times of 2 and 15 min. The difference in initial austenite fraction of 9.7% for the TRIP-2min sample and 6.1% for the TRIP-15min sample is related to the bainitic holding time. The bainite formation leads to a continuous reduction in the austenite fraction for increasing holding times. For this steel composition and annealing temperature the optimal holding time to retain a maximum amount of metastable austenite at room temperature had previously been determined at 2 min [16]. The austenite fraction of the TRIP-2min sample decreases with increasing strain due to the mechanically induced austenite transformation into martensite, while the austenite fraction of the TRIP-15min sample remains relatively constant with increasing strain. For the TRIP-2min sample, the martensitic transformation continues until fracture. As shown in Table 5.3, the amount of austenite transformed by shear deformation is 6.7% for a bainitic holding time of 2 min and 1.6% for a bainitic holding time of 15 min. This indicates that the lower austenite carbon concentration in the TRIP-2min sample exhibits a lower stability and a higher degree of transformation during shear deformation compared to the TRIP-15min sample. The larger austenite fraction transformed by shear deformation correlates to a higher ultimate shear strength in the stress-strain curve of Fig. 5.4a.

Table 5.3: Austenite fraction for the TRIP steel measured for different strain stages for the TRIP-2min and TRIP-15min steels.

Steel	Austenite fraction Initial value (%)	Austenite fraction at Yield strength (%)	Austenite fraction at fracture (%)
TRIP-2min	9.7(3)	7.9(3)	3.0(4)
TRIP-15min	6.1(2)	5.8(2)	4.5(2)

5.3.3 Relative change in lattice parameter

The elastic strain tensor ϵ_{ij} can be determined by measuring the normal strains in various directions in the sample coordinates (1, 2, 3) = (RD, TD, -ND) [40,41], where RD is the rolling direction, ND the normal direction and TD the transverse direction of the plate sample. Note that RD is along the vertical loading axis and ND along the X-ray beam in the laboratory system. The orientation-dependent elastic strain $\epsilon_{\phi\psi}$ with respect to the sample coordinates is defined in terms of the angles ϕ and ψ , where ϕ is defined with respect to RD (loading axis) and ψ is defined with respect to ND. The orientation-dependent normal strain $\epsilon_{\phi\psi}$ can be related to the elastic strain tensor ϵ_{ij} by [40,41]:

$$\epsilon_{\phi\psi} = \frac{a_{\phi\psi} - a_0}{a_0} = \left(\epsilon_{11} \cos^2 \phi + \epsilon_{12} \sin 2\phi + \epsilon_{22} \sin^2 \phi \right) \sin^2 \psi + \epsilon_{33} \cos^2 \psi + \left(\epsilon_{13} \cos \phi + \epsilon_{23} \sin \phi \right) \sin 2\psi \quad (1)$$

where a_0 is the lattice parameter at zero deformation and $a_{\phi\psi}$ in the deformed state measured along the sample orientation defined by angles ϕ and ψ . Variables ϵ_{11} , ϵ_{12} , ϵ_{22} , ϵ_{13} , ϵ_{23} and ϵ_{33} are the components of the elastic strain tensor ϵ_{ij} in sample coordinates. For X-ray diffraction in transmission geometry using a 2D detector, the sample coordinates can be translated in detector coordinates by $\phi = -\eta$ and $\psi = \frac{\pi}{2} - \theta$, where η is the azimuth angle on the surface detector and θ is the Bragg angle.

As θ is small ($\theta < 5^\circ$) for our high energy X-ray diffraction experiment, the strain equation reduces to:

$$\epsilon(\eta) = \frac{a(\eta) - a_0}{a_0} \approx \left(\frac{\epsilon_{11} + \epsilon_{22}}{2} \right) + \left(\frac{\epsilon_{11} - \epsilon_{22}}{2} \right) \cos 2\eta - \epsilon_{12} \sin 2\eta \quad (2)$$

Fig. 5.5 shows the development of the relative change in lattice parameter as a function of the azimuth angle monitored at the centre of the shear band for the studied macroscopic strain steps. A clear sinusoidal normal strain $\varepsilon(\eta)$ develops during shear loading for both the austenite phase and the ferritic matrix. For a positive ε_{12} contribution minima in $\varepsilon(\eta)$ are expected for η values around 45° and 225° and maxima for 135° and 315° . For our double-notched sample geometry, the maximum shear strain is observed at slightly higher angles. The estimated tilt angle of the shear band with respect to the vertical loading axis is between 5 and 10 degrees. During deformation, the load is distributed between the austenite and the ferritic matrix.

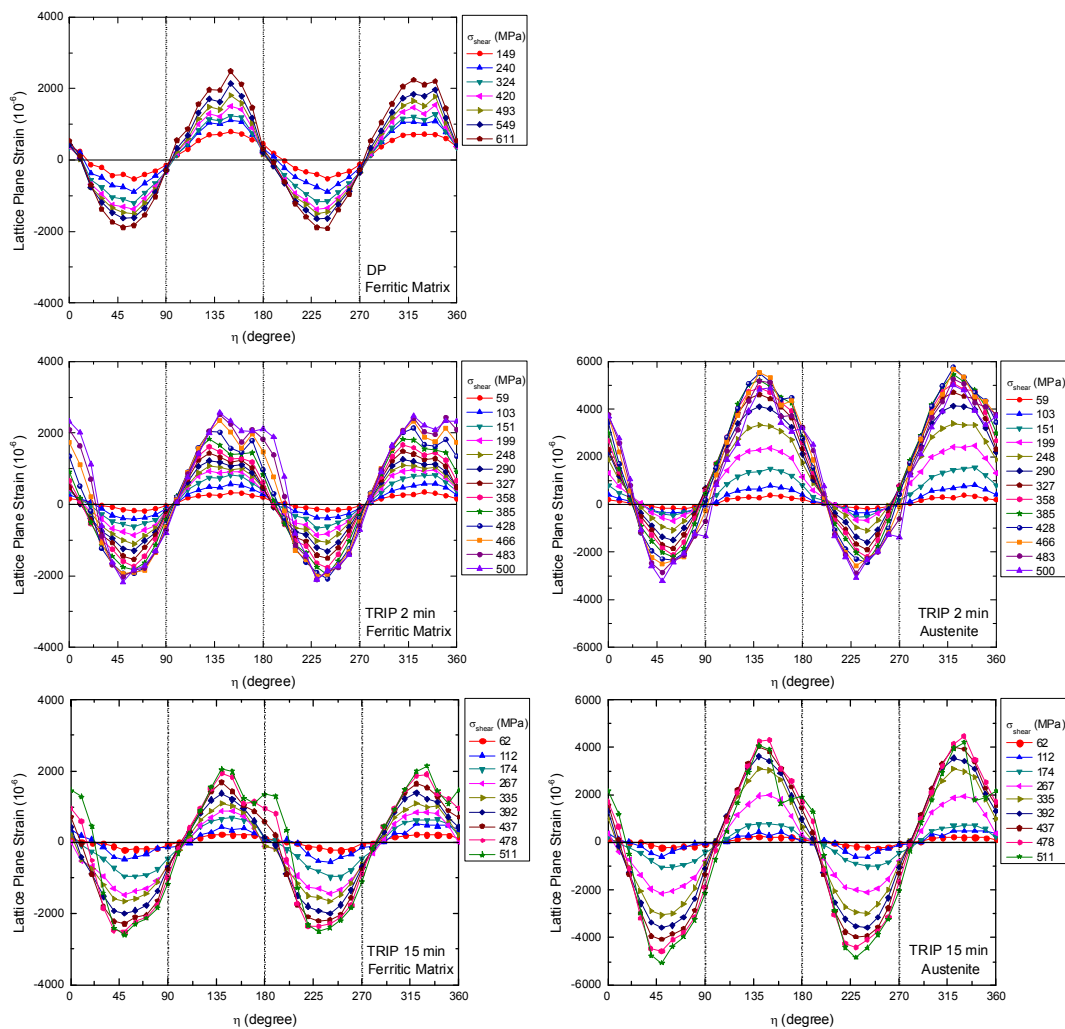


Figure 5.5: Lattice plane strain of the ferritic matrix and austenite as a function of the azimuth angle for a varying macroscopic shear stress.

The relative change in lattice parameters of austenite originates from both the elastic strain and the average carbon enrichment resulting from the mechanically-induced martensite transformation. For the TRIP-2min sample, the global increase in the average lattice parameter of austenite originates from an increase in carbon content of the austenite that is untransformed by the shear loading (caused by a preferential transformation of the least stable grains with a low carbon content). In addition to the shear strain, the TRIP microstructure also shows a weaker elastic tensile component developing at the later deformation stages. This new component is found at characteristic η values of 0° , 90° , 180° and 270° and is more pronounced for the ferritic matrix than for the austenite. This suggests that the overall strain state in the strongly deformed state combines shear and tensile modes. The shear component for both phases can be estimated by $\varepsilon_{12} = [\varepsilon(45^\circ) - \varepsilon(-45^\circ)] / 2$. The relative change in the (shear) strain-free lattice parameter can be estimated by $\varepsilon_0 = [\varepsilon(45^\circ) + \varepsilon(-45^\circ)] / 2$. For the austenite phase ε_0 reflects the relative change in lattice parameter due to the carbon enrichment $\varepsilon_0 = \varepsilon_C$, while for the ferritic matrix $\varepsilon_0 = 0$ is expected.

Fig. 5.6 shows the amplitude of the elastic shear strain ε_{12} , axial tensile strain $\varepsilon_{11} = \varepsilon(0^\circ)$, transverse tensile strain $\varepsilon_{22} = \varepsilon(90^\circ)$. In addition the value of ε_0 is shown for both phases. Below the macroscopic yield point, the lattice plane strains of the austenite phase and ferritic matrix evolve linearly with the macroscopic shear stress. For the TRIP-2min sample, austenite shows a shear modulus ($G = C_{44} = C_{55} = C_{66}$) of $G_\gamma = 75(3)$ GPa, while for the ferritic matrix a value of $G_\alpha = 214(1)$ GPa is obtained. The reported single-crystal shear moduli at room temperature are $G_\alpha = 118$ GPa for bcc iron (ferrite) and of $G_\gamma = 145$ GPa for fcc iron (austenite) [32]. The difference in the shear moduli between the single-crystal values and the values obtained for our TRIP-2min sample partly arises from the effect of the surrounding microstructure. In addition, for the ferritic matrix the presence of bainite and the newly formed martensite will be of influence. The DP sample shows a significantly higher shear modulus of $G_\alpha = 330(13)$ GPa resulting from the presence of a relatively large fraction of about 50% martensite

within the microstructure. In Table 5.4 the shear moduli for both phases are reported as a function of the bainitic holding time.

Table 5.4: *Shear modulus G of the ferritic matrix and the austenite for DP, TRIP-2min and TRIP-15min steels.*

Steel	Ferritic Matrix G (GPa)	Austenite G (GPa)
DP	330(13)	-
TRIP-2min	214(1)	75(3)
TRIP-15min	240(1)	77(4)

In Fig. 5.7 the carbon enrichment Δx_C in the austenite phase of the TRIP-2min sample is shown as a function of the macroscopic shear stress. In this figure the corresponding austenite fraction is also shown. The change in average carbon concentration in the austenite phase, resulting from the martensitic transformation of the least stable grains is obtained from the relative change in austenite lattice parameter ε_C . The austenite lattice parameter is related to chemical composition via the following relationship [17]:

$$a_\gamma = 3.556 + 0.0453x_C + 0.00095x_{Mn} + 0.0056x_{Al} \quad (3)$$

where a_γ is in Å and x_C , x_{Mn} and x_{Al} are in wt.%. The obtained initial carbon content amounts to $x_C = 1.30(2)$ wt.% for the TRIP-2min sample and $x_C = 1.50(1)$ wt.% for the TRIP-15min sample. The increase in x_C for the TRIP-15min sample compared to the TRIP-2min sample is caused by the longer bainitic holding time that further enriches the remaining austenite. Under shear the carbon enrichment increases continuously with the transformed austenite fraction, resulting in a maximum carbon enrichment of $\Delta x_C = 0.13$ wt.% for a transformed austenite fraction of 6.7%.

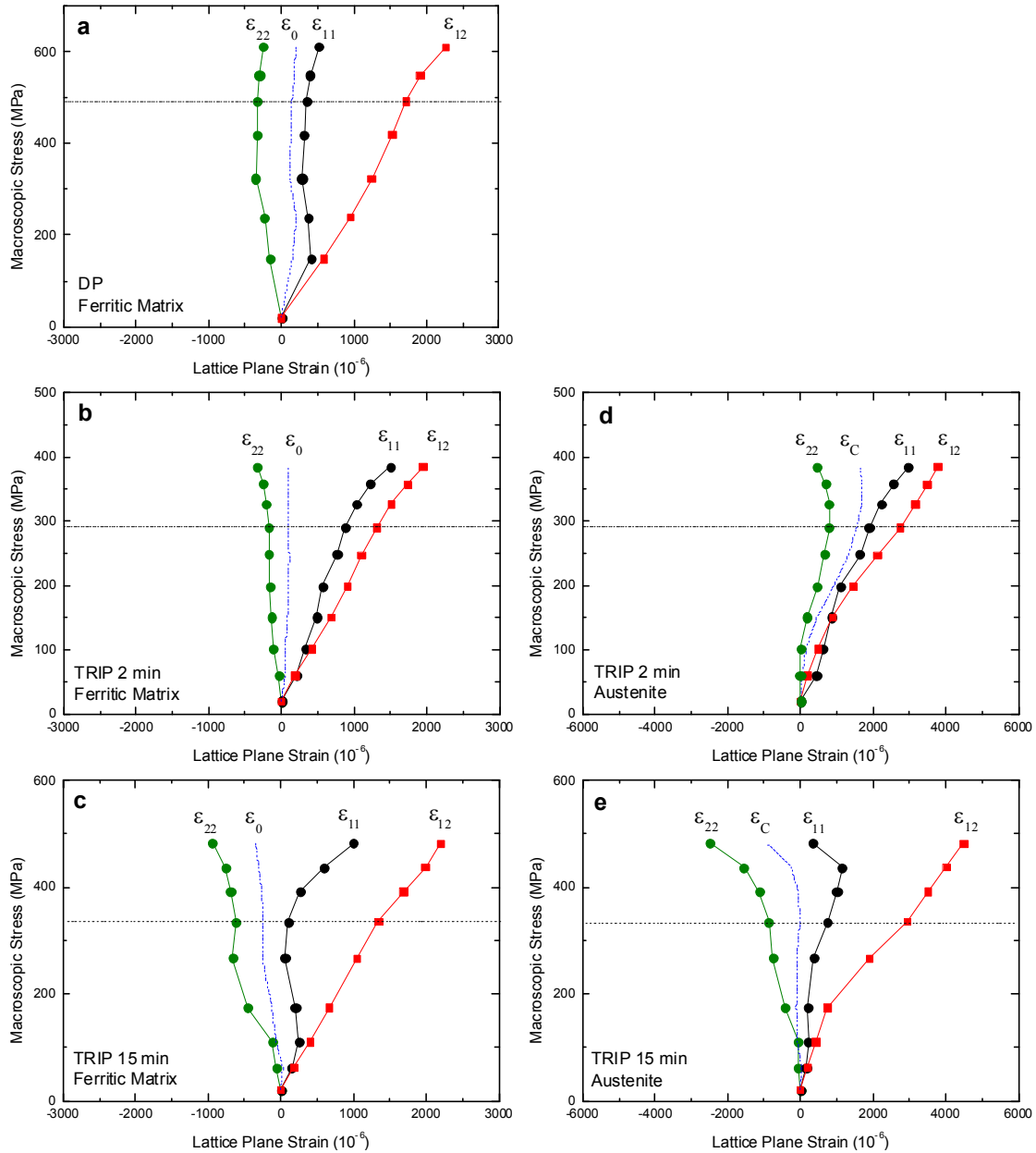


Figure 5.6: Amplitude of the elastic strain components ϵ_{12} , ϵ_{11} and ϵ_{22} of the ferritic matrix and austenite as a function of the macroscopic stress for the DP, TRIP-2min and TRIP-15min steels. In addition the value of ϵ_0 is shown for the ferritic matrix and ϵ_C for austenite (see text). The horizontal dashed lines correspond to the macroscopic yield point.

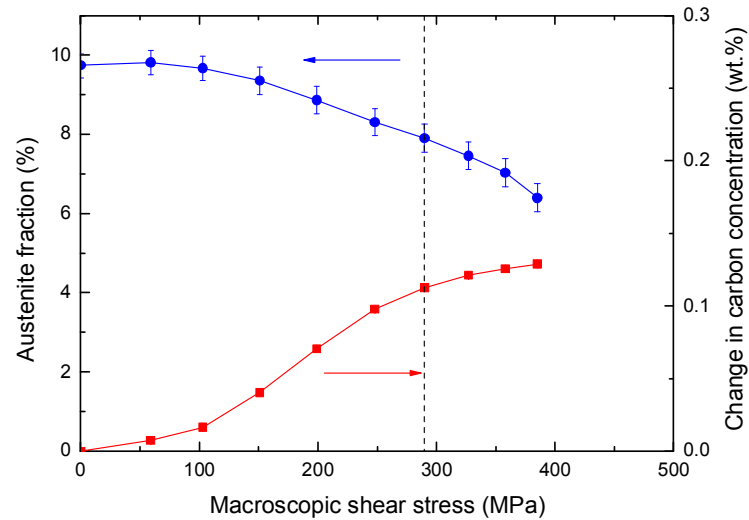


Figure 5.7: Phase fraction and carbon enrichment of the austenite phase in the TRIP-2min sample. The increase in the average carbon content in the remaining austenite is caused by the preferred transformation of the less stable austenite grains.

5.3.4 Austenite stability for individual $\{hkl\}$ planes

In Fig. 5.8 the relative integrated intensity of the individual $\{hkl\}$ austenite reflections is shown as a function of the macroscopic stress for grains with a plane normal oriented 0° , 45° and 90° with respect to the loading direction. Up to the macroscopic yield strength the intensity of all $\{hkl\}$ reflections slowly decreases proportional to the austenite fraction. The presence of a comparable decrease in relative intensity for all $\{hkl\}$ planes at 0° , 45° and 90° orientations indicates that the martensitic transformation is nearly isotropic under shear load. In order to understand this the resolved shear stress along the most favourable slip system should be considered [32,42].

For the more common case of tensile stress one finds $\tau_{RSS} = \sigma \cos(\phi) \cos(\lambda)$, where σ is the macroscopic tensile stress, ϕ is the angle between the macroscopic tensile direction (\hat{l}_1) and the plane normal of the $\{111\}$ austenite shear plane (\hat{n}) and λ is the angle between the macroscopic tensile direction (\hat{l}_1) and the $\langle 110 \rangle$ slip direction (\hat{s}) within the shear plane. The corresponding Schmid factor then amounts to $m = \tau_{RSS} / \sigma = (\hat{l}_1 \cdot \hat{n})(\hat{l}_1 \cdot \hat{s}) = \cos(\phi) \cos(\lambda)$. The critical resolved shear stress τ_{CRSS} is

obtained by the maximum resolved shear stress for the most favourable slip system. In total 12 different $\{111\}\langle 110\rangle$ slip systems can be activated.

For shear loading the resolved shear stress can be written as $\tau_{RSS} = \tau \cos(\psi) \cos(\lambda)$, where $\tau = \sigma_{12}$ is the macroscopic shear stress, ψ is the angle between the macroscopic shear plane normal (\hat{l}_2) and the plane normal of the $\{111\}$ austenite shear plane (\hat{n}) and λ is the angle between the macroscopic shear direction (\hat{l}_1) and the $\langle 110\rangle$ slip direction (\hat{s}) within the shear plane. The resolved shear stress relative to the macroscopically applied shear then corresponds to $\tau_{RSS} / \tau = (\hat{l}_2 \cdot \hat{n})(\hat{l}_1 \cdot \hat{s}) = \cos(\psi) \cos(\lambda)$.

In a powder experiment one generally still needs to average over the possible orientations, as within one family of $\{hkl\}$ planes only the plane normal of the diffracting plane is known. One relatively simple example is found for the $\{111\}$ plane at $\eta = 90^\circ$. In this case we find $\tau_{CRSS} / \tau = \langle \cos(\lambda) \rangle = 3 / \pi = 0.96$ (with $0.87 \leq \cos(\lambda) \leq 1$) as the macroscopic and microscopic shear planes are aligned.

Beyond the macroscopic yield stress the reduction in intensity for the $\{200\}$, $\{220\}$ and $\{311\}$ reflection is strongly enhanced by the plastic deformation that promotes further transformation of the remaining austenite. It is interesting to note that in the plastic regime a significant orientation dependence is observed for the $\{111\}$ plane intensity. For the shear orientation at 45° a slight increase in the $\{111\}$ plane intensity is observed, while for 0° no difference in behaviour with respect to the $\{200\}$, $\{220\}$ and $\{311\}$ planes is observed. For 90° the decrease in the $\{111\}$ plane intensity falls in between the ones for 45° and 0° . The increase in the $\{111\}$ plane intensity at 45° suggests that this plane experiences a significant grain rotation towards the orientation with the highest normal strain during plastic deformation by shear loading.

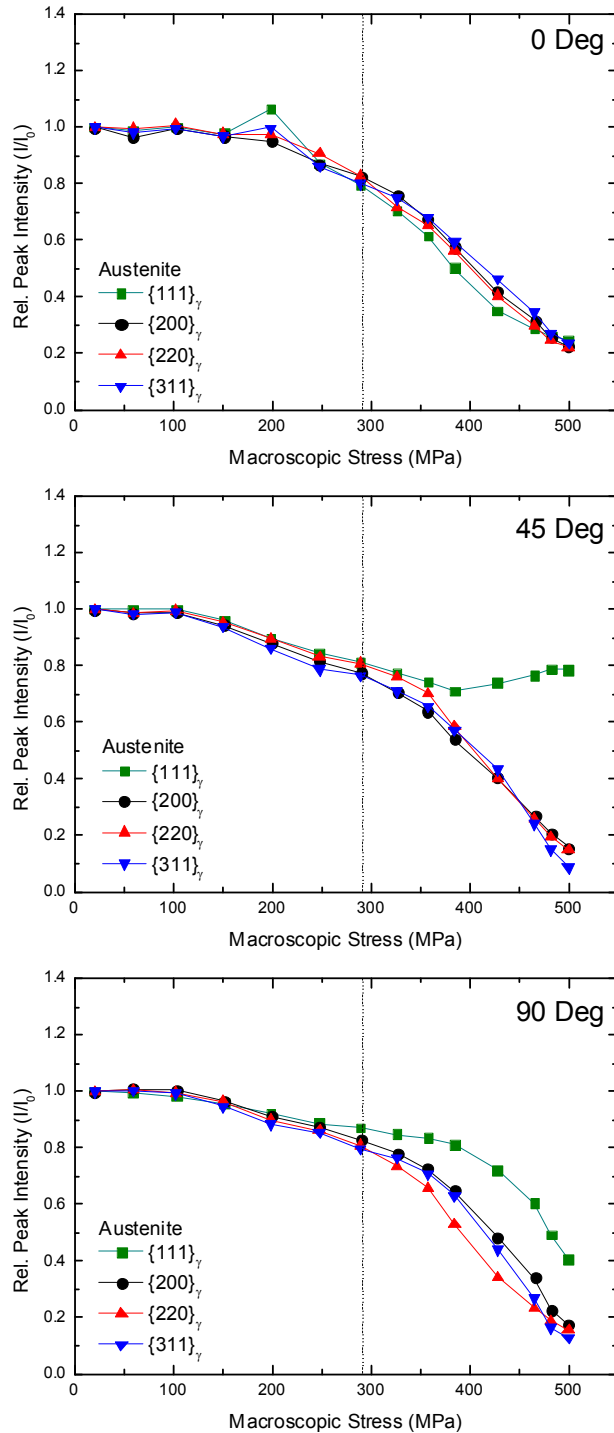


Figure 5.8: Relative peak intensity of the individual $\{hkl\}$ austenite reflections as a function of the macroscopic stress for grains with a plane normal oriented 0° , 45° and 90° with respect to the loading direction. The vertical dotted lines correspond to the macroscopic yield point.

In line with our previously proposed model [29] the dependence of the martensite start temperature M_s on the (elastic) shear stress can qualitatively be described by:

$$M_s(\sigma) = M_s(0) + C\tau_{RSS}^2 = M_s(0) + Cn^2\tau^2 \quad (4)$$

where $C = (1/2G)(d\Delta g_v/dT)^{-1}$ is a constant, G is the shear modulus and Δg_v the difference in Gibbs free energy per unit volume between austenite and martensite. In agreement with the experimental data in Fig. 5.9, the relative intensity of the $\{hkl\}$ diffraction peaks is found to scale with τ^2

5.3.5 Texture analysis

A texture analysis of the constituent phases has been performed using the MAUD software for selected macroscopic stress states. Fig. 5.9 shows for all 3 samples the texture evolution from the undeformed state to the yield strength and for the TRIP-2min sample to ultimate shear strength (USS). In Table 5.5 the local stress state of the constituent phases has been derived using the Reuss model for all three samples at the selected macroscopic stress states. The orientation of the grains has been represented by inverse pole figures as a function of the rolling (RD), normal (ND) and transverse (TD) directions. In the initial (undeformed) state the ferritic matrix shows a single preferred $\{111\}\langle 110 \rangle$ orientation. For austenite there are two preferred orientations: $\{110\}\langle 001 \rangle$ and $\{110\}\langle 111 \rangle$. When applying a mechanical load in the elastic regime, for all 3 samples the $\{111\}\langle 110 \rangle$ component of the ferritic matrix remains unchanged. For the TRIP-15min sample the austenite texture remains unchanged up to the yield strength as no significant transformation takes place. For the austenite in the TRIP-2min sample however, a comparable decrease of both texture components is observed as a result of the martensitic transformation induced by shear load. This behaviour is significantly different from the behaviour observed for tensile deformation where only the $\{110\}\langle 001 \rangle$ component is suppressed under load [29].

Table 5.5: Elastic stresses in the ferritic matrix and the austenite for the DP, TRIP-2min and TRIP-15min steels at Yield strength (YS) and at Ultimate Shear Strength (USS).

Steel	Stress state	Ferritic Matrix		Austenite	
		σ_{12} (MPa)	σ_{11} (MPa)	σ_{12} (MPa)	σ_{11} (MPa)
DP	USS	343.4(4)	3.4(8)	-	-
TRIP-2min	YS	225.5(4)	104.3(3)	573(6)	99.4(8)
	USS	158.8(4)	168.3(6)	294(5)	239(4)
TRIP-15min	YS	230.9(4)	97.0(2)	561(3)	125.4(8)
	USS	330.4(4)	349.3(8)	606(9)	130(10)

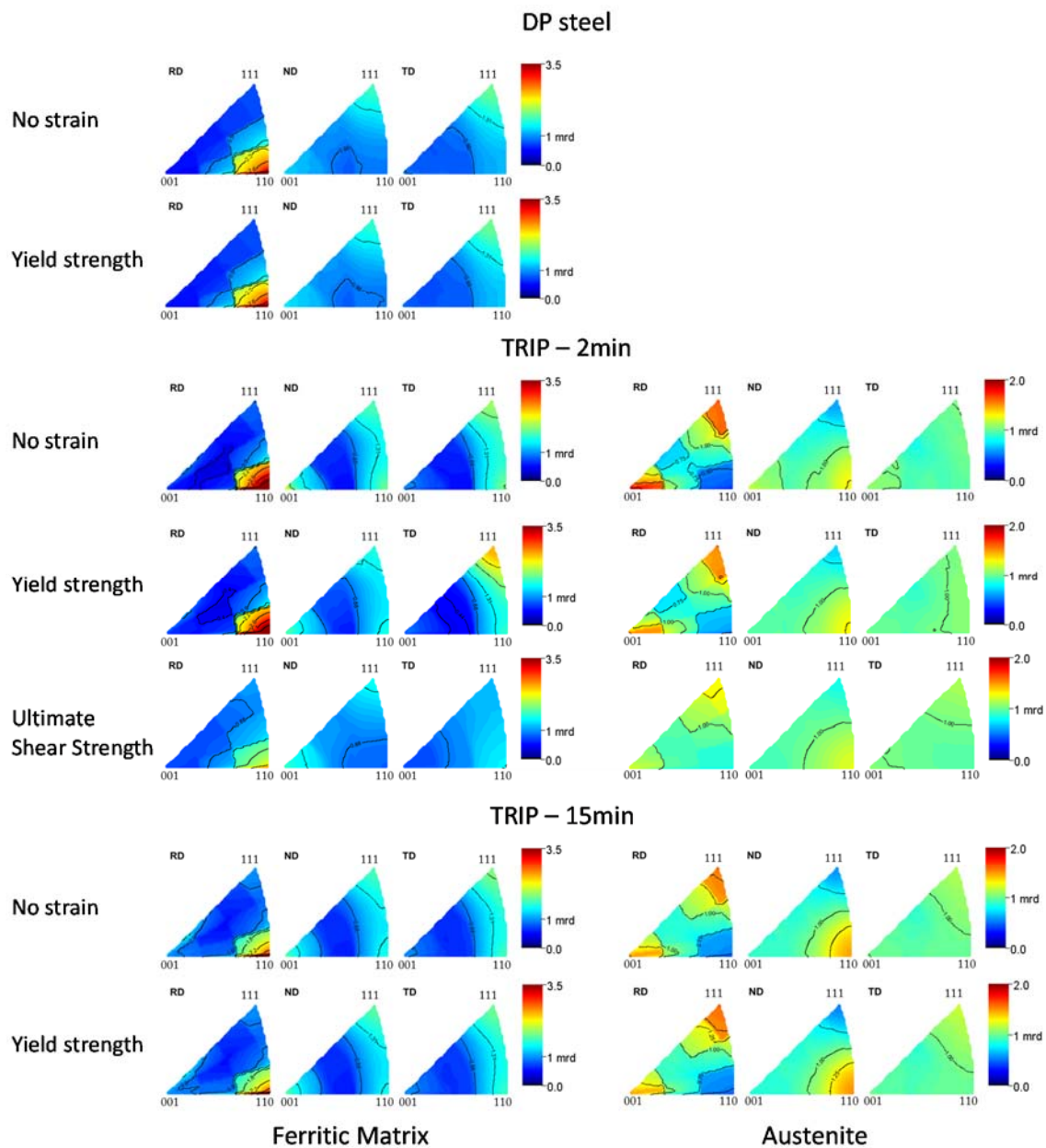


Figure 5.9: Texture evolution of the ferritic matrix and austenite represented as inverse pole figures reconstructed from the ODF's for the indicated stress states. The scale is in multiples of random distribution.

In the plastic regime, the texture of both the ferrite and austenite is significantly suppressed during the shear deformation and develops towards a fully random orientation. This is probably induced by the strongly inhomogeneous stress state that is induced at ultimate shear stress for our sample geometry. The inhomogeneity of the stress state may strongly enhance grain rotations in the centre of the shear band.

5.3.6 Comparison between shear and tensile deformation

In Fig. 5.10 a comparison is made between the relative austenite fraction of the TRIP-2min steel as a function of the relative displacement for shear load and tensile load. At room temperature the austenite is destabilised much faster under tensile load than under shear load as a function of the equivalent strain. Under shear the transformation is initially significantly delayed but shows a similar rate of transformation beyond a value of about 10%. Under tensile deformation the austenite fraction rapidly decreases until a strain of about 2.5% and then remains constant until fracture. Under shear deformation the maximum elongation is much higher. As the austenite transformation continues until fracture, a larger relative fraction is transformed. When we consider the tensile data at 153 K we observe that the relative rate of transformation is initially equal to the data at 293 K. At low temperature, however, the austenite transformation continues until fracture.

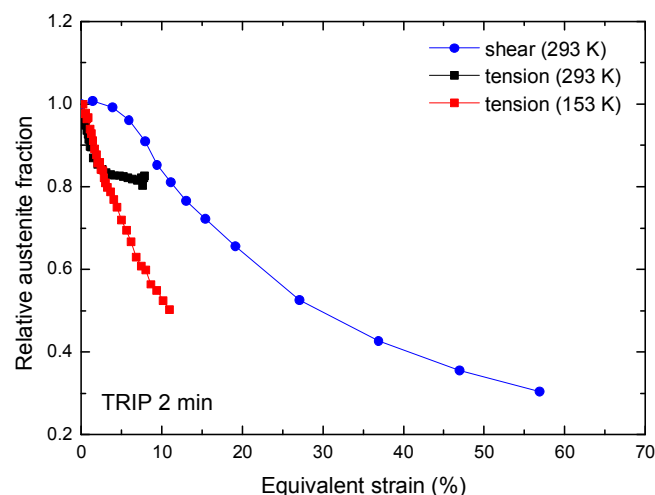


Figure 5.10: Comparison of the relative austenite fraction of the TRIP-2min steel as a function of the relative displacement for shear load ($T = 293\text{ K}$) and tensile load ($T = 293$ and 153 K).

So far limited experimental work has been done to systematically compare the austenite stability for different deformation modes. Reviews by Jacques [12], Shan [43] and Choi [44-45] indicate that simple shear shows the lowest amount of austenite transformation as a function of the equivalent plastic strain in comparison with deformation modes such as tensile loading. This is in good agreement with the data of Fig. 5.10 where the transformation under shear is significantly delayed with respect to tensile deformation.

5.4 Conclusions

We have performed in-situ synchrotron high-energy X-ray diffraction experiments in order to study the stability of metastable austenite in low-alloyed TRIP steel (TRIP-2min) during shear loading. For comparison (1) a TRIP steel with stable austenite (TRIP-15min) and (2) a dual-phase (DP) steel with the same chemical composition have also been studied. A detailed analysis of the diffraction data reveals the relevant characteristics of the martensitic transformation of metastable austenite during shear deformation. The main conclusions are:

1. Shear deformation of the TRIP-2min sample results in a relatively large transforming austenite fraction of about 75% of the initial retained austenite. The austenite transformation is found to start well below the macroscopic yield strength and to continue until rupture. The large degree of transformation however results in a limited TRIP effect with a relatively small mechanical response compared to the TRIP-15min sample with a more stable austenite. The shear modulus is found to increase for a decreasing amount of retained austenite in the TRIP-2min, TRIP-15min and the DP samples due to the increasing amount of bainite/martensite. For the retained austenite a comparable shear modulus is found for the TRIP-2min and TRIP-15min samples.
2. From the orientation dependence of the normal strain simultaneously the elastic strain and the carbon enrichment could be obtained. During shear, the carbon concentration in the remaining austenite first increases, but then stabilizes before the TRIP effect is depleted due to the progressive transformation of the least stable austenite grains into martensite.

3. The texture evolution during shear indicates that the austenite grains transform without a significant preferred orientation. The initial texture components $\{110\}\langle 001\rangle$ and $\{110\}\langle 111\rangle$ for austenite are significantly suppressed by shear loading in the plastic regime. The texture of both the ferrite and the austenite develop towards a fully random orientation.

5.5 References

- [1] O. Matsumura, Y. Sakuma, H. Takechi, *Trans. ISIJ* 27 (1987) 570.
- [2] O. Matsumura, Y. Sakuma, H. Takechi, *Scripta. Mater.* 21 (1987) 1301.
- [3] H.C. Chen, H. Era, M. Shimizu, *Metall. Trans.* 20A (1989) 437.
- [4] S. Oliver, T.B. Jones, G. Fourlaris. *Mat. Sci. Tech.* 23 (2007) 423.
- [5] O. Kwon, K. Lee, G. Kim, K.G. Chin. *Mat. Sci. Forum* 638-642 (2010) 136.
- [6] A.K. Srivastava, G. Jha, N. Gope, S.B Singh. *Mat. Charact.* 57 (2006) 127.
- [7] L. Skálová, R. Divišová, J. Jandová. *Mat. Proc. Tech.* 175 (2006) 387.
- [8] A. Kammouni, W. Saikaly, M. Dumont, C. Marteau, X. Bano, A. Charai. *Mat. Sci. Eng. A* 518 (2009) 89.
- [9] J. Chiang, B. Lawrence, J.D. Boyd, A.K Pilkey. *Mat. Sci. Eng. A* 528 (2011) 4516.
- [10] S. Zaefferer, J. Olhert, W. Bleck. *Acta Mater.* 52 (2004) 2765.
- [11] I.B. Timokhina, P.D. Hodgson, E.V. Pereloma. *Metall. Mater. Trans. A* 35A (2004) 2331.
- [12] P.J Jacques, Q. Furnémont, F. Lani, T. Pardoën, F. Delannay. *Acta Mater.* 55 (2007) 3681.
- [13] W.J. Dan, W.G. Zhang, S.H. Li, Z.Q Lin. *Comp. Mat. Sci.* 40 (2007) 101.
- [14] E. Jimenez-Melero, N.H. van Dijk, L. Zhao, J. Sietsma, S.E. Offerman, J.P. Wright, S. van der Zwaag. *Acta Mater.* 55 (2007) 6713.
- [15] L. Zhao, N.H. van Dijk, E. Brück, J. Sietsma, S. van der Zwaag. *Mat. Sci. Eng. A* 313 (2001) 145.
- [16] R. Blondé, E. Jimenez-Melero, N.H. van Dijk, E. Brück, L. Zhao, J. Sietsma, S. van der Zwaag. *Solid State Phenom.* 172-174 (2011) 196.
- [17] N.H. van Dijk, A.M. Butt, L. Zhao, J. Sietsma, S.E. Offerman, J.P. Wright, S. van der Zwaag. *Acta Mater.* 53 (2005) 5439.
- [18] E. Jimenez-Melero, N.H. van Dijk, L. Zhao, J. Sietsma, S.E. Offerman, J.P. Wright, S. van der Zwaag. *Scripta Mater.* 56 (2007) 421.
- [19] E. Jimenez-Melero, N.H. van Dijk, L. Zhao, J. Sietsma, S.E. Offerman, J.P. Wright, S. van der Zwaag. *Acta Mater.* 57 (2009) 533.
- [20] S. Kruijver, L. Zhao, J. Sietsma, E. Offerman, N. van Dijk, L. Margulies, E. Lauridsen, S. Grigull, H. Poulsen, S. van der Zwaag, *S. Steel Res.* 73 (2002) 236.
- [21] K.K. Park, S.T. Oh, S.M. Baeck, D.I. Kim, J.H. Han, H.N. Han, S.H. Park, C.G. Lee, S.J. Kim, K.H. Oh. *Mat. Sci. Forum* 408-412 (2002) 571.

- [22] O. Muránsky, P. Šittner, J. Zrník, E.C. Oliver. *Metall. Mater. Trans. A* 39A (2008) 3097.
- [23] N. Jia, Z.H. Cong, X. Sun, S. Cheng, Z.H. Nie, Y. Ren, P.K. Liaw, Y.D. Wang. *Acta Mater.* 57 (2009) 3965.
- [24] J. Jung, H. Kim, B.C. De Cooman. *ISIJ Int* 50 (2010) 620.
- [25] Y. Tomota, H. Tokuda, Y. Adachi, M. Wakita, N. Minakawa, A. Moriai, Y. Morii. *Acta Mater.* 52 (2004) 5737.
- [26] K. Asoo, Y. Tomota, S. Harjo, Y. Okitsu. *ISIJ Int* 51 (2011) 145.
- [27] Z.H. Cong, N. Jia, X. Sun, Y. Ren, J. Almer, Y.D. Wang. *Metall. Trans. A* 40A (2009) 1383.
- [28] E. Jimenez-Melero, N.H. van Dijk, L. Zhao, J. Sietsma, J.P. Wright, S. van der Zwaag. *Mat. Sci. Eng. A* 528 (2011) 6407.
- [29] R. Blondé, E. Jimenez-Melero, L. Zhao, J.P. Wright, E. Brück, S. van der Zwaag, N.H. van Dijk. *Acta Mater.* 60 (2012) 565.
- [30] F. Lani, Q. Furnémont, T. van Rompaey, F. Delannay, P.J. Jacques, T. Pardoen. *Acta Mater.* 55 (2007) 3695.
- [31] K.S. Choi, W.N. Liu, M.A. Khaleel, Y. Ren, Y.D. Wang. *Metall. Mater. Trans. A* 39A (2008) 3089.
- [32] D.D. Tjahjanto, S. Turteltaub, A.S.J. Suiker, S. van der Zwaag. *Phil. Mag.* 88 (2008) 3369.
- [33] K.S. Choi, W.N. Liu, X. Sun, M.A. Khaleel. *Acta Mater.* 57 (2009) 2592.
- [34] B.C. De Cooman. *Curr Opin Solid State Mater. Sci.* 8 (2004) 285.
- [35] H. Czychos, T. Saito, L. Smith. (2006) *Springer Handbook of Materials Measurement Methods*. Springer. Leipzig.
- [36] A.P. Hammersley, S.O. Svensson, M. Hanfland, A.N. Fitch, D. Hausermann. *High Pressure Res.* 14 (1996) 235.
- [37] J. Rodríguez-Carvajal. *Physica B* 192 (1993) 55.
- [38] L. Lutterotti, S. Matthies, H.R. Wenk. *CPD Newsletter IUCr* 21 (1999) 14.
- [39] L. Lutterotti, M. Bortolotti, G. Ischia, I. Lonardelli, H.R. Wenk. *Z Kristallogr. Suppl.* 26 (2007) 125.
- [40] I.C. Noyan and J.B. Cohen. *Residual stress: measurement by diffraction and interpretation*, Springer-Verlag, New York. (1987).
- [41] B.B. He. *Two-dimensional X-ray diffraction*, Wiley & Sons, New Jersey. (2009).
- [42] H.R. Piehler, *Fundamentals of Modeling for Metals Processing*, 22A (2009) ASM Handbook.
- [43] T.K. Shan, S.H. Li, W.G. Zhang, Z.G. Xu. *Mat. & Des.* 29 (2008) 1810.
- [44] K.S. Choi, A. Soulami, W.N. Liu, X. Sun, M.A. Khaleel. *Com. Mat. Sci.* 50 (2010) 720.
- [45] K.S. Choi, W.N. Liu, X. Sun, M.A. Khaleel. *Acta Mater.* 57 (2009) 2592.



Chapter 6

Mapping investigation during shear experiments

While earlier studies on TRIP steels focussed on the determination of the austenite to martensite decomposition in uniform deformation or thermal fields, the current research focusses on the determination of the local retained austenite-to-martensite transformation behaviour in an inhomogeneous yet carefully controlled shear loaded region of double notched TRIP and DP steel samples. A detailed powder analysis has been performed to simultaneously monitor the evolution of the phase fraction and the changes in average carbon concentration of metastable austenite together with the local strain components in the constituent phases as a function of the macroscopic stress and location with respect to the shear band. The metastable retained austenite shows a mechanically-induced martensitic transformation in the localized shear zone, which is accompanied by an increase in average carbon concentration of the remaining austenite due to a preferred transformation of the austenite grains with the lowest carbon concentration. At the later deformation stages the geometry of the shear test samples results in the development of an additional tensile component. The experimental strain field within the probed sample area is in good agreement with finite-element calculations. The strain development observed in the low-alloyed TRIP steel with metastable austenite is compared to steels with the same chemical composition containing either no austenite (a DP grade) or stable retained austenite (a TRIP grade produced at a long bainitic holding time). The transformation of metastable austenite under shear is a complex interplay between the local microstructure and the evolving strain fields.

6.1 Introduction

Low-alloyed transformation-induced-plasticity (TRIP) steels were developed in the late 1980s [1-3] and have ever since attracted significant interest for automotive applications due to their outstanding combination of high strength and formability [4-8]. At room temperature a typical TRIP steel microstructure contains three phases: ferrite, bainite and metastable austenite [9,10]. The remarkable mechanical properties of this material are attributed to the combined effect of the multiphase microstructure and the transformation of the soft metastable austenite phase into the hard martensite phase upon activation by mechanical and/or thermal stimuli. This phenomenon, called the TRIP effect, increases the work-hardening rate during plastic deformation and delays necking [11,12]. The understanding of the mechanical parameters controlling the austenite stability under complex loading conditions remains limited.

Previous in-situ studies have examined the austenite stability by applying an uniaxial tensile load at room temperature [13-17], by cooling the material below room temperature [18] and by tensile deformation at selected temperatures [19]. These experimental results led to the development of advanced micromechanical models for the multiphase TRIP microstructure [20-23]. So far, limited work has been done to investigate the structural behaviour of TRIP steels under shear loading [12] and more complicated mechanical testing conditions [24] in detail. Understanding the mechanical response of the microstructure under shear deformation is an essential step to control the sheet forming process in TRIP steels for automotive applications [25]. An accurate prediction of this process requires a deeper insight into the mechanical response in terms of the austenite-to-martensite transformation, the load partitioning between the constituent phases and the texture evolution during shear loading.

In this study, we have undertaken a spatially-resolved characterization of the austenite evolution in the deformed area during shear loading by performing in-situ high-energy synchrotron X-ray diffraction (XRD) experiments. In order to determine the austenite transformation behaviour and the local strain partitioning as a function of the distance from the central shear length, a single low-alloyed steel composition with three different microstructures has been investigated: a dual-phase (DP) steel without

austenite, a TRIP steel with stable (i.e. non-transforming) austenite (TRIP-15min) and a TRIP steel with metastable austenite (TRIP-2min). The relation between the macroscopic stress and the orientation-dependent martensitic transformation has been determined by a Rietveld refinement of the high-energy XRD data. The corresponding texture evolution in the centre of the shear band was monitored by rotation of the sample and will be discussed in Chapter 5.

6.2 Experimental methods and data analysis

6.2.1 Sample preparation

The chemical composition of the studied TRIP steel is shown in Table 6.1. Double-notched plate specimens [26] with a shear length of 1 mm and a thickness of 1 mm were machined along the hot-rolling direction of the starting sheet material. The slits are at 45° with respect to the loading direction and have a width of 0.2 mm. The loading axis of the samples was chosen parallel to the rolling direction (RD). Three different microstructures have been generated by the applied heat treatment. To start, all samples were annealed in a salt bath for 30 min at an intercritical temperature of 1143 K in order to obtain about equal fractions of austenite and ferrite. The first microstructure was obtained by a direct quench to room temperature creating a dual phase steel (DP) containing about equal amounts of ferrite (α) and martensite (α'). The other two samples were quenched in a second salt bath to a temperature of 673 K and held for either 2 min (TRIP-2min) or 15 min (TRIP-15min), respectively. During this isothermal holding the intercritical austenite transformed partly into bainite, resulting in a continuous enrichment of the interstitial carbon content in the untransformed austenite. The carbon-enriched austenite remained in a metastable state after a final water quench to room temperature. This heat treatment for the TRIP-2min and the TRIP-15min samples yielded a microstructure made of three constituents: ferrite (α), bainite (α_b) and metastable austenite (γ). In Fig. 6.1 the formed microstructures are shown.

Table 6.1: *Chemical composition of the studied samples in wt.% with balance Fe.*

C	Mn	Si	Al	P
0.218	1.539	0.267	1.75	0.018

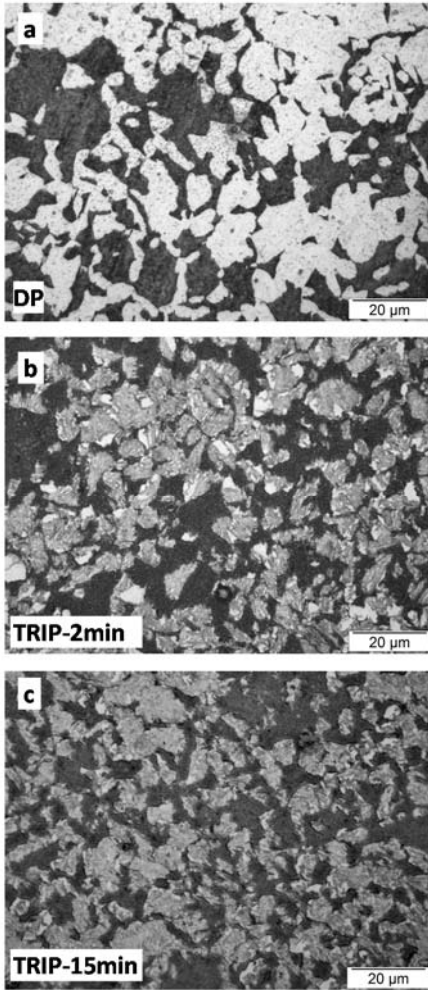


Figure 6.1: *Initial microstructure of the studied samples: (a) DP, (b) TRIP-2min and (c) TRIP-15min. The DP microstructure contains a matrix of ferrite (black) and martensite (white). The TRIP microstructure contains a metastable austenite phase (white) within a matrix of ferrite (black) and bainite (grey) phases.*

6.2.2 In-situ high-energy X-ray diffraction

The *in-situ* XRD experiments were performed at the high-energy materials science beamline (P07) of the PETRA III synchrotron radiation source at DESY (Hamburg, Germany). Fig. 6.2 shows the sample geometry and the experimental setup used for the experiments. A monochromatic X-ray beam with an energy of 79.6 keV (wavelength of 0.156 Å) and a beam size of $100 \times 100 \mu\text{m}^2$ illuminated the plate sample. For the high-energy X rays the sample absorption is relatively small, making it possible to study even 1 mm thick samples in transmission geometry. The diffracted beam was recorded on a two-dimensional digital flat panel X-ray detector (Perkin Elmer XRD 1622) placed at 1025.1 mm behind the sample.

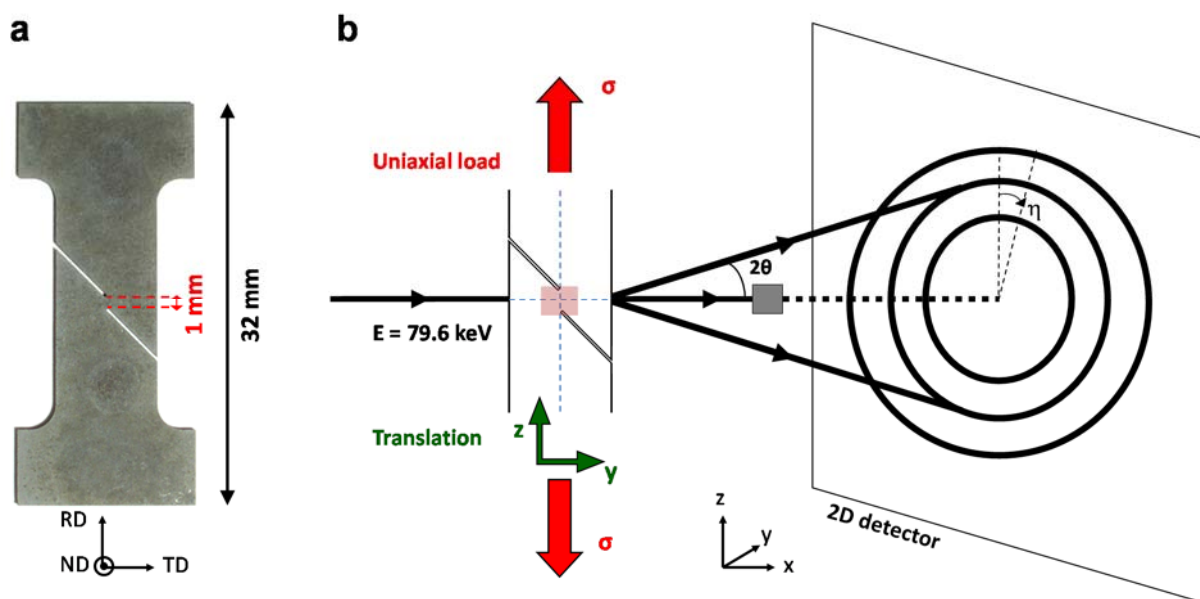


Figure 6.2: *Photography of (a) the shear specimen and (b) the experimental setup used for the high-energy microbeam X-ray diffraction experiments. The sample area of $2.1 \times 1.3 \text{ mm}^2$ scanned in steps of $100 \text{ }\mu\text{m}$ is represented by a red rectangle at the crossing of the dotted lines.*

To study the mechanical response of the constituent phases, the sample was mounted on a 2-kN micro tensile tester placed on a translation table that provided alignment of the sample in three directions with respect to the X-ray beam. During the experiment, the samples were translated along (z axis) and transverse (y axis) the loading axis in steps of $100 \text{ }\mu\text{m}$. We covered a rectangular area of $2.1 \times 1.3 \text{ mm}^2$ centred on the middle of the shear path (21 steps along y and 13 steps along z). The sample area monitored by the in-situ microbeam X-ray diffraction experiments is indicated in red in Fig. 6.2. For each deformation step the strain was held constant during a complete set of diffraction measurements over the scanned sample area. During each translation step a two-dimensional (2D) diffraction pattern was recorded using an exposure time of 0.5 s. The instrument parameters for the X-ray diffraction setup were determined using a CeO_2 calibrant (NIST SRM 674b).

6.2.3 Analysis of diffraction data

The data measured consist of a series of 273 individual 2D diffraction patterns covering the sample area of interest in (y, z) sample coordinates for each macroscopic deformation step. An integration over the azimuthal angles at constant scattering angle was performed using the FIT2D software package [27] to obtain the corresponding one-dimensional (1D) diffraction patterns. A Rietveld refinement of the

resulting one-dimensional X-ray diffraction patterns was performed using the Fullprof package [28] in order to determine the phase fraction and lattice parameter of the constituent phases as a function of the macroscopic strain. Fig. 6.3a and 6.3b shows two examples of the two-dimensional X-ray diffraction patterns with the corresponding 1D patterns analysed by the Rietveld method before and after applying a shear load. Shear deformation leads to a reduction in peak intensity for the metastable austenite phase having a face-centred cubic (fcc) structure, and an increase in the diffraction peaks for the ferritic matrix having a body-centred cubic (bcc) structure.

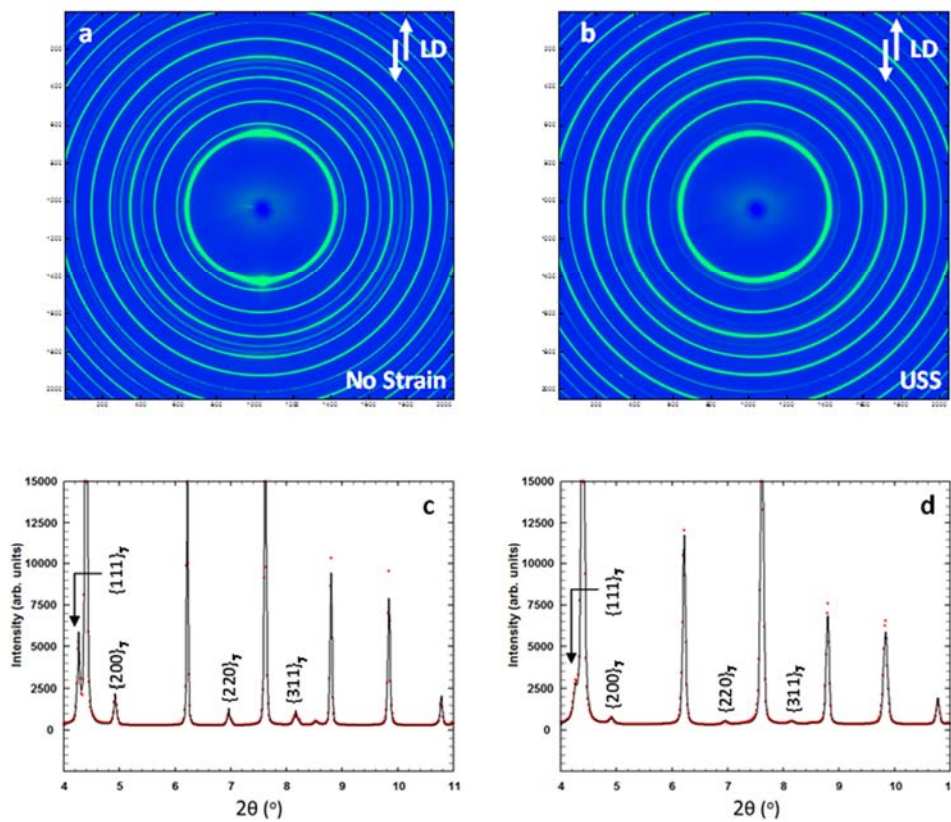


Figure 6.3: 2D X-ray diffraction patterns at (a) no strain and (b) ultimate shear strength (USS). The loading direction (LD) is indicated in the figure. The 2D patterns have been subsequently integrated over the azimuth angles to obtain the one-dimensional X-ray patterns as a function of the scattering angle at (c) no strain and (d) ultimate shear strength. The corresponding Rietveld refinement of the one-dimensional X-ray patterns is also shown. The studied $\{111\}_\gamma$, $\{200\}_\gamma$, $\{220\}_\gamma$ and $\{311\}_\gamma$ austenite reflections have been labeled on the 1D patterns.

6.2.4 Finite element modelling

In order to study the relation between the (macroscopic) tensile load applied at the grips of the specimen and the local shear deformation induced in the central section due to the slits, a two-

dimensional finite element analysis has been performed under plane stress conditions, shown in Fig. 6.4. The material behaviour is modelled using a classical J_2 -Von Mises elasto-plastic constitutive law with isotropic hardening. The model parameters are calibrated from the uniaxial stress-strain response of the same material at 293 K as reported in [19]. Consequently, the material model describes the effective behaviour of a large number of grains of all microstructural phases (austenite, ferrite, martensite). The inelastic deformation mechanisms occurring at individual phases (e.g., plastic deformation in the ferrite or phase transformation in retained austenite) are accounted for *collectively* as an effective inelastic deformation. Although the model is not intended for providing grain-scale information, it is suitable at the length scale of the specimen.

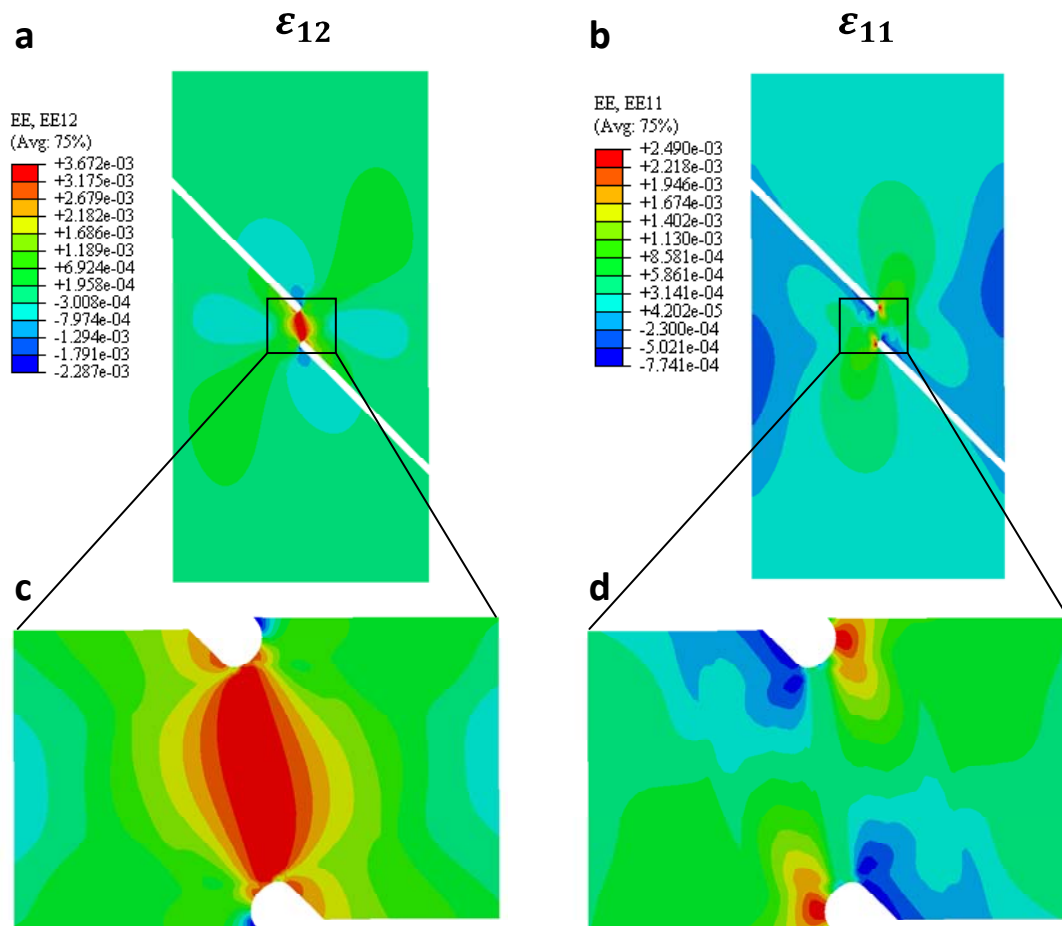


Figure 6.4: *Finite Element Method (FEM) results for the shear sample geometry at yield strength. The local shear ϵ_{12} (a) and tensile ϵ_{11} (b) strains have been represented over the full domain. The area measured by X-ray diffraction has been showed in detail for ϵ_{12} (c) and ϵ_{11} (d).*

6.3 Results and discussion

6.3.1 Macroscopic mechanical behaviour

Fig. 6.5 shows the mechanical response of the three steels deformed under shear load with a strain rate of $5.5 \times 10^{-4} \text{ s}^{-1}$. The relative displacement corresponds to the displacement of the grips normalized to the length of the shear section (1 mm) in the sample. Table 6.2 contains the relevant parameters that characterize the mechanical behaviour of the 3 samples. The difference in microstructure, resulting from the variation in bainitic holding time, results in a significant change in the mechanical response. Each sample was deformed step-wise in order to perform the X-ray diffraction experiments at constant macroscopic strain. Due to presence of about 50% of the hard martensite phase in the dual-phase steel the macroscopic stress-strain curve remains linear nearly up to fracture. The two TRIP microstructures also show a different response: the TRIP-2min sample shows a higher ultimate shear stress and a lower elongation at fracture compared to the TRIP-15min. This difference is explained by the difference in fraction and average carbon content of the retained austenite phase present. The strong sensitivity of the macroscopic mechanical response on the microstructural parameters highlights the need to understand the microstructural evolution in TRIP steels in order to control and predict their mechanical properties.

Table 6.2: *Characteristic values for the macroscopic mechanical response of the steels deformed continuously under shear load for DP, TRIP-2min and TRIP-15min steels.*

Steel	Bainitic holding time (min)	Yield Strength (MPa)	Ultimate Shear Strength (MPa)	Elongation at YS (%)	Elongation at fracture (%)
DP	0	527	630	17.1	24.4
TRIP-2min	2	324	543	10.9	54.1
TRIP-15min	15	290	495	10.1	60.4

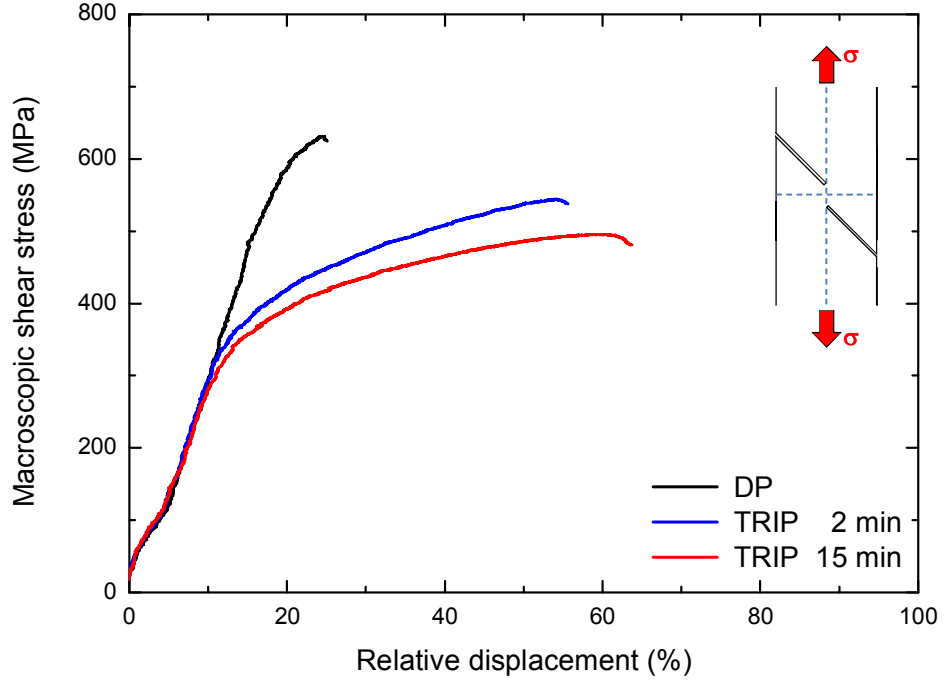


Figure 6.5: Characteristic values for the macroscopic mechanical response of the steels deformed continuously under shear load for DP, TRIP-2min and TRIP-15min steels.

6.3.2 Development of elastic shear strains

The elastic strain tensor can be determined by measuring the normal strains in various directions in the sample coordinates (1, 2, 3) = (RD, TD, -ND) [29], where RD is the rolling direction, ND the normal direction and TD the transverse direction of the plate sample. Note that RD is along the vertical loading axis and ND along the X-ray beam in the laboratory coordinate system. For this high-energy X-ray diffraction experiment in transmission geometry, the orientation-dependent normal lattice strain $\varepsilon(\eta)$ can be described as [30]:

$$\varepsilon(\eta) = \frac{a(\eta) - a_0}{a_0} \approx \left(\frac{\varepsilon_{11} + \varepsilon_{22}}{2} \right) + \left(\frac{\varepsilon_{11} - \varepsilon_{22}}{2} \right) \cos 2\eta + \varepsilon_{12} \sin 2\eta \quad (1)$$

where η is the azimuth angle on the 2D detector placed behind the sample, a_0 is the lattice parameter at zero deformation and $a(\eta)$ in the deformed state. ε_{11} , ε_{22} and ε_{12} are the components of the strain tensor ε_{ij} in sample coordinates. During deformation, the load is distributed between the austenite and the ferritic matrix. It is important to note that the relative change in the austenite lattice parameter can originate both from elastic strains and from a change in average carbon concentration. This change in

average carbon content originates from the fact that retained austenite grains with a low carbon concentration preferentially transform earliest as they have a lower stability. In this case we find:

$$\varepsilon(\eta) \approx \left(\frac{\varepsilon_{11} + \varepsilon_{22}}{2} \right) + \left(\frac{\varepsilon_{11} - \varepsilon_{22}}{2} \right) \cos 2\eta + \varepsilon_{12} \sin 2\eta + \varepsilon_C \quad (2)$$

where ε_C is the relative change in lattice parameter caused by a change in average carbon content.

For the TRIP-2 min grade the average carbon concentration in the retained austenite is lower than that in the TRIP-15 min grade and hence a stronger evolution in average carbon content is expected.

The elastic shear strain component for both phases can be estimated by $\varepsilon_{12} = [\varepsilon(45^\circ) - \varepsilon(-45^\circ)] / 2$ where $\varepsilon(45^\circ)$ and $\varepsilon(-45^\circ)$ are the relative changes in lattice parameter for an azimuth angle of $\eta = 45^\circ$ and $\eta = -45^\circ$, respectively.

Fig. 6.6 shows the spatial distribution of the local shear strain ε_{12} in the area of interest at the initial undeformed state and at ultimate shear strength (USS) for the three samples. The particular design of the sample shows a clear development of a shear strain localized along the shear length. Note that the notches are observed at the bottom right and top left of the shear strain maps. For increasing load the shear band is found to rotate about 5° - 10° with respect of the loading axis.

Fig. 6.7 shows the spatial profile of the local shear strain for the ferritic matrix and the austenite phase in the DP, TRIP-2min and TRIP-15min samples for an increasing macroscopic shear load. The curves were obtained by an integration along the loading direction covering a length of 0.5 mm around the centre on the shear length. The profile of the shear band can roughly be described by a Gaussian function. For increasing shear load the shape of the profile is largely unchanged while the maximum strain value increases linearly with the load until the yield point. Above this point a plastic deformation mode is activated where the grains are yielding and deviations from this linear behaviour are found. For the local shear strains these deviations are found to be small. At the USS the ferritic matrix of the TRIP microstructures present a shear band of about 2 mm and about 1 mm for the DP microstructure. The

corresponding maximum shear strain in the ferritic matrix is $\varepsilon_{12}^{\alpha} \approx 0.34\%$ for the DP microstructure and $\varepsilon_{12}^{\alpha} \approx 0.25\%$ for the TRIP microstructures at USS. Comparing the strain profile of the shear band in the ferritic matrix at fixed stress levels between 300 and 500 MPa, a higher maximum strain is observed at the centre of the shear band for the DP microstructure than for the two TRIP microstructures (TRIP-2min and TRIP-15min).

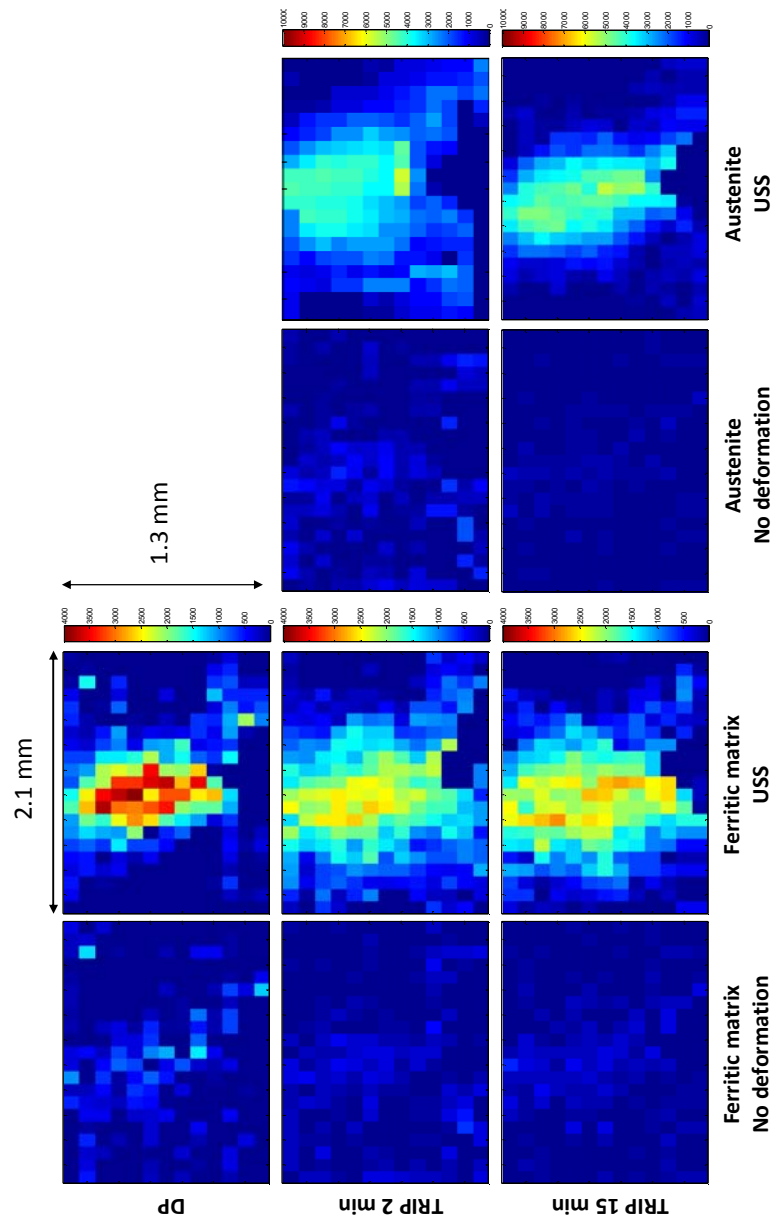


Figure 6.6: Spatial maps of the elastic shear strain ε_{12} (10^{-6}) in the ferritic matrix and the austenite at no deformation and at USS for the DP, TRIP-2min and TRIP-15min samples.

This difference can be explained from the strain partitioning with the retained austenite phase in the TRIP steels. The retained austenite in the TRIP steels is only present in a relatively low volume fraction (<10%), but shows a significantly higher shear strain than the ferritic matrix. The width of the shear band in the ferritic matrix is significantly higher for the two TRIP microstructures than for the DP microstructure for stress levels beyond 300 MPa.

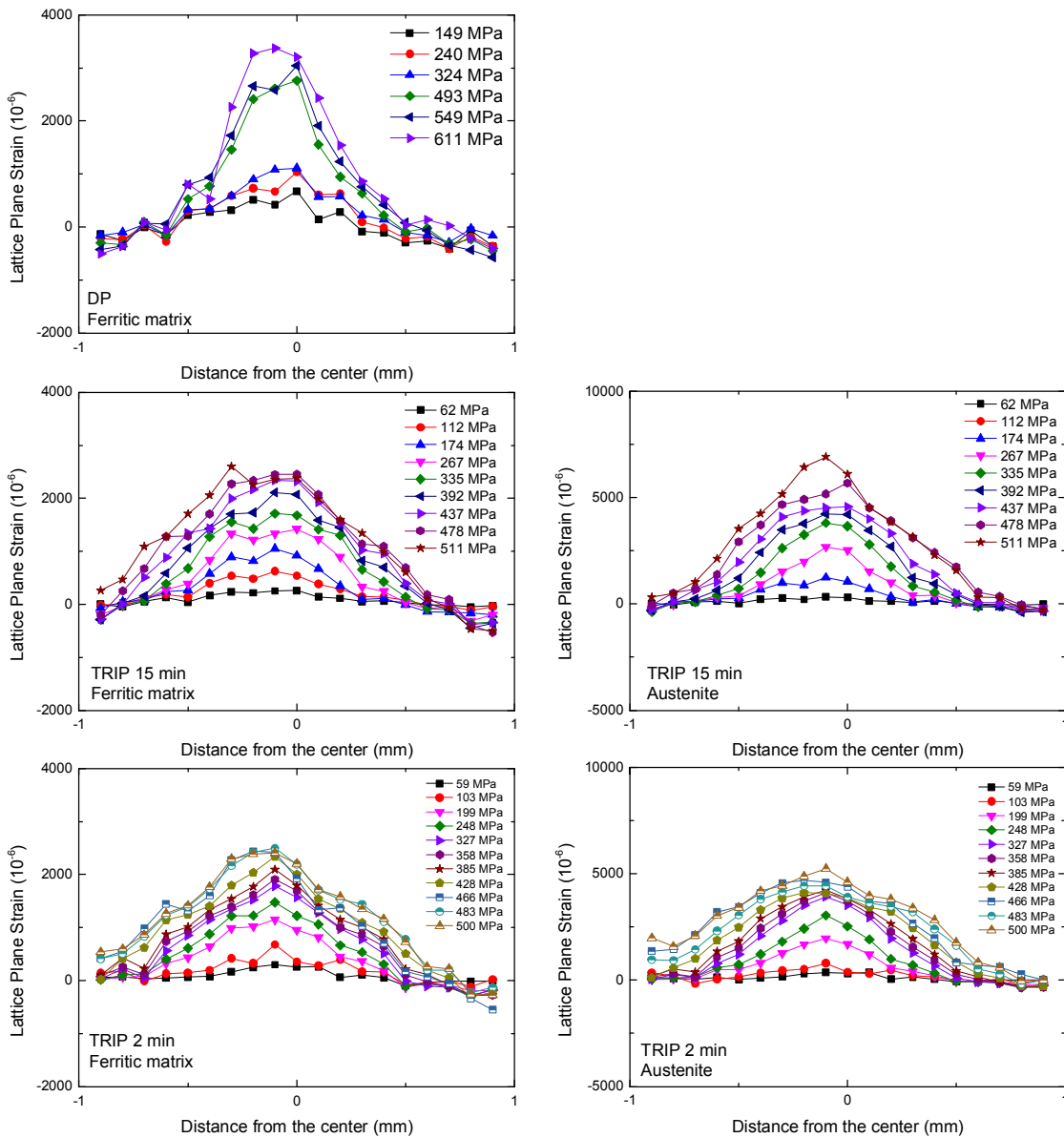


Figure 6.7: Elastic shear strain ε_{12} (10^{-6}) as a function of the distance from the middle of the shear band in the ferritic matrix and the austenite for the DP, TRIP-2min and TRIP-15min samples for the studied stress states.

As the increase in width for the TRIP samples is most pronounced beyond the yield stress, it is expected to originate from the plastic deformation, which is negligible for the DP microstructure. The width of the shear band is comparable for both TRIP samples, which indicates that their elastic properties are similar.

In the TRIP-15min microstructure, the shear band shows a similar strain profile for both the austenite phase and the ferritic matrix, as this microstructure is relatively stable during shear deformation. For the TRIP-2min sample with a metastable austenite phase the strain profiles appears to flatten for austenite at the centre of the shear band and peak for the ferritic matrix. This may be caused by a local transformation of the relatively unstable austenite into martensite in the centre of the shear band.

6.3.3 Transformation behaviour of metastable austenite

The TRIP-2min sample containing retained austenite with an optimal metastability for transformation under elastic-plastic deformation at room temperature will be studied in more detail. Fig. 6.8 shows the elastic tensile strain ε_{11} and the elastic shear strain ε_{12} , for the ferritic matrix and austenite, the austenite fraction and the change in carbon concentration in the austenite for three stress states in the TRIP-2min sample. The maximum load of 327 MPa correspond approximately to the yield point. For austenite, the tensile strain ε_{11} can be obtained by:

$$\varepsilon_{11} = \frac{\varepsilon(0^\circ) - \varepsilon(90^\circ)}{1 + \nu} \quad (3)$$

where $\nu = 0.367$ is the Poisson ratio of austenite [19]. The corresponding compressive strain amounts to $\varepsilon_{22} = -\nu\varepsilon_{11}$. The change in lattice parameter due to the evolution in average carbon content ε_C can now be estimated by:

$$\varepsilon_C = \frac{\varepsilon(45^\circ) + \varepsilon(-45^\circ)}{2} - \left(\frac{1 - \nu}{1 + \nu} \right) \frac{\varepsilon(0^\circ) - \varepsilon(90^\circ)}{2} \quad (4)$$

In the centre of the shear band only the first term significantly contributes up to the yield point.

The experimental value of ε_C can directly be used to estimate the change in carbon concentration as the austenite lattice parameter is related to chemical composition via the following relationship [18]:

$$a_\gamma = 3.556 + 0.0453x_C + 0.00095x_{Mn} + 0.0056x_{Al} \quad (5)$$

where a_γ is in Å and x_C , x_{Mn} and x_{Al} are in wt.%.

For the TRIP-2min sample the initial austenite phase has a carbon content of $x_C = 1.30(2)$ wt.%. Fig. 6.8 confirms that for the TRIP-2 min sample a shear band develops with increasing macroscopic shear load. In addition, we find that near end of the notches an additional tensile component is generated for our sample geometry. These strain components can now be correlated to the decay of the austenite phase fraction and the increase in carbon concentration in the remaining austenite. It is found that in the middle of the shear band indeed the austenite phase fraction is strongly reduced, while the carbon concentration increases significantly. The transformation of metastable austenite is however not exclusive found in the shear band but also extends to the regions with a high tensile strain close to the end of the notches. This confirms that the transformation can be induced both by shear and tensile deformation as was already shown in dedicated experiments for transformation under uniform tensile stress [19].

In Fig. 6.9 the spatial profiles of the local austenite shear strain, austenite fraction and change in average carbon concentration are shown for the TRIP-2min sample for increasing macroscopic shear load. The curves were obtained by an integration along the loading direction covering a length of 0.5 mm around the centre on the shear length. The local strain is increasing until fracture, while the austenite fraction is continuously decreasing and leads to a local increase in average carbon concentration. The carbon increase seems to saturate at a maximum value of $\Delta x_C \approx 0.15$ wt.%. The high degree of shear localization in the centre of the sample leads to a change in austenite volume fraction from about 8% prior to loading to a final volume fraction of about 3% at USS.

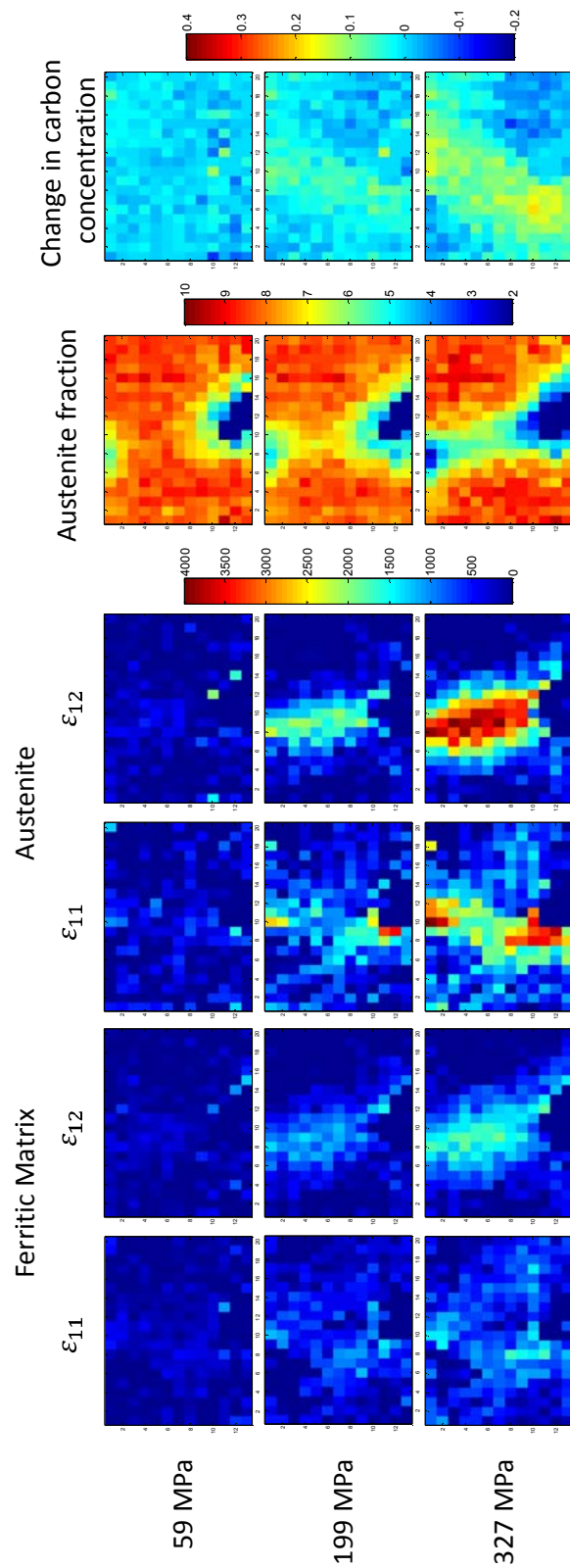


Figure 6.8: Spatial maps of the elastic shear strain ε_{12} (10^6) and tensile strain ε_{11} (10^6) for the ferritic matrix and the metastable austenite in the TRIP-2min sample at a macroscopic shear stress of 59, 199 and 327 MPa. The corresponding spatial maps of the austenite phase fraction f_γ (%) and the change in average carbon concentration in the austenite phase Δx_C (wt. %) have also been shown.

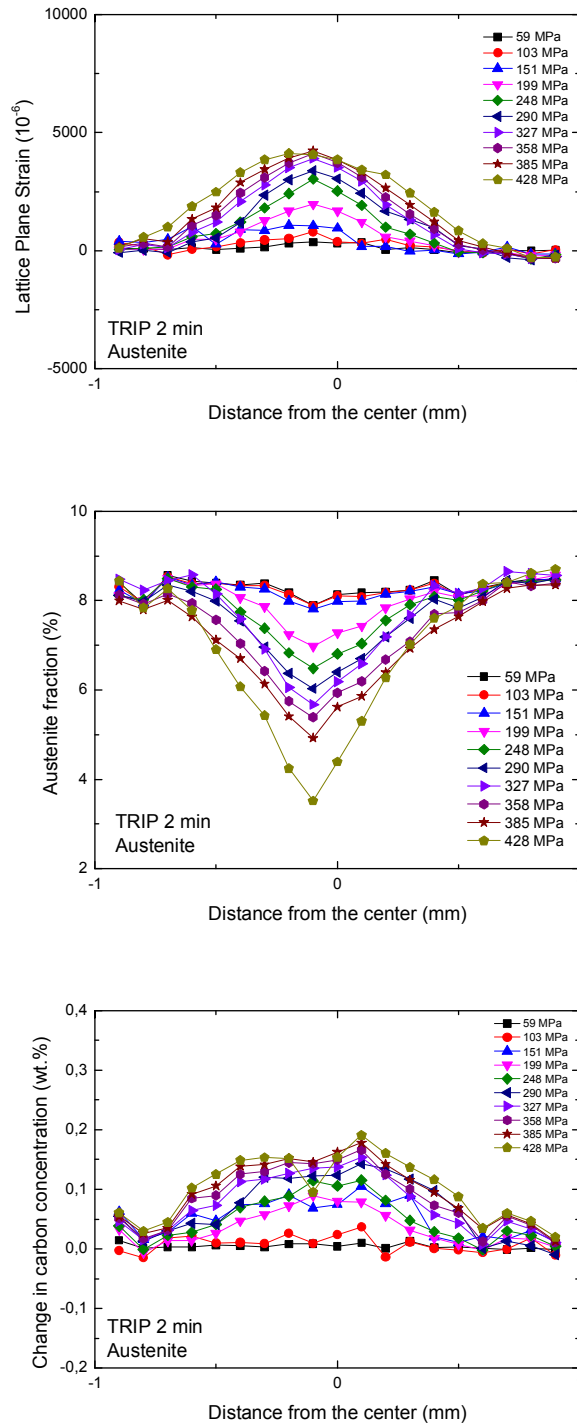


Figure 6.9: Elastic shear strain ϵ_{12} , phase fraction and change in average carbon concentration of the austenite phase in the TRIP-2min sample as a function of the distance from the middle of the shear band for the stress state studied.

6.3.4 Comparison with finite element modelling

Contour plots of the elastic strain components obtained from the finite element simulation at the macroscopic yield strength are shown in Fig. 6.4. The experimentally measured strain contours compare qualitatively well with the numerical predictions. As expected, the extension of the specimen at the grips is localized mostly as a shear deformation in a band-like region connecting the ends of the slits in the specimen (see ε_{12} component in Fig. 6.4. a &c). A similar strain state is indeed observed in the experimental data of Fig. 6.8. Outside of this banded region, the deformation is significantly smaller. Strains normal to the shear band (i.e., ε_{11} component shown in Fig. 6.4b and Fig. 6.4d) are concentrated near the ends of the slits but rapidly decay outside this region. These peak tensile regions can be purely attributed to the geometry of the shear specimen. The above arguments support that the observed phase transformation in fact takes place primarily in the regions under shear deformation. From the simulations, it is observed that the normal stress along the shear band is relatively small compared to the shear stress implying that the applied load is predominantly felt as shear force by the mid-section. This justifies the approximation of computing the average shear stress (mentioned as macroscopic shear stress in the above sections) as the total force at the grips divided by the nominal cross section of 1 mm^2 in the middle of the specimen.

6.4 Conclusions

We have performed in-situ high-energy X-ray diffraction experiments at a synchrotron source in order to correlate the austenite transformation behaviour in TRIP steels to the local strain development during shear deformation. The main conclusions are:

1. The use of a micro-beam of high-energy X-rays to scan the shear length of a double-notched specimen has proven to be a powerful method to monitor the austenite evolution under shear conditions, simultaneously with the occurrence of shear and tensile components at different sample positions relative to the shear band.

2. The maximum local shear stress and the width of the Gaussian shear band are dependent on the elastic properties of the material. The DP microstructure present the narrowest strained zone, while both the TRIP microstructures present a similar behaviour.

3. The evolution of the strain profile has been successfully simulated by finite element modelling under plane stress conditions using the classical Von Mises model. The simulations confirm the presence of strong shear strains in the centre of the shear length and the occurrence of additional tensile strains confined to the edge region of the notches.

4. The austenite fraction evolution in the TRIP-2min sample is correlated to the degree of local shear strain. The continuous austenite transformation leads to an increase in the average carbon content. The local carbon content is found to play an important role in the austenite stability under shear deformation.

6.5 References

- [1] O. Matsumura, Y. Sakuma, H. Takechi, *Trans. ISIJ* 27 (1987) 570.
- [2] O. Matsumura, Y. Sakuma, H. Takechi, *Scripta. Mater.* 21 (1987) 1301.
- [3] H.C. Chen, H. Era, M. Shimizu, *Metall. Trans.* 20A (1989) 437.
- [4] L. Skálová, R. Divišová, J. Jandová. *Mat. Proc. Tech.* 175 (2006) 387.
- [5] A.K. Srivastava, G. Jha, N. Gope, S.B. Singh. *Mat. Charact.* 57 (2006) 127.
- [6] J. Chiang, B. Lawrence, J.D. Boyd, A.K. Pilkey. *Mat. Sci. Eng. A* 528 (2011) 4516.
- [7] A. Kammouni, W. Saikaly, M. Dumont, C. Marteau, X. Bano, A. Charaï. *Mat. Sci. Eng. A* 518 (2009) 89.
- [8] S. Oliver, T. B. Jones, G. Fourlaris, *Mat. Sci. Tech.* 23 (2007) 55.
- [9] I.B. Timokhina, P.D. Hodgson, E.V. Pereloma. *Metall. Mater. Trans. A* 35A (2004) 2331.
- [10] S. Zaefferer, J. Olhert, W. Bleck. *Acta Mater.* 52 (2004) 2765.
- [11] W.J. Dan, W.G. Zhang, S.H. Li, Z.Q. Lin. *Comp. Mat. Sci.* 40 (2007) 101.
- [12] P.J. Jacques, Q. Furnémont, F. Lani, T. Pardoën, F. Delannay. *Acta Mater.* 55 (2007) 3681.
- [13] Y. Tomota, H. Tokuda, Y. Adachi, M. Wakita, N. Minakawa, A. Moriai, Y. Morii, *Acta Mater.* 52 (2004) 5737.
- [14] O. Muránsky, P. Šittner, J. Zrník, E.C. Oliver, *Metall. Mater. Trans. A* 39A (2008) 3097.
- [15] Z.H. Cong, N. Jia, X. Sun, Y. Ren, J. Almer, Y.D. Wang, *Metall. Trans. A*, 40A (2009) 1383.
- [16] K. Asoo, Y. Tomota, S. Harjo, Y. Okitsu. *ISIJ Int.* 51 (2011) 145.

- [17] N. Jia, Z.H. Cong, X. Sun, S. Cheng, Z.H. Nie, Y. Ren, et al. *Acta Mater.* 57 (2009) 3965.
- [18] N.H. van Dijk, A.M. Butt, L. Zhao, J. Sietsma, S.E. Offerman, J.P. Wright, S. van der Zwaag, *Acta Mater.* 53 (2005) 5439.
- [19] R. Blondé, E. Jimenez-Melero, L. Zhao, J.P. Wright, E. Brück, S. van der Zwaag, N.H. van Dijk, *Acta Mater.* 60 (2012) 565.
- [20] K.S. Choi, W.N. Liu, M.A. Khaleel, Y. Ren, Y.D. Wang. *Metall. Mater. Trans. A.* 39A (2008) 3089.
- [21] K.S. Choi, W.N. Liu, X. Sun, M.A. Khaleel, *Acta Mater.* 57 (2009), 2592.
- [22] F. Lani, Q. Furnémont, T. Van Rompaey, F. Delannay, P.J. Jacques, T. Pardoen, *Acta Mater.* 55 (2007) 3695.
- [23] D.D. Tjahjanto, S. Turteltaub, A.S.J. Suiker, S. van der Zwaag, *Phil. Mag.* 88 (2008) 3369.
- [24] G. Lacroix, T. Pardoen, P.J. Jacques, *Acta Mater.* 56 (2008) 3900-3913.
- [25] B. C. De Cooman, *Curr. Opin. Solid State Mater. Sci.* 8 (2004) 285.
- [26] H. Czichos, T. Saito, L. Smith, *Springer Handbook of Materials Measurement Methods.* Springer. Leipzig (2006).
- [27] A. P. Hammersley, S. O. Svensson, M. Hanfland, A. N. Fitch, D. Hausermann, *High Pressure Res.* 14 (1996) 235.
- [28] J. Rodríguez-Carvajal, *Physica B.* 192 (1993) 55.
- [29] I.C. Noyan, J.B. Cohen, *Residual stress: measurement by diffraction and interpretation.* Springer-Verlag, New York (1987).
- [30] B. B. He, *Two-dimensional X-ray diffraction.* Wiley & Sons, New Jersey (2009). [39] B. B. He, *Two-dimensional X-ray diffraction.* Wiley & Sons, New Jersey (2009).



Chapter 7

Individual grain analysis during tensile test

The stability of individual metastable austenite grains in low-alloyed TRIP steels during tensile loading has been studied using high-energy X-ray diffraction. A method of analysis based on Friedel pairs has been employed to correlate the macroscopic behaviour in the material to the microstructural parameters of individual grains. For individual grains the carbon concentration, the grain volume and the grain orientation with respect to the loading direction were determined from the diffractograms. Our results show that these three parameters control the mechanical stability, with the grain volume being the dominant parameter. The orientation-dependent stability of austenite grains depends on their Schmid factor with respect to the loading direction. Most austenite grains transform into martensite in a single transformation step once a critical load is obtained. This present study reveals the complex interplay of microstructural parameters on the mechanical stability of individual austenite grains.

7.1 Introduction

Low-alloyed Transformation Induced Plasticity (TRIP) steels were developed in the late 80s [1-4] and have attracted significant interest for automotive applications due to their outstanding combination of high strength and formability [5-7]. A typical TRIP steel microstructure contains three phases at room temperature: ferrite, bainite and metastable austenite [8, 9]. The remarkable mechanical properties of this material are attributed to the multiphase microstructure as well as to the transformation of the soft metastable austenite phase into the hard martensite phase upon activation by mechanical and/or thermal stimuli. This latter phenomenon, called the TRIP effect, increases the work-hardening rate during plastic deformation and delays necking [10-15]. In previous in-situ studies the average retained

austenite behaviour was either studied as a function of the undercooling (defining the thermal stability) [16-18] or as a function of the applied load at a fixed temperature (defining the mechanical stability) [19-26]. An accurate prediction of the material's mechanical response upon thermal, mechanical and thermo-mechanical loading requires detailed knowledge at the single grain scale, level of the interplay between the transformation behaviour, the microstructural parameters and grain orientation evolution as a function of the uniaxial load. In our previous synchrotron X-ray diffraction studies we have probed the austenite transformation behaviour at the level of single grains located in the bulk of the sample during deformation at room temperature [27], at low temperatures [28] and during cooling down to 100 K [18,29,30,31]. Such experimental results play an important role in the development of micro-mechanical models for the mechanical and transformation behaviour of TRIP multiphase microstructures [32-35]. The method is based on a detailed modelling of the relevant microstructural phenomena at the lowest dimensional levels with a subsequent upscaling to coarser scales via appropriate homogenization techniques. Hence, these models require accurate experimental data describing the behaviour of individual phases and grains in order to calibrate the models at the lowest scale properly. In the present work, a detailed in-situ characterization of the mechanical stability of individual retained austenite grains has been performed by high energy synchrotron X-ray diffraction (XRD) during tensile loading. The interplay between tensile deformation, the orientation of the dominant transformation slip planes, the grain size and the carbon content, all at the level of individual austenite grains is analyzed in great detail using an analysis method based on Friedel pairs [36,37].

7.2 Experimental methods

7.2.1 Sample preparation

The chemical composition of the TRIP steel studied is shown in Table 7.1. Cylindrical dog-bone tensile specimens with a gauge length of 10 mm and a diameter of 1 mm were carefully machined from hot rolled sheet material. The cylindrical axis of the samples was taken parallel to the rolling direction (RD). The samples were annealed in a salt bath at an intercritical temperature of 1143 K for 30 min in order to obtain equal fractions of austenite and ferrite. Then the samples were quenched in a second salt bath to a temperature at 673 K and held for 2 min. During this holding time part of the intercritical austenite

transformed into bainite, while the remaining austenite was enriched in carbon. The carbon-enriched austenite remained in a metastable state after a final water quench to room temperature. This heat treatment yielded a multiphase microstructure composed of ferrite (α), bainite (α_b) and metastable austenite (γ), as shown in the optical micrograph of Fig. 7.1.

Table 7.1: Chemical composition of the TRIP steel in wt.% with balance Fe.

C	Mn	Si	Al	P
0.218	1.539	0.267	1.75	0.018

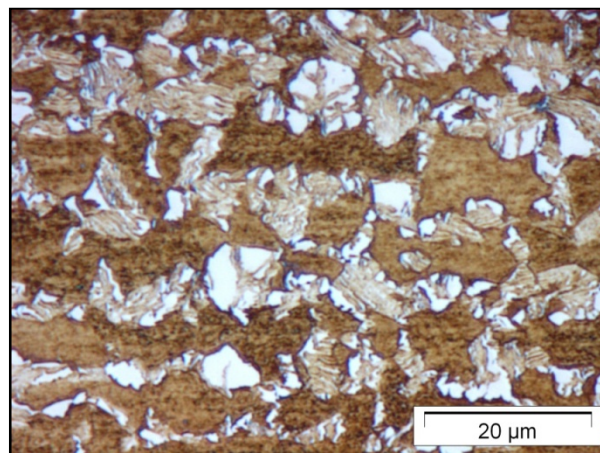


Figure 7.1: Optical micrograph of the low-alloyed TRIP steel. The room temperature multiphase microstructure contains a metastable austenite phase (white) within a matrix of ferrite (dark brown) and bainite (light brown) phases.

7.2.2 In-situ high-energy X-ray diffraction

The in-situ XRD experiments were performed at the 3D X-ray diffraction microscope at the ID11 beam line of the European Synchrotron Radiation Facility (Grenoble, France). Fig. 7.2 shows the used experimental setup. A monochromatic X-ray beam of 88 keV (wavelength of 0.141 Å) and a beam size of 20×20 , 30×30 , 40×40 , and $100 \times 100 \mu\text{m}^2$ illuminated the cylindrical sample. For these high-energy X-rays the absorption is relatively small making it possible to study even 1 mm thick samples in transmission. The diffracted beam was recorded onto a two dimensional (2D) CCD detector (FRELON) [38] placed behind the sample at 352.5 mm. For each beam size, the sample was rotated continuously around the cylindrical axis perpendicular to the X-ray beam in steps of $\Delta\omega = 0.25^\circ$ covering an angular

range of 84° at the front and back side of the sample. For each rotation step a 2D diffraction pattern was recorded using an exposure time of 0.2 s. In addition to the base beam size of $20 \times 20 \mu\text{m}^2$, others scans were performed with bigger dimensions of $30 \times 30 \mu\text{m}^2$ and $40 \times 40 \mu\text{m}^2$, to test whether the grains were completely illuminated by the X-ray beam. A beam size of $100 \times 100 \mu\text{m}^2$ was used for the powder data analysis [28]. The instrument parameters of the 3D X-ray diffraction microscope were determined using a CeO_2 calibrant (NIST SRM 674b).

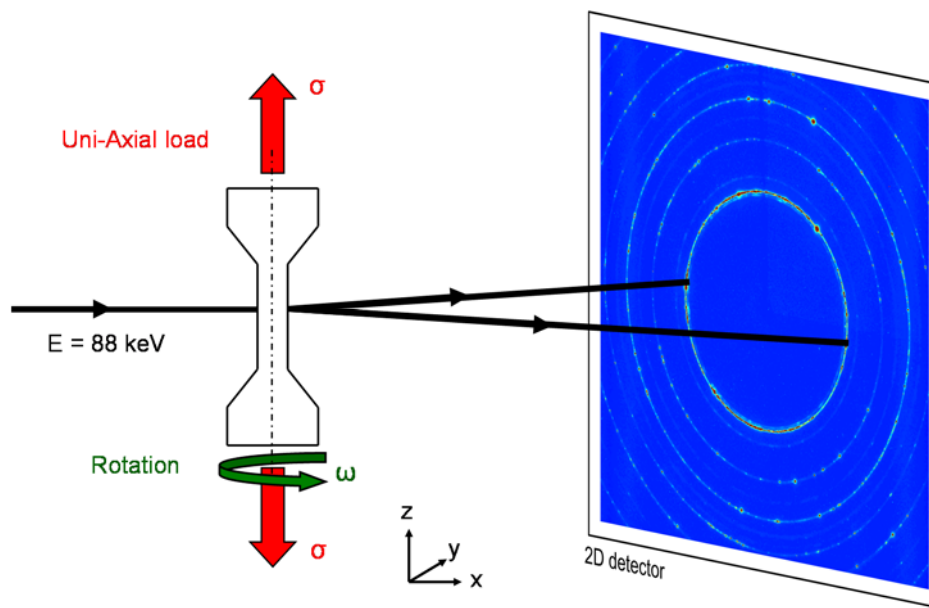


Figure 7.2: Schematic representation of the experimental setup used for the high-energy microbeam X-ray diffraction experiments. The sample was rotated around the vertical axis perpendicular to the beam.

To study the mechanical stability of the retained austenite, the sample was mounted on a 2 kN micro tensile tester placed on a translation table that provided alignment of the sample in three directions with respect to the X-ray beam and allowed ω rotation along the cylindrical axis of the sample (the loading direction was along the sample axis). After each deformation step, the strain was held constant and the originally illuminated sample volume was retraced by performing scans of the horizontal sample position, the vertical sample position and the sample rotation angle. For this purpose, the intensity of a specific diffraction spot from a characteristic non-transforming ferrite grain was used. After sample repositioning, the diffraction pattern was recorded as a function of ω for the three beam sizes mentioned. Precise information on the sample-to-detector distance during deformation was obtained

by analyzing the X-ray diffraction patterns related to a small CeO_2 calibrant placed on the sample surface.

7.2.3 Data analysis

A new method to determine the grain orientation, the grain position and an accurate value for the lattice parameter has been developed. The experimental data consist of a series of two-dimensional diffraction patterns as a function of sample elongation, ω -angle and beam size. The grains that fulfilled the Bragg condition generated one or more diffraction spots on the 2D detector. Due to the micrometer sized dimensions of the X-ray beam and the limited angular rotation for each exposure, separate diffraction spots appear on the austenite and ferrite diffraction rings, as shown in Fig. 7.3.

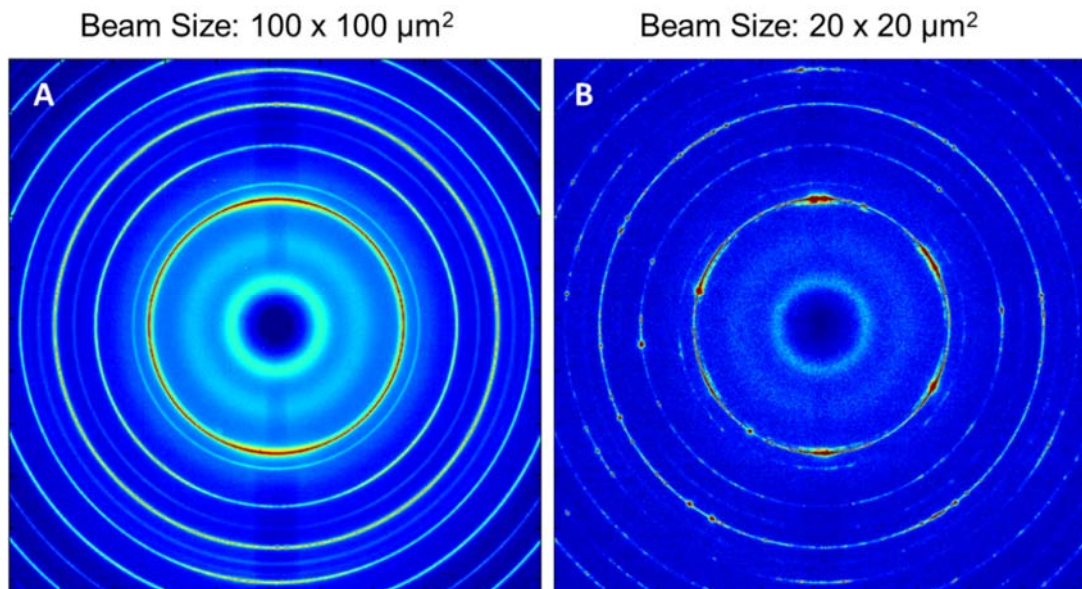


Figure 7.3: (a) Two-dimensional X-rays diffraction pattern using a beam of $100 \times 100 \mu\text{m}^2$ showing a powder pattern (b) and a beam of $20 \times 20 \mu\text{m}^2$ showing single reflections.

Each austenite diffraction ring consists of a number of single spots originating from individual austenite grains in the TRIP microstructure, together with a weak powder signal stemming from austenite grains whose volume falls below the experimental detection limit for individual grains, estimated to be about $5 \mu\text{m}^3$. The spots from the $\{200\}$, $\{220\}$ and $\{311\}$ austenite reflections with a face-centered cubic (fcc) structure have been indexed and reported in the detector coordinates $(2\theta, \eta, \omega)$ [39].

The \bar{Q} -vector for an individual peak is given by [36, 37]:

$$\bar{Q} = \frac{2\pi}{\lambda} \begin{pmatrix} \cos(\omega) & \sin(\omega) & 0 \\ -\sin(\omega) & \cos(\omega) & 0 \\ 0 & 0 & 1 \end{pmatrix} \begin{pmatrix} \cos(2\theta) - 1 \\ -\sin(2\theta) \sin(\eta) \\ \sin(2\theta) \cos(\eta) \end{pmatrix} \quad (1)$$

where λ is the wavelength of the X-rays beam and 2θ , η , ω are the detector coordinates of the diffraction peak. Using the Friedel reflection-pairs that probe the same diffracting plane at \bar{Q} and $-\bar{Q}$, the center-of-mass position of the grain within the sample can be obtained. This results in a more accurate determination of the d -spacing of the diffracting plane and the related lattice parameter. The grain orientation has also been obtained using two different Friedel pairs from the same individual grain. For the {200} austenite reflections the (± 200) , (0 ± 20) and (00 ± 2) diffraction pairs of the face-centred cubic lattice structure have perpendicular \bar{Q} -vectors:

$$\bar{Q}_{\{200\} pair 1} \cdot \bar{Q}_{\{200\} pair 2} = 0 \quad (2)$$

To obtain a higher accuracy in the grain orientation and the grain position, the software packages Fable 2.0 and ImageD11 were used to combine an average number of 20 from different $\{hkl\}$ reflections originating from the same grain. This method gives more detailed information on the grain orientation and characteristics than can be obtained from just the {200} diffraction spots, but requires more peaks from the same grain to be identified. Therefore, it means that only diffracting grains located near the centre of the sample could be analysed. Grains located further away from the centre would not always be in the (narrow) beam and hence would not always show up in the diffractogram. Consequently, a lower number of individual grains could be tracked as a function of the macroscopic strain during tensile deformation.

The grain volume of each grain (obtained from the collection of diffraction peaks) has been determined using the integrated intensity I_g of the grain by a scaling to the powder intensity of the corresponding diffraction ring:

$$V_g = \frac{1}{2} m \Delta\omega \cos(\theta) f^\gamma V_{gauge} \frac{I_g}{I_p} \quad (3)$$

where m is the multiplicity factor of the $\{hkl\}$ ring of austenite, $\Delta\omega$ is the angular range over which the grain is rotated, f^γ is the volume fraction of the austenite phase determined from the powder data analysis, V_{gauge} is the gauge volume, which is defined by the beam size and the thickness of the sample and I_p is the powder intensity of the complete $\{hkl\}$ ring.

7.3 Results and discussion

7.3.1 Macroscopic behaviour & phase fraction evolution

Fig. 7.4a shows the macroscopic stress-strain curve of the low-alloyed TRIP steel. The markers (solid spheres) indicate the strain levels at which the X-ray diffraction measurements were performed. The macroscopic strain is held constant while the 2D diffraction patterns are collected for the covered ω -rotation range. We recorded the diffraction patterns for a series of elongation steps up to a stress of about 400 MPa. The TRIP steel presents a yield strength of 206 MPa, a uniform elongation of 6.6%, an ultimate tensile strength of 519 MPa and an elongation at fracture of 8.1%.

The austenite phase fraction was derived using a powder data analysis procedure presented in a previous work [28]. Fig. 7.4b shows the austenite fraction as a function of the macroscopic strain. The austenite fraction decreases progressively with increasing strain due to the mechanically induced austenite transformation. The austenite starts to transform well before the macroscopic yield stress is reached.

7.3.2 Initial microstructure

The TRIP microstructure contains two types of austenite grains [5,9]: (i) “film-type” austenite located between the bainite plates with a volume below $1 \mu\text{m}^3$, Due to the combination of their small size and high carbon concentration (and rigid surroundings) these retained austenite grains are extremely stable and do not transform upon loading. (ii) “blocky-type” metastable austenite grains with micron-scale dimensions ($>5 \mu\text{m}^3$) and a lower carbon concentration. The present method only treats the behaviour of “blocky-type” grains. Fig. 7.5 displays the austenite lattice parameter, and the corresponding carbon content, as a function of the grain volume at no deformation. The austenite lattice parameter is related to the grain’s chemical composition [18,40]:

$$a_{\gamma} = 3.556 + 0.0453x_c + 0.00095x_{Mn} + 0.0056x_{Al} \quad (4)$$

where a_{γ} is the austenite lattice parameter in Å and x_c , x_{Mn} and x_{Al} are the alloying concentrations in wt.%. For this steel composition the effect of Si and P on the lattice parameter of austenite is ignored. Fig. 7.5 shows the volume and carbon concentration of all individual grains analysed. There is quite some variation in grain volume and a smaller variation in carbon concentration. Generally the carbon concentration reaches higher values at smaller grain volumes. The distribution in carbon levels and grain size reflects the combined effects of variation in austenite grain size prior to the bainite formation and local variation of bainitic stasis due to interacting transformation fronts. For the grain volume the experimental values range from 5 to $52 \mu\text{m}^3$ and for the carbon concentration from 0.7 to 1.5 wt.%. Comparable values have been observed in previous studies on similar steels [29-31].

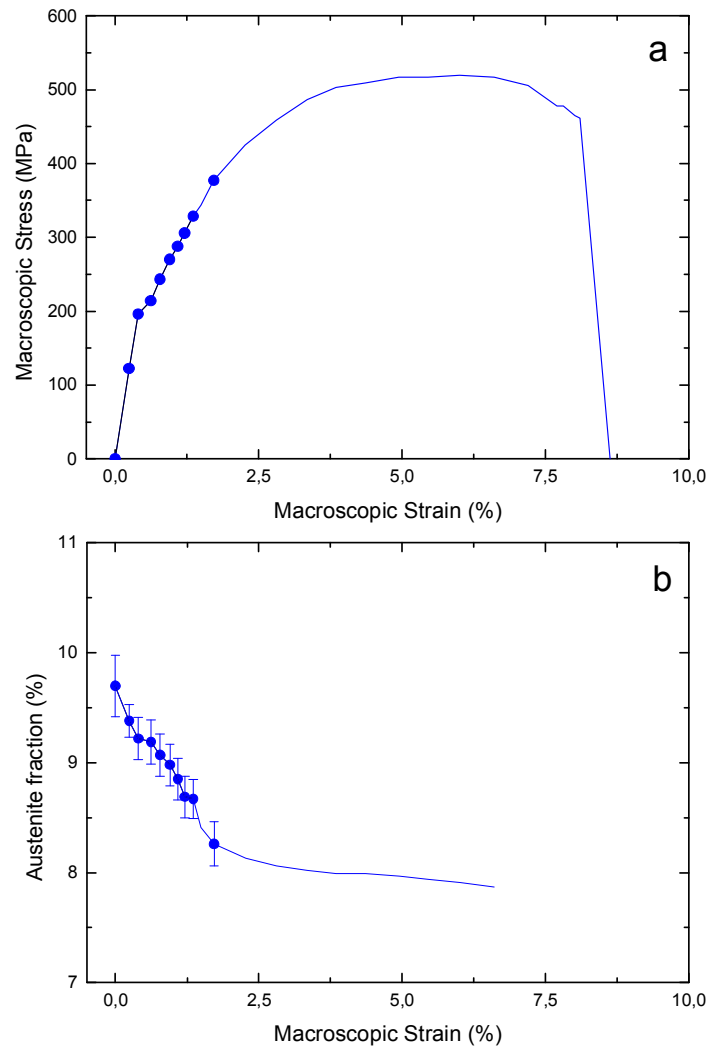


Figure 7.4: (a) Macroscopic (engineering) stress-strain curves of TRIP steel during the in situ X-ray diffraction experiments. The markers (solid spheres) represent the single grain experimental data. (b) Austenite fraction as a function of the macroscopic strain determined from a Rietveld refinement of the powder data [28].

7.3.3 Microstructure evolution

7.3.3.1 Carbon content and grain size

Fig. 7.6 shows the carbon concentration of individual grains as well as the grain volume distribution at three stages: the initial stress-free state (0 MPa), a stress state close to the macroscopic yield point (196 MPa) and a state where a significant plastic deformation has taken place (243 MPa) (see Fig. 7.4). The powder diffraction data analysis reveals that the retained austenite fraction decreases linearly with the macroscopic strain as a result of the mechanically induced austenite-to-martensite transformation.

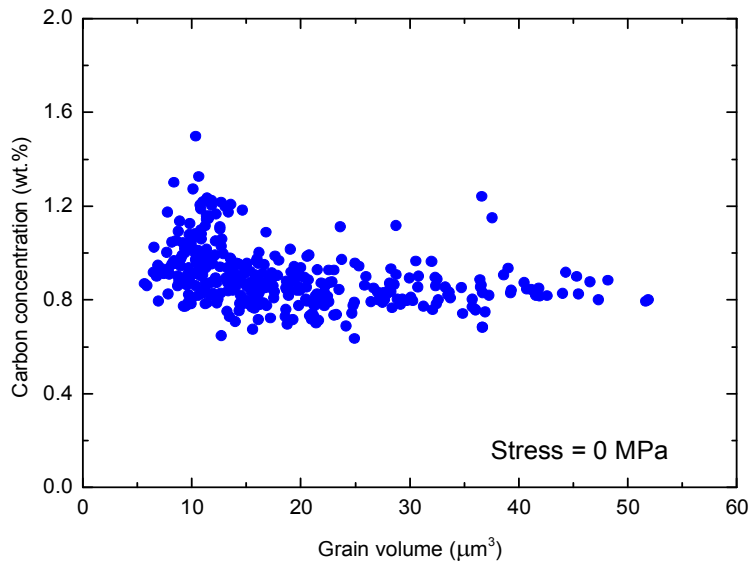


Figure 7.5: Carbon content of the individual austenite grains as a function of their grain volume at no deformation characterized as determined using single Friedel pairs.

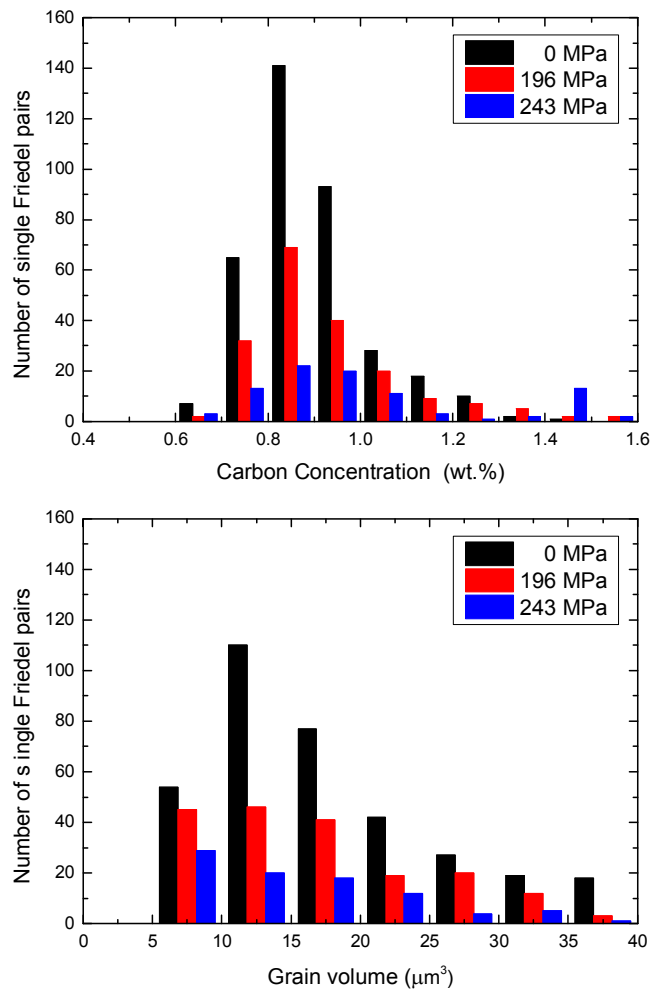


Figure 7.6: Number of austenite grains above the detection limit ($5 \mu\text{m}^3$) at a stress of 0, 196 and 243 MPa as a function of the grain volume and carbon concentration

The single grain analysis shows that the total volume fraction of austenite with a volume higher than $5 \mu\text{m}^3$ in the unstrained sample is around 5.7(1) %, which represents 58% of the initial austenite fraction. For an applied load of 243 MPa (or strain of 0.78%), the powder and single grain analysis reveal that around 0.7% of austenite has transformed. Figure 7.6 shows that transformation occurs for all grain sizes, but the probability of transformation seems a little higher for larger grains. Earlier studies involving straining at room temperature and low temperatures [29-31] showed a similar effect, with a slightly higher probability of larger grains to transform preferentially at lower temperatures. As reported in Table 7.2 and figures 7.6a and 7.6b, the average grain size decreases with applied tensile stress, while the average carbon concentration in the remaining population increases. The distribution in carbon concentration roughly corresponds to a Gaussian function with an average value (at the maximum) of about 0.9 wt.%, which increases slightly with increasing tensile load. The average grain size, however, is more strongly affected by the applied stress. As the grain average volume shows a more pronounced change, it is considered to be the dominant parameter governing the mechanical stability.

Table 7.2: *The average carbon content and grain size of the untransformed austenite grains as a function of the macroscopic stress determined from the single Friedel pairs analysis. The yield stress is about 200 MPa. The width of the distribution (standard deviation) is indicated in parenthesis.*

Stress (MPa)	Pairs number (-)	Average carbon concentration (wt.%)	Average grain volume (μm^3)
0	365	0.90(0.12)	19.13(10.9)
196	188	0.93(0.16)	17.15(8.5)
243	90	1.00(0.24)	15.30(8.1)

7.3.3.2 Grain orientation

While the minimal stress required to induce the martensitic transformation of individual austenite grains depends on grain volume as well as carbon content, the mechanically-induced transformation also depends on the grain orientation with respect to the loading direction. We assume that the transformation is controlled by the critical resolved shear stress τ induced by the macroscopic tensile load σ that initiated slip on preferred crystallographic planes.

The orientational stability is defined by the Schmid factor m which relates τ to σ [40]:

$$\tau = m\sigma = \cos(\lambda)\cos(\phi)\sigma \quad (5)$$

where λ is the angle between the tensile orientation and the slip plane normal and ϕ the angle between the tensile orientation and the slip direction. In the case of a face-centered cubic (fcc) structure, the slip plane is the {111} plane and the slip direction is the $\langle 110 \rangle$ which defines 12 independent slip systems. The resolved shear stress has been analyzed in Fig. 7.7 in terms of the inverse pole figure. For the 12 options considered the slip system giving the least stable orientation had a calculated Schmid factor between 0.27 and 0.5.

In Fig. 7.8, the grain orientation as determined from two perpendicular {200} Friedel pairs originating from the same grain are reported in an inverse pole figure colour coded as a function of the Schmid factor. The initial texture of the blocky-type austenite grains is weak. For an increasing macroscopic stress state, the transformation preferentially occurs for the grains with the highest Schmid factor. At the stage where the TRIP phenomenon is depleted, the average Schmid factor has decreased from 0.44 to 0.41 (Table 7.3). While almost all of the grains with a Schmid factor higher than 0.43 have transformed, a particular grain having a Schmid factor of 0.49 has survived, which suggests that the grain stability depends not only on its carbon content, grain size, and Schmid factor, but also on the resistance to plastic flow of the surrounding microstructure.

Table 7.3: *The average Schmid factor of the untransformed austenite grains as a function of the macroscopic stress determined from the perpendicular Friedel pairs analysis. The yield stress is about 200 MPa. The width of the distribution (standard deviation) is indicated in parenthesis.*

Stress (MPa)	Perpendicular pairs number (-)	Average Schmid factor
0	128	0.44(4)
196	26	0.42(6)
243	5	0.41(6)

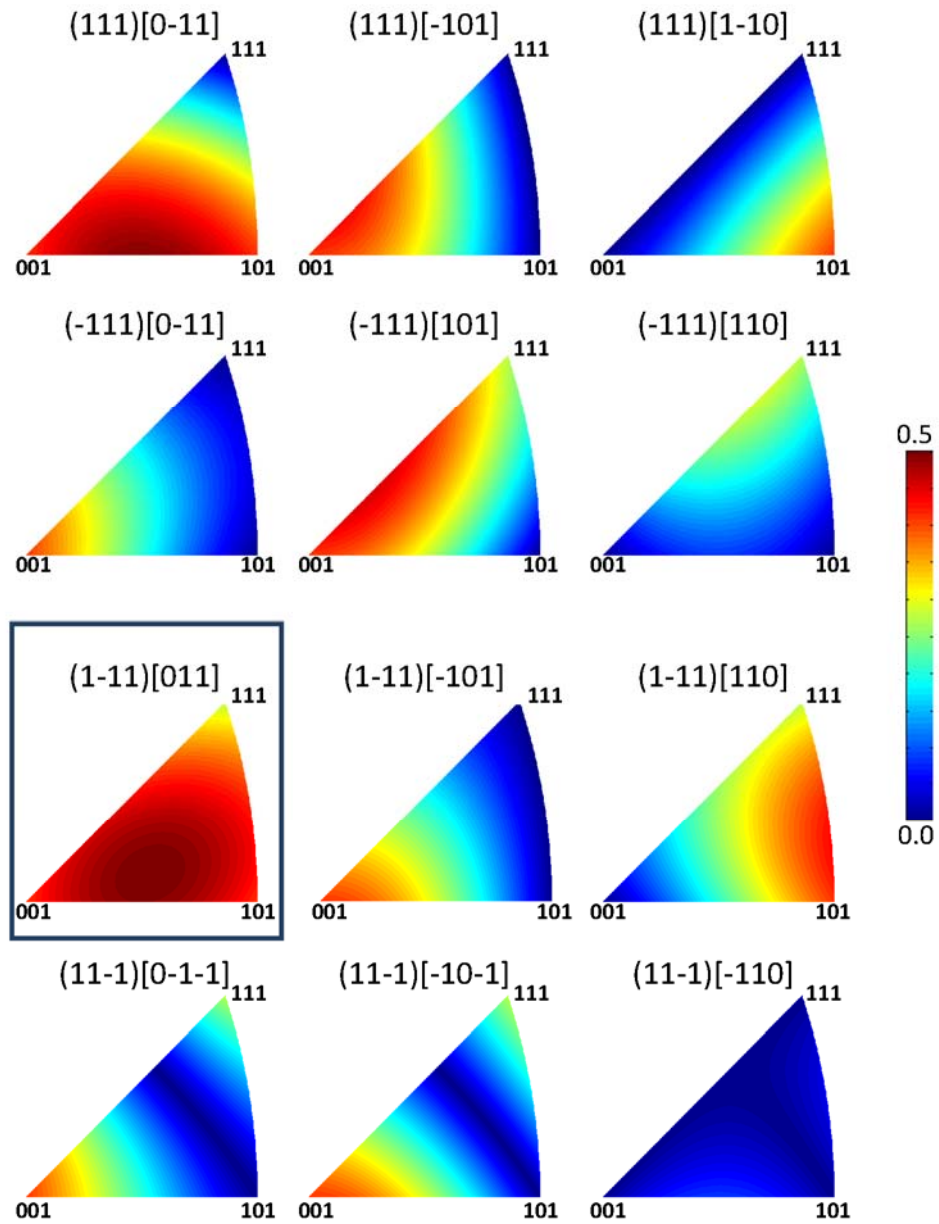


Figure 7.7: Orientation dependence of the resolved shear stress derived by the tensile stress represented in an inverse pole figure as a function of the loading direction for the 12 slip systems for the martensite transformation in the metastable austenite.

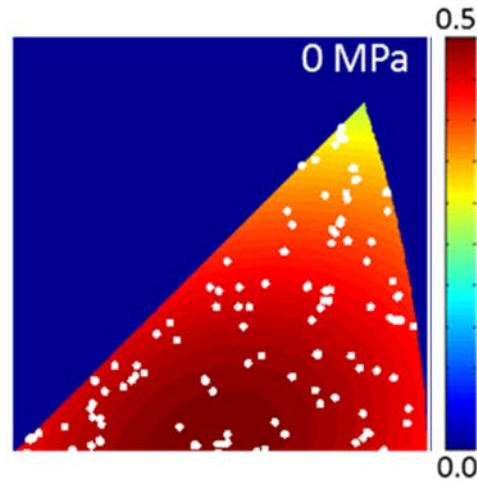


Figure 7.8: Austenite grain orientation determined from two perpendicular $\{200\}$ Friedel pairs at 0 MPa represented in an inverse pole figure together with the estimated Schmid factor.

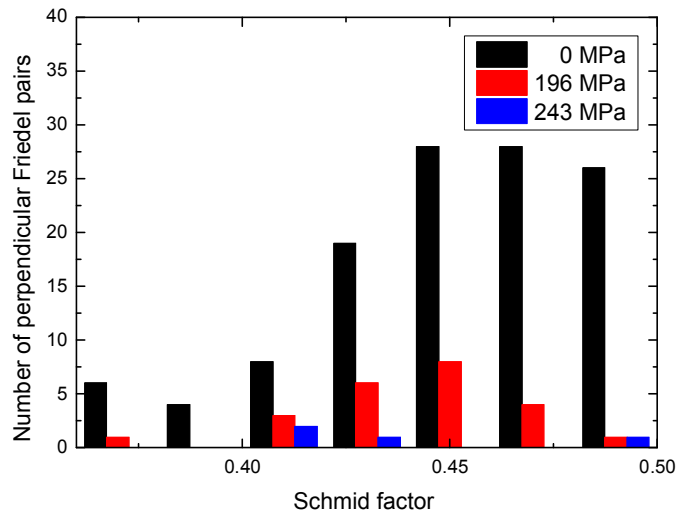


Figure 7.9: Distribution of Schmid factors for individual grains at a tensile stress of 0, 196, and 243 MPa.

7.3.4 High-precision transformation behaviour of individual grains

In this substudy, we follow the transformation behaviour of a limited number of grains for which about 20 reflections could be found leading to a very high precision in their determined orientation and location in the sample volume. Fig. 7.10 presents individual grain positions within the sample prior to straining for the 3 analysis methods (1, 2 and multiple Friedel pairs). The 13 grains identified with the multiple Friedel pairs were tracked as a function of the applied stress and were characterized in terms of carbon content, Schmid factor and grain volume. The overall carbon concentration is found to be around 0.8 wt.% with an average volume of about $20 \mu\text{m}^3$. Figure 7.11 shows the orientation of the 13

grains at different stress levels. The figure clearly shows that the grain retain their orientation. The grains do not significantly rotate, yet disappear due to the martensitic transformation at specific stress values.

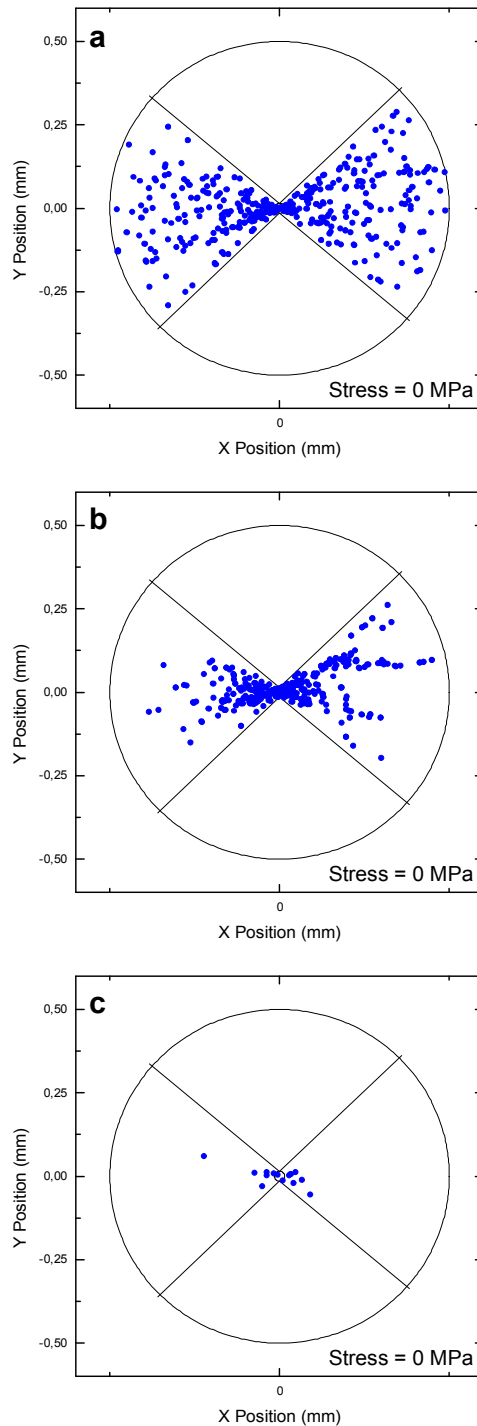


Figure 7.10: Grain position within the sample at no deformation for the 3 analysis method, (a) single Friedel pairs, (b) two perpendicular $\{200\}$ Friedel pairs and (c) Fable method. In successive order the methods require a high number of peaks and are therefore located close to the center.

The order of disappearance is in mostly accordance with their Schmid factor with the exception of grains 4 and 5, which transformed prematurely. These two grains however have a volume that is about twice as large as the average grain volume which significantly reduces the stability of these grains. Fig. 7.12 shows the grain volume evolution as a function of the macroscopic stress for individual grains. In line with our previous work on the thermal stability of austenite grains [29-31], different transformation behaviours have been observed: one-step and two-step transformations.

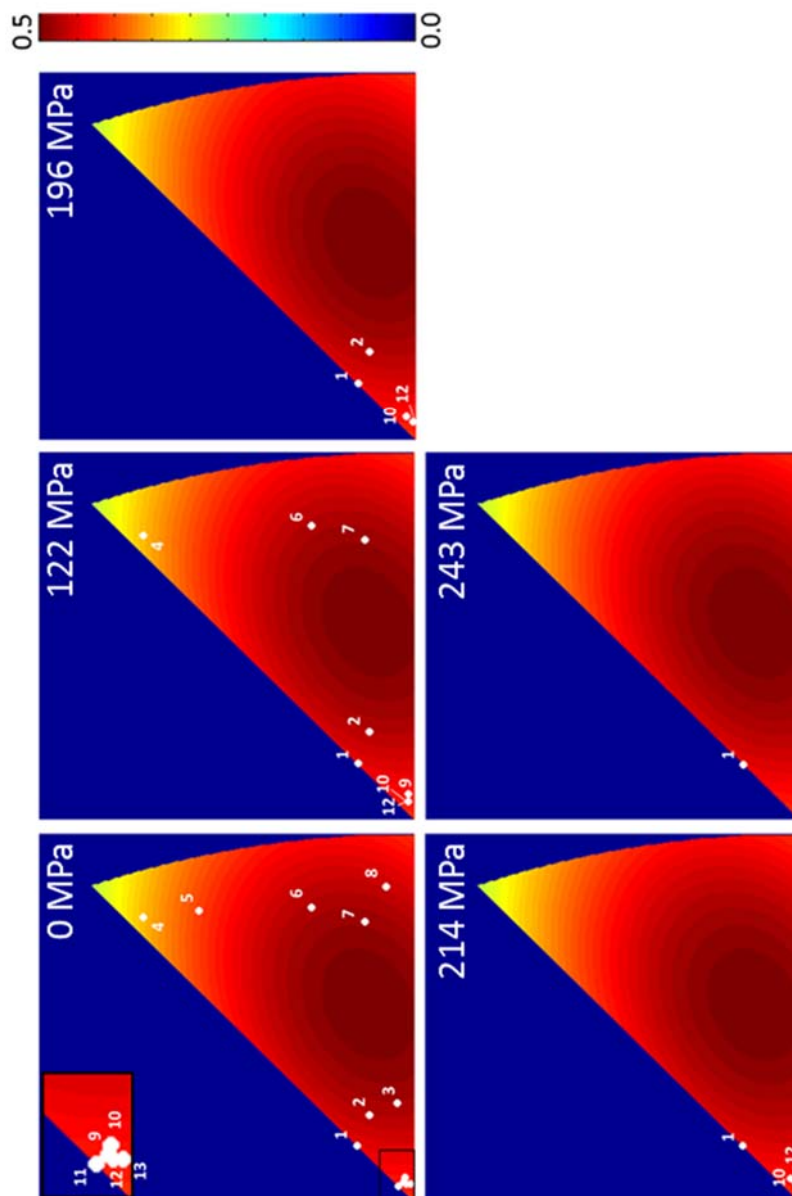


Figure 7.11: Grain orientation for a selection of 13 grains tracked as a function of the macroscopic stress and represented into an inverse pole figure together with the estimated Schmid factor.

In this study, most of the individual transformation sequences indicate that the transformation occurs in one step. Only one grain showed a transformation in two steps where the carbon content remains unchanged during the transformation. A two step transformation may be caused by the presence of two austenite grains that originates from the same high temperature grain, but were separated by the bainitic transformation.

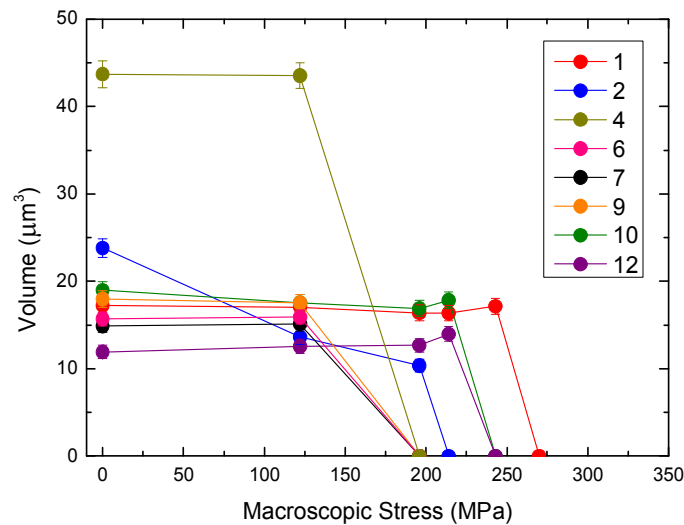


Figure 7.12: Transformation behaviour of the individual austenite grains. Most grains transform completely into martensite in a single strain step. One grain (2) shows a two-step transformation into martensite.

7.4 Conclusions

We have performed in-situ high-energy X-ray diffraction experiments at a synchrotron source in order to study the stability of individual austenite grains in a low-alloyed TRIP steels during tensile loading and developed a new method to locate and follow individual grains based on Friedel diffraction pairs. The main conclusions are:

1. The mechanical stability depends simultaneously on the carbon content, grain orientation and grain volume.
2. The “blocky type” austenite grains present the least mechanical stability because of the predominant volume and local stress critical parameter.

3. The orientation dependence of the martensitic transformation is defined by the Schmid factor. The grains with the highest Schmid factor are the least stable.

4. Transformations have been observed for single austenite grains to take place in either 1 or 2 steps.

7.5 References

- [1] O. Matsumura, Y. Sakuma, H. Takechi, *Trans. ISIJ* 27 (1987) 570.
- [2] O. Matsumura, Y. Sakuma, H. Takechi, *Scripta. Mater.* 21 (1987) 1301.
- [3] Y. Sakuma, O. Matsumura, H. Takeshi, *Metall. Trans. A* 22 (1991)489.
- [4] K. I. Sugimoto, N. Usui, M. Kobayashi, S. Hashimoto, *ISIJ Int* 32 (1992)1311.
- [5] B. C. De Cooman, *Curr. Opin. Solid State Mater. Sci.* 8 (2004) 285.
- [6] S. Oliver, T. B. Jones, G. Fourlaris, *Mat. Sci. Tech.* 23 (2007), 55.
- [7] O. Kwon, K. Lee, G. Kim, K.G. Chin. *Mat. Sci. Forum* 638-642 (2010) 136.
- [8] S. Zaefferer, J. Olhert, W. Bleck. *Acta Mater.* 52 (2004) 2765.
- [9] D.D. Tjahjanto, S. Turteltaub, A.S.J. Suiker, S. van der Zwaag, *Phil. Mag.* 88 (2008) 3369.
- [10] P.J. Jacques, Q. Furnémont, F. Lani, T. Pardoën, F. Delannay. *Acta Mater.* 55 (2007) 3681.
- [11] W.J. Dan, W.G. Zhang, S.H. Li, Z.Q. Lin. *Comp. Mat. Sci.* 40 (2007) 101.
- [12] A.K. Srivastava, G. Jha, N. Gope, S.B. Singh. *Mat. Charact.* 57 (2006) 127.
- [13] L. Skálová, R. Divišová, J. Jandová. *Mat. Proc. Tech.* 175 (2006) 387.
- [14] A. Kammouni, W. Saikaly, M. Dumont, C. Marteau, X. Bano, A. Charai. *Mat. Sci. Eng. A* 518 (2009) 89.
- [15] J. Chiang, B. Lawrence, J.D. Boyd, A.K. Pilkey. *Mat. Sci. Eng. A* 528 (2011) 4516.
- [16] L. Zhao, N.H. van Dijk, E. Brück, J. Sietsma, S. van der Zwaag, *Mat. Sci. Eng. A.* 313 (2001) 145.
- [17] R. Blondé, E. Jimenez-Melero, N.H. van Dijk, E. Brück, L. Zhao, J. Sietsma, S. van der Zwaag. *Solid State Phenom.* 196 (2011) 172.
- [18] N.H. van Dijk, A.M. Butt, L. Zhao, J. Sietsma, S.E. Offerman, J.P. Wright, S. van der Zwaag, *Acta Mater.* 53 (2005) 5439.
- [19] S. Kruijver, L. Zhao, J. Sietsma, E. Offerman, N. van Dijk, L. Margulies, E. Lauridsen, S. Grigull, H. Poulsen, S.van Der Zwaag, *Steel Res.* 73 (2002) 236.
- [20] K. K. Park, S.T. Oh, D.I. Kim, J.H. Han, H.N. Han, S.H. Park, et al. *Mat. Sci. Forum.* 408-412 (2002), 571.
- [21] O. Muránsky, P. Šittner, J. Zrník, E.C. Oliver, *Metall. Mater. Trans. A* 39A (2008) 3097.
- [22] N. Jia, Z.H. Cong, X. Sun, S. Cheng, Z.H. Nie, Y. Ren, et al. *Acta Mater.* 57 (2009) 3965.
- [23] J. Jung, H. Kim, B.C. De Cooman, *ISIJ Int* 50 (2010) 620.
- [24] Y. Tomota, H. Tokuda, Y. Adachi, M. Wakita, N. Minakawa, A. Moriai, Y. Morii, *Acta Mater.* 52 (2004) 5737.

- [25] K. Asoo, Y. Tomota, S. Harjo, Y. Okitsu. *ISIJ Int.* 51 (2011) 145.
- [26] Z.H. Cong, N. Jia, X. Sun, Y. Ren, J. Almer, Y.D. Wang, *Metall. Trans. A*, 40A (2009) 1383.
- [27] E. Jimenez-Melero, N.H. van Dijk, L. Zhao, J. Sietsma, J.P. Wright, S. van der Zwaag. *Mat. Sci. Eng. A*. 528 (2011) 6407.
- [28] R. Blondé, E. Jimenez-Melero, L. Zhao, J.P. Wright, E. Brück, S. van der Zwaag, N.H. van Dijk, *Acta Mater.* 60 (2012) 565.
- [29] E. Jimenez-Melero, N.H. van Dijk, L. Zhao, J. Sietsma, S.E. Offerman, J.P. Wright, S. van der Zwaag. *Acta Mater.* 55 (2007) 6713.
- [30] E. Jimenez-Melero, N.H. van Dijk, L. Zhao, J. Sietsma, S.E. Offerman, J.P. Wright, S. van der Zwaag. *Scripta Mater.* 56 (2007) 421.
- [31] E. Jimenez-Melero, N. H. van Dijk, L. Zhao, J. Sietsma, S.E. Offerman, J.P. Wright, S. van der Zwaag, *Acta Mater.* 57 (2009) 533.
- [32] F. Lani, Q. Furnémont, T. Van Rompaey, F. Delannay, P.J. Jacques, T. Pardoen, *Acta Mater.* 55 (2007) 3695.
- [33] K.S. Choi, W.N. Liu, M.A. Khaleel, Y. Ren, Y.D. Wang. *Metall. Mater. Trans. A*. 39A (2008) 3089.
- [34] D.D. Tjahjanto, S. Turteltaub, A.S.J. Suiker, S. van der Zwaag, *Phil. Mag.* 88 (2008) 3369.
- [35] K.S. Choi, W.N. Liu, X. Sun, M.A. Khaleel, *Acta Mater.* 57 (2009), 2592.
- [36] M. Moscicki, P. Kenesei, J.P. Wright, H. Pinto, T. Lippmann, A. Borbély, A. R. Pyzalla, *Mat Sci Eng A*. 64 (2009) 524.
- [37] W. Ludwig, P. Reischig, A. King, M. Herbig, E. M. Lauridsen, T.J. Marrow, J.Y. Buffière, *Rev. Sci. Instr.* 80 (2009) 033905.
- [38] J. C. Labiche, O. Mathon, S. Pascarelli, M. A. Newton, G. G. Ferre, C. Curfs, *Rev. Sci. Instr.* 78 (2007) 091301.
- [39] E. Jimenez-Melero, N. H. van Dijk, L. Zhao, J. Sietsma, S. van der Zwaag. *Adv. X-ray Analysis*, 1097-0002 (2008) 69.
- [40] H.R. Piehler, *ASM Handbook, Fundamentals of Modeling for Metals Processing*, 22A (2009) 232.
- [41] D.A. Porter, K.E. Easterling, *Phase Transformations in Metals and Alloys*, Chapman & Hall, London, 1992.



Chapter 8

High resolution XRD investigation of individual austenite grains

The martensitic transformation behaviour of the meta-stable austenite phase in low-alloyed TRIP steels has been studied in-situ using high-energy X-ray diffraction during deformation. The austenite stability during tensile deformation has been evaluated at different length scales. A powder diffraction analysis has been performed to correlate the macroscopic behaviour of the material to the observed changes in the volume phase fraction. Moreover, the austenite deformation response has been studied at the length scale of individual grains, where an in-depth characterization of four selected grains has been performed including grain volume, local carbon concentration and grain orientation. For the first time, a high resolution far-field detector was used to study the initial and evolving structure of individual austenite grains during uniaxial tensile deformation. It was found that the austenite sub-grain size does not change significantly during tensile deformation. Most austenite grains show a complete martensitic transformation in a single loading step.

8.1 Introduction

In-situ high-energy synchrotron X-ray diffraction (XRD) is a powerful tool to study the fundamentals of phase transformations. The intense beam of high energy X-rays makes it possible to monitor the change in phase fraction and lattice parameters of the constituent phases in the bulk of a material [1]. Using this unique capability it is possible to analyze the transformation behaviour of metastable austenite in low-alloyed multiphase steels [2,3]. By selecting an optimal beam size the austenite phase can be characterised as a powder average and at the level of individual austenite grains.

The transformation of metastable austenite into martensite during deformation makes it possible to achieve greater elongations and lends these steels their excellent combination of strength and ductility. This mechanism is known as the Transformation-Induced Plasticity (TRIP) effect. This phenomenon increases the work-hardening rate during plastic deformation and hence delays necking [4,5]. This has opened the door to obtain outstanding combinations of strength and ductility. At room temperature, a typical low-alloyed TRIP steel microstructure contains three phases: ferrite, bainite and metastable austenite [6,7]. In our previous synchrotron X-ray diffraction studies we have monitored the transformation behaviour of metastable austenite in low-alloyed TRIP steels during tensile deformation at room temperature [11] and during cooling to a temperature of 100 K [3,9-11]. We found that the austenite stability depends on the local carbon content, the grain size and orientation.

In this study, a detailed characterization of four individual austenite grains has been performed from a high-resolution X-ray diffraction experiment using a far-field detector. In order to evaluate their mechanical stability during tensile deformation, first the average behaviour of the austenite fraction has been analyzed using a medium-field powder diffraction approach (the term near-field is reserved for cases where the detector is placed as close as possible behind the sample). Medium-field measurements covering a wide angular rotation range probing a lower angular resolution have been performed. These data have been analysed using the 3DXRD method [12-16] in order to characterise the transformation behaviour of the four retained austenite grains in terms of grain size, local carbon content and grain orientation.

For TRIP steels it is an open question whether plastic deformation (i.e. the creation of dislocations or dislocation networks) precedes the martensite transformation or that the martensite forms from plastically undeformed austenite grains. So far, no experimental single-grain data are available to resolve this question. To monitor the material at smaller length scales, an additional high-resolution far-field detector was used. For the first time, the sub-grain structure of austenite prior to the transformation has been observed. The use of high-resolution diffraction to monitor subgrains under tensile load was previously explored by Jakobsen and co-workers [17-18] in pure metals. This method is

non-destructive, in contrast to the conventional methods to study the subgrain structure within a single grain like EBSD [19,20] and TEM [21,22]. The interplay between tensile deformation, the orientation-dependent austenite-to-martensite transformation, grain volume and carbon concentration has been analysed by diffraction data from the medium-field detector, while the substructure evolution of individual grain as a function of the macroscopic stress has been investigated by the diffraction data from the far-field detector. The analysis from the combination of both data from medium-field and far-field detectors provided a detailed characterization of the austenite stability. While the angular resolution obtained with the far-field detector is very high, the spatial resolution is limited (either to the beam size or to a smaller value defined by reconstruction of the reflections on the medium-field detector).

8.2 Experimental details

8.2.1 Sample preparation

The chemical composition of the studied TRIP steel is shown in Table 8.1. A cylindrical dog-bone tensile specimen with a gauge length of 10 mm and a diameter of 1 mm was machined from hot rolled sheet material. The cylindrical axis of the samples was chosen parallel to the rolling direction (RD). A mark parallel to the normal direction of the sheet material was made on the top part of the cylindrical sample in order to keep track of the normal (ND) and transverse (TD) sample orientation. First, the sample was annealed in a salt bath for 30 min at an intercritical temperature of 1143 K in order to obtain equal fractions of austenite and ferrite. Then the samples was quenched in a second salt bath to a temperature of 673 K and held for 2 min. During this holding time part of the intercritical austenite transformed into bainite and the remaining austenite was enriched in carbon. The carbon-enriched austenite remained in a metastable state after a final water quench to room temperature. This heat treatment, discussed in more detail in a previous study [23], yielded a multiphase microstructure composed of ferrite (α), bainite (α_b) and metastable austenite (γ), as shown in the optical micrograph of Fig. 8.1. The austenite phase is present in two forms: blocky type and film type. The blocky type (with a size $> 1 \mu\text{m}$) corresponds to the metastable retained austenite, while the film type (with a size $< 1 \mu\text{m}$) corresponds to the stable austenite present within the bainite. The stability of these blocky type

austenite grains defines the TRIP effect as the film-type austenite remains stable during tensile deformation. The austenite grain size distribution was investigated previously [9].

Table 8.1: *Chemical composition of the studied samples in wt.% with balance Fe.*

C	Mn	Si	Al	P
0.218	1.539	0.267	1.75	0.018

8.2.2 Experimental setup

The in-situ high-energy XRD experiments were performed with the 3D X-ray diffraction microscope at the ID11 beam line of the European Synchrotron Radiation Facility (Grenoble, France). Fig. 8.2 shows the experimental setup used for the experiments. The monochromatic X-ray beam with energy of 69.52 keV (wavelength of 0.1783 Å) made it possible to obtain diffraction patterns from the bulk material in transmission geometry. A square beam size defined by slits with a dimension of 50×50 μm² was chosen in order to illuminate a small amount of grains within the cylindrical bar-shaped sample. For this experiment, a two dimensional CCD detector (FRELON) [24] and a prototype HIZPAD 1 mm CdTe pixel detector with 256×256 pixels covering an area of 14×14 mm² [25] were placed behind the sample at 251.619 mm and 3239.136 mm, respectively.

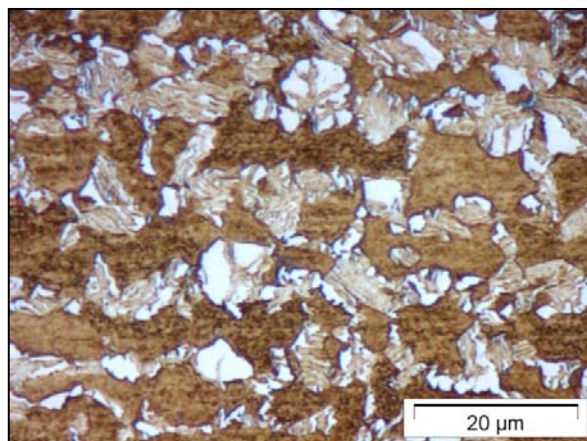


Figure 8.1: *Optical micrograph of the low-alloyed TRIP steel. The room temperature multiphase microstructure contains a metastable austenite phase (white) within a matrix of ferrite (dark brown) and bainite (light brown) phases.*

8.2.3 Experimental procedure

To study the mechanical stability of retained austenite, the sample was mounted on a 2 kN micro tensile tester placed on a Huber diffractometer that allowed ω -rotations around the cylindrical axis of the sample. For each deformation step the strain was held constant during a complete set of X-ray diffraction measurements, where the diffracted beam was recorded consecutively on both detectors.

After each deformation step the sample alignment was checked using the reflection of an untransforming ferrite grain within the illuminated sample volume. For the medium-field (MF) detector data, the sample was continuously rotated during exposure around the cylindrical axis of the sample (perpendicular to the X-ray beam) in steps of 0.2° covering an angular range of 90° . For the far-field (FF) detector data, the $\{111\}_\gamma$ reflection of austenite (face-centred cubic structure) and the $\{110\}_\alpha$ reflection of ferrite (body-centred cubic structure) have been monitored simultaneously in the horizontal scattering plane.

During the experiments, 4 individual austenite peaks on the $\{111\}_\gamma$ ring have been selected from the medium-field X-ray diffraction data. These grains were selected by first creating a 2D map of the $\{111\}$ ring intensity collected using a vertical translation of the far-field detector covering an angular range of about 1 degree combined with a sample rotation of 6 degrees. From this 2D map of the $\{111\}$ ring intensity the 4 most intense austenite reflections located in the central part of the 2D map were selected. The selected peaks have been monitored at high resolution using the same method as the medium-field detector but using smaller rotation steps of 0.002° and covering an angle range between 0.8° and 2.8° , depending on the peak studied. The long sample-to-detector distance for the FF detector allowed us to separate the $\{111\}_\gamma$ and $\{110\}_\alpha$ reflections, which are overlapping on the MF detector.

Assuming an average austenite grain radius of about $3 \mu\text{m}$ and a transforming blocky-type austenite phase fraction of $f \approx 3\%$ (these are the largest grains) the expected number of austenite grains within the illuminated sample volume of $50 \times 50 \times 1000 \mu\text{m}^3$ is $N \approx 700$. These grains will produce $2 \times m_{\text{hkl}} \times N \approx 8400$ reflections on the $\{111\}$ austenite ring.

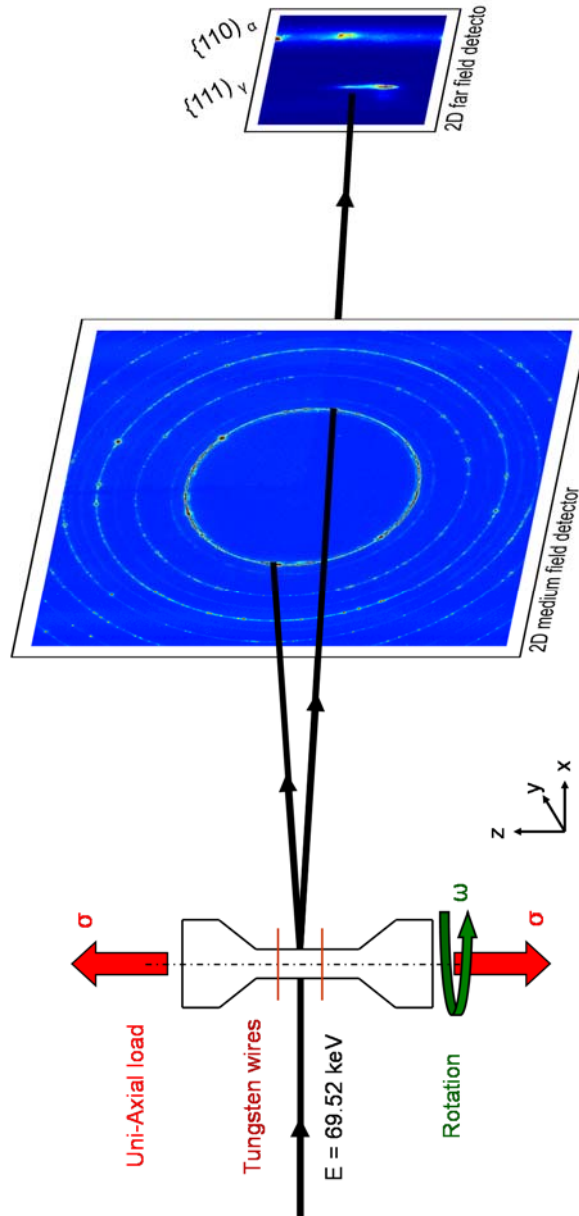


Figure 8.2: Schematic representation of the experimental setup used for the high-energy microbeam X-ray diffraction experiments in transmission geometry. Two separate 2D detectors were used: a medium-field CCD detector (MF) and a far-field CdTe pixel detector (FF). The sample was under a tensile stress (σ) and continuously rotated around the vertical axis during exposure.

The average solid angle per reflection $\Delta\Omega \approx 4\pi/8400$, results in an angular spacing between the (111) austenite reflections of $(180/\pi) \times (\Delta\Omega)^{1/2} \approx 2$ degrees. This average angular spacing is sufficient to obtain well distinguishable individual peaks. The corresponding number of grains that are placed in the central volume that remains illuminated for all sample rotations ($10^5 \mu\text{m}^3$) is about 30.

Fig. 8.3a displays a 2D diffraction pattern of TRIP steel from the MF detector. From this diffraction pattern, the $\{111\}_\gamma$, $\{200\}_\gamma$, $\{220\}_\gamma$ and $\{311\}_\gamma$ austenite reflections have been studied. Each austenite diffraction ring consists of a number of single spots originating from individual austenite grains in the TRIP microstructure, together with a powder signal stemming from austenite grains, whose volume falls below the experimental detection limit of about $5 \mu\text{m}^3$ for individual grains [3]. Fig. 8.3b shows a high magnification of the region of interest on the MF detector (resolution is around 0.007 \AA^{-1}) and Fig. 8.3c is the corresponding XRD pattern for the same grain monitored on the FF detector. The longer sample-to-detector distance provides a higher resolution of 0.0006 \AA^{-1} . The image obtained from the FF detector permits us to evaluate the subgrain structure within an individual austenite grain. The instrumental parameters of the 3D X-ray diffraction microscope for both detectors were determined using a CeO_2 calibrant.

Fig. 8.4 shows the one-dimensional XRD patterns of CeO_2 , resulting from an integration over the azimuthal angles at constant scattering angle of the two-dimensional XRD image measured on the MF and FF detectors. The 2θ values measured on the MF detector ranges up to 10.7° while a single image on the CdTe detector covers only 0.25° . The far field detector has been translated horizontally to monitor a range from 5.248° to 8.913° in order to cover 6 CeO_2 reflections. The FWHM of the $\{311\}$ reflection determined from a Pseudo-Voigt profile fitting decrease from $0.0382(2)^\circ$ to $0.004903(3)^\circ$ for an increasing detector sample-to-distance, corresponding to a decrease in resolution from $6.10(3)\times 10^{-3}$ to $7.845(5)\times 10^{-4}$. Changes in the sample-to-detector distance during straining were determined using a CeO_2 calibrant placed on the sample.

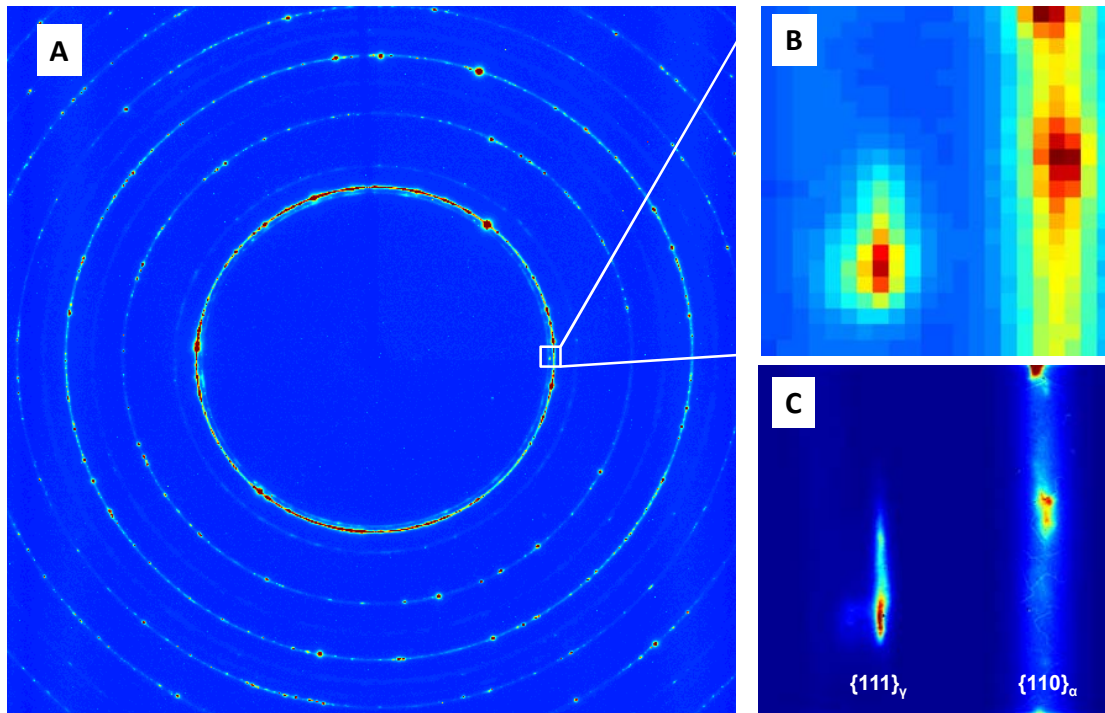


Figure 8.3: Two-dimensional X-ray diffraction pattern of the TRIP sample. The pattern monitored on the medium-field (MF) detector (a) shows both ferrite and austenite reflections on separate diffraction rings. (b) A zoom of the medium-field data that shows a single austenite diffraction peak from the $\{111\}$ ring and part of the ring $\{110\}$ of ferrite. (c) The corresponding image monitored on the far field (FF) detector provides a higher resolution.

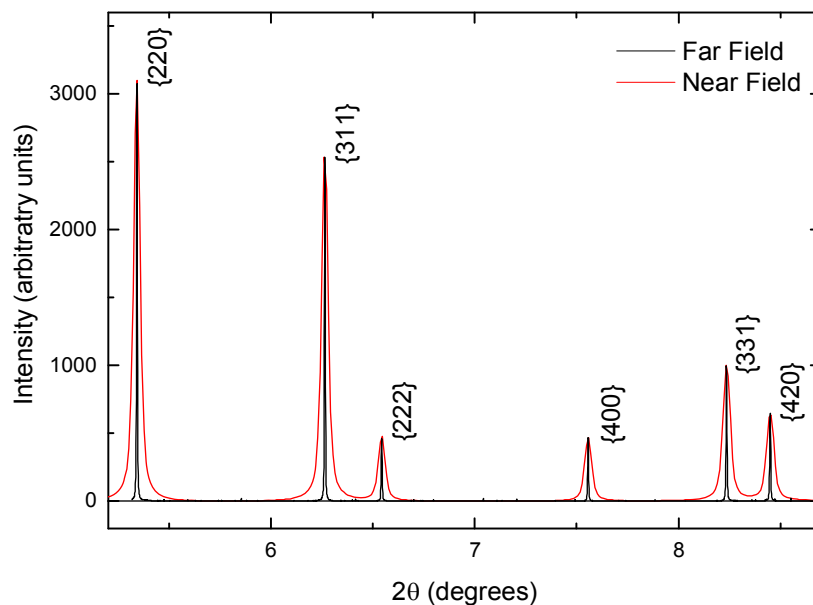


Figure 8.4: One-dimensional X-ray diffraction pattern of the CeO_2 calibrant measured with both detectors.

8.3 Data analysis

8.3.1 Powder data analysis

The wide ω angle range monitored on the MF detector was used to perform an accurate powder XRD data analysis. The measured data consisted of a series of two-dimensional diffraction patterns as a function of sample elongation and ω -angle. The two-dimensional diffraction patterns for the complete ω range covered in this experiment were summed. Afterwards, an integration over the azimuthal angles at constant scattering angle was performed using the FIT2D software package [26] to obtain the corresponding one-dimensional diffraction patterns at different strain steps. A Rietveld refinement of the resulting one-dimensional X-ray diffraction patterns was performed using the Fullprof package [27] in order to determine the phase fraction and lattice parameter of the constituent phases as a function of the macroscopic strain.

8.3.2 Data analysis of single grains on the near-field detector

The volume, crystallographic orientation, centre-of-mass position and strain state of the 4 monitored individual grains have been determined. For the data analysis the algorithms recently developed by Sharma and co-workers were applied [28,29]. The first step consisted of a peak search of the austenite peaks where the detection threshold has been scaled with the structure factor of the studied $\{hkl\}$ plane because of their relatively weak intensity. The next step consisted of the assignment of diffraction spots to individual grains and refining them to obtain accurate values. The volume of a grain was obtained from the integrated intensities of the corresponding diffraction spots. Full grain illumination was checked by evaluation of the grain position from the reflections on the medium-field detector.

8.3.3 Data analysis of single grains on the far-field detector

The grain volume V_g of the 4 monitored diffraction peaks has been determined from integrated intensity I_g of the single grain reflection on the FF detector by a scaling to the powder intensity of the corresponding diffraction ring I_p on the MF detector:

$$V_g = \frac{1}{2} m \Delta \omega \cos(\theta) f^\gamma V_{gauge} \frac{I_g}{I_p} \quad (1)$$

where m_{hkl} is the multiplicity factor of the $\{111\}_\gamma$ ring of austenite, $\Delta\omega$ is the angular range over which the grain is rotated, f^γ is the volume fraction of the austenite phase determined from the powder data analysis from the MF data and V_{gauge} is the gauge volume, which is defined by the beam size and the thickness of the sample.

8.4 Results and discussion

8.4.1 Macroscopic mechanical behaviour

Fig. 8.5a shows the macroscopic (engineering) stress-strain curve of the low-alloyed TRIP steel. Two tungsten wires glued on the surface of the sample perpendicular to the loading direction acted as an accurate strain gauge during deformation. Each data point on the curves represents a set of X-ray diffraction measurements, while the macroscopic strain is held constant. We recorded the diffraction patterns for a series of elongation steps up to the yield strength. The stress-strain data provided a yield strength of 425 MPa and an ultimate tensile strength of 624 MPa at strain levels of 0.83% and 5.95%, respectively. These values are in good agreement with values obtained on macroscopic samples.

8.4.2 Austenite phase fraction evolution

A powder analysis of the XRD data indicated a austenite volume fraction of 8.5(3) % at room temperature. By increasing the macroscopic strain, the mechanically induced transformation starts well before the macroscopic yield stress is reached. The fraction decreases continuously to 5.6(2)% for strains up to 0.8% and then remains roughly constant until the maximum applied strain (see Fig. 8.5b).

Table 8.2: Grain characteristics for the 4 grains studied on the medium-field detector before deformation.

Grain	Lattice Parameter (Å)	Carbon concentration (wt.%)
1	3.6015(1)	0.757(2)
2	3.6039(1)	0.809(2)
3	3.6031(1)	0.791(2)
4	3.6120(1)	0.987(2)

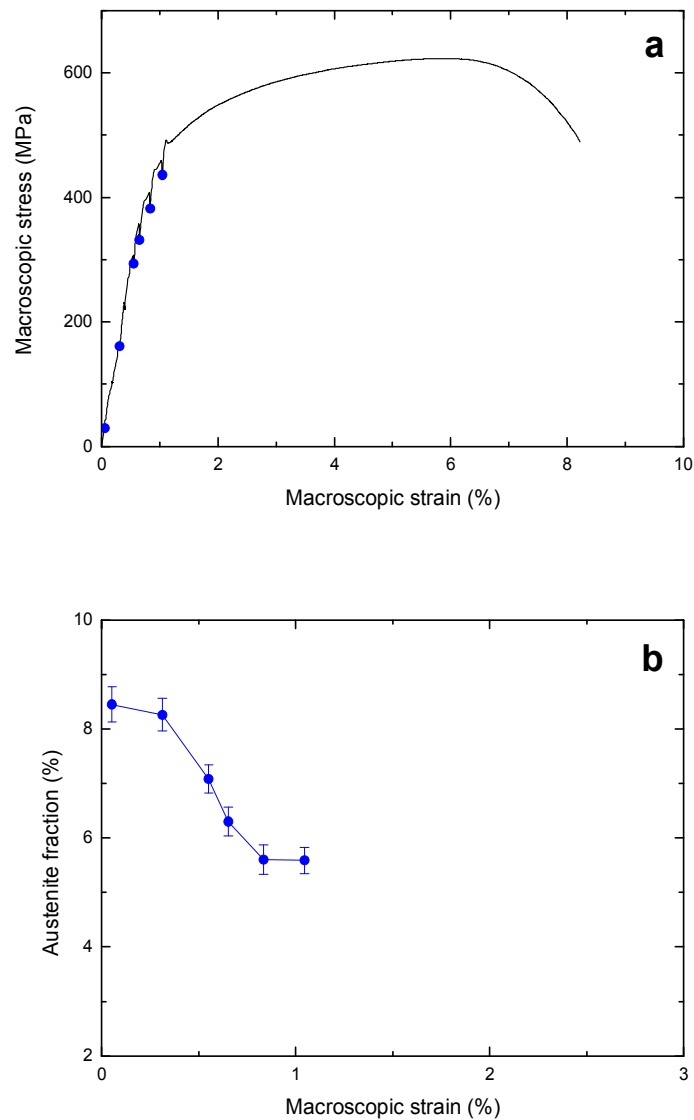


Figure 8.5: (a) Macroscopic (engineering) stress-strain curves of TRIP steel measured step-wise during the in situ X-ray diffraction experiments and (b) the austenite fraction as a function of the macroscopic strain.

8.4.3 Single grain analysis

The 4 reflections monitored on the FF detector have been tracked back to the MF diffraction data. For the 4 individual grains of interest a collection of austenite peaks on different diffraction rings was identified and indexed to obtain the grain orientation. At zero deformation the grain volume, the lattice parameter and derived carbon concentration of the 4 indexed grains have been reported in Table 8.2.

The relationship between the austenite lattice parameter and the grain's chemical composition is given by [11,30]:

$$a_{\gamma} = 3.556 + 0.0453x_c + 0.00095x_{Mn} + 0.0056x_{Al} \quad (2)$$

where a_{γ} is the austenite lattice parameter in Å and x_c , x_{Mn} and x_{Al} are the alloying concentrations in wt.%. The presence of Si and P is considered to have a negligible effect on the lattice parameter of austenite. The studied grains are blocky-type austenite grains, which constitute the remaining parts of the intercritical austenite grains after the partial bainitic transformation. Both the carbon enrichment and the grain volume are significant parameters to retain the austenite stability at room temperature.

These microstructural parameters have been intensively investigated to establish their relation to the martensitic start temperature of the austenite-to-martensite transformation [3,9-11]:

$$M_s = M_{so} - Ax_c - BV_{\gamma}^{-\frac{1}{3}} \quad (3)$$

The first two terms of this expression reflect the well-known Andrews' empirical relation between the martensitic start temperature, M_s and the carbon content with $A = 425$ K/wt.% [31], while the third term was recently introduced to quantify the effect of the grain volume on its stability, where $M_{so} = 702$ K and $B = 475$ μm K for the current TRIP microstructure [3].

The derived grain orientation has been used to map the tensile direction in the inverse pole figure represented by the stereographic triangle in Fig. 8.6. The background colour in the inverse pole figure corresponds to the theoretical Schmid factor for a face-centred cubic system. The Schmid factor represents the relative strength of the maximum resolved shear stress along the relevant slip system

that drives the austenite-to-martensite transformation. The 4 selected grains present a Schmid factor of about 0.45, which is close to the highest theoretical value of 0.5.

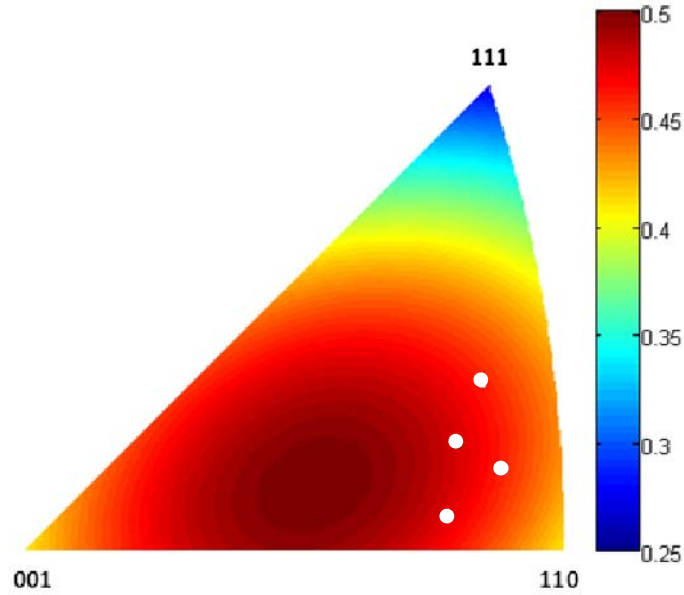


Figure 8.6: Stereographic triangle representing the grain orientation with respect to the loading direction at no deformation. The white spheres indicate the relative orientation of the 4 grains studied. The colour scheme represents the theoretical Schmid factor for the most favourable slip system in a face-centred cubic system.

8.4.4 High resolution data analysis

The integrated radial peak profile has been fitted with a Pseudo-Voigt function where the resulting parameters of the 4 austenite grains have been reported in Table 8.3.

Table 8.3: Grain characteristics for the 4 grains studied on the far field detector before deformation.

Q_0 (\AA^{-1})	$\langle q_{\parallel}^2 \rangle^{\frac{1}{2}}$ (10^{-3}\AA^{-1})	$\langle q_{\perp}^2 \rangle^{\frac{1}{2}}$ (10^{-3}\AA^{-1})	$\langle \Delta 2\theta \rangle$ (deg)	$\langle \Delta \alpha \rangle$ (deg)	$\langle \varepsilon^2 \rangle^{\frac{1}{2}}$ (%)	Volume (μm^3)	Radius (μm)	Subgrains (number)
3.0248	0.7056	12.463	0.0011	0.0035	0.023	1426	6.98	1066
3.0248	0.9096	6.175	0.0015	0.0011	0.030	369.3	4.45	263
3.0260	3.3801	52.414	0.0055	0.0150	0.112	658.1	5.40	422
3.0243	1.0271	5.679	0.0017	0.0014	0.034	251.1	3.91	82

Fig. 8.7 shows the projection of the 2D intensity distribution on the plane perpendicular (q_x, q_z) to the scattering vector at no deformation. This 2D projection of the 3D diffraction peaks in reciprocal space shows a complex variation in the diffracted intensity originating from a single grain. For grain 1, it is clearly observed that the peak shows one central peak with a rich substructure. In high resolution the pronounced substructure of the reflection is observed even before applying any macroscopic tensile load. Several small sharp peaks, slightly misoriented with respect to the main peak, are observed indicating the presence of subgrains within the grain. The presence of a rich dislocation structure within the austenite grain before applying a tensile deformation may find its origin in the TRIP heat treatment, where a certain amount of dislocations are expected to be induced by the bainite formation and the resulting inhomogeneous residual stresses. Such a pre-existing substructure has been observed for all the 4 grains.

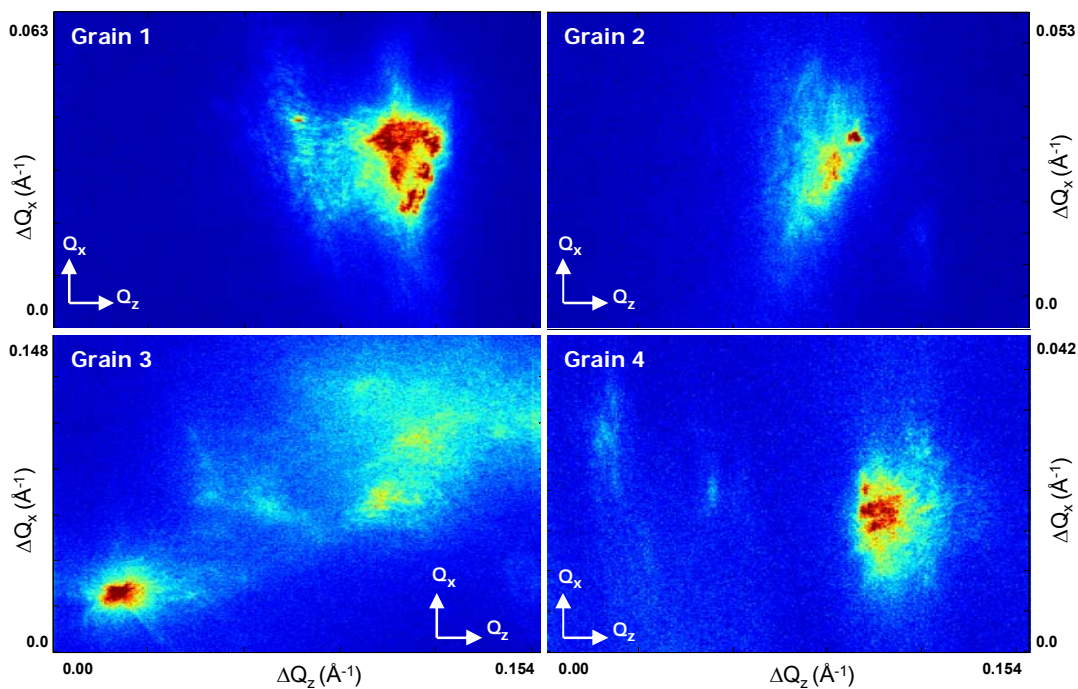


Figure 8.7: Projection of the 3D reciprocal space intensity distribution on to the azimuthal plane (Q_x, Q_z) at no deformation.

For grain grain 3 besides the central peak a disconnected more diffuse contribution is observed. It cannot be excluded that the intensity of the diffuse contribution in Fig. 8.7c originates from a different

grain. However, the $\{111\}$ austenite reflections are generally well separated under the current conditions. An alternative explanation is that during the bainitic transformation in a limited number of cases two spatially separated units origination from the same grain are generated [3]. In this case these retained austenite units can have a slightly different orientation.

To obtain a better insight into the substructure representing the dislocation network, each subpeak with a local maximum in intensity within the 3D peak profile presented in Fig. 8.7 has been studied independently and compared to the centre of mass of the total reflection. The scattering vectors \vec{Q} of each subpeak and \vec{Q}_0 of the full peak have been compared. In Fig. 8.8, the resulting difference vector $\vec{q} = \vec{Q} - \vec{Q}_0 = \vec{q}_{par} + \vec{q}_{perp}$ has been decoupled in \vec{q}_{par} and \vec{q}_{perp} , corresponding respectively to the component along and perpendicular to \vec{Q}_0 .

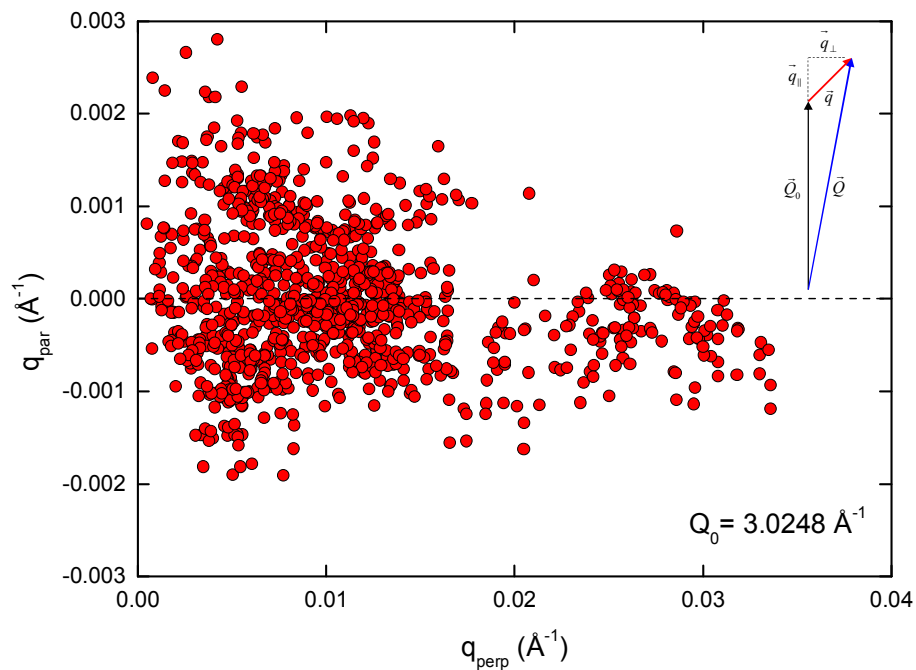


Figure 8.8: Scattering vectors of the subpeaks of grain 1. The scattering vector is $\vec{Q} = \vec{Q}_0 + \vec{q}$ decomposed in the central vector \vec{Q}_0 and the deviatory vector \vec{q} . The vector \vec{q} is decomposed in a component q_{\parallel} along and q_{\perp} perpendicular to \vec{Q}_0 , respectively.

The maximum misorientation for the subpeaks amounts to $\Delta q_{perp} = 0.0336 \text{ \AA}^{-1}$. The variation in lattice parameter, represented by Δq_{par} , is significantly smaller. In Table 8.3 the grain volume and the number of assigned subgrains is listed for the studied grains. When the grain volume is divided by the number of identified subgrains an average volume of about $1 \mu\text{m}^3$ is obtained for all 4 grains. This value should be regarded as an upper bound for the average subgrain size as the smallest subgrains cannot be identified due to the overlap of subgrain diffraction peaks: the weakest peaks are indistinguishable when they fall inside the tails of the more intense peaks from larger subgrains. That the average subgrain size is significantly smaller than $1 \mu\text{m}$ is consistent with typical experimental dislocation densities of the order of 10^{14} m^{-2} [32,33], which corresponds to an average subgrain size of about $0.1 \mu\text{m}$.

The characteristics of the subgrain structure can be quantified in more detail using an autocorrelation function of the 3D high-resolution peak structure represented in Fig. 8.7. The correlation function reflects the nature of the spatial correlations within the material [34-36]. The used reciprocal-space autocorrelation function corresponds to:

$$C(\vec{q}) = \frac{\langle I(\vec{o})I(\vec{q}) \rangle}{\langle I(\vec{o})I(\vec{o}) \rangle} \quad (4)$$

where \vec{q} is the difference vector in reciprocal space and $I(\vec{q})$ is its corresponding intensity. The resulting curves for grain 1 are shown in Fig. 8.9. Two types of contributions are present in the autocorrelation function: one sharp initial decrease in the first displacement step, followed by a smooth continuous decrease. The overall behaviour closely follows an exponential of the following form:

$$C(q_i) = (1 - A) + A \exp(-c |q_i|) \quad (5)$$

where q_i is the component of \vec{q} along (q_{par}) and perpendicular (q_{perp}) to \vec{Q}_0 . This autocorrelation

function reflects a Lorentzian distribution $\frac{1}{\pi} \left\{ \frac{\Gamma/2}{x^2 + (\Gamma/2)^2} \right\}$ for a symmetric real-space displacement x

with a full width at half maximum Γ [37]. The constant c is linked to the distribution with by $c = \pi\Gamma$. In

our case the constant c has been calculated in both dimensions: $c_{perp} = 70.6(2) \text{ \AA}$ and $c_{par} = 33.2(5) \text{ \AA}$.

The corresponding correlation distance for the displacement fields is as low as $\Gamma_{par} \approx 1$ nm. This confirms earlier observations that the subgrains within a single grain form a hierarchical structure with characteristic sizes ranging from the nanometer up to the micron range [33,34].

8.4.5 Strain effect on the sub structure of individual austenite grains

Fig. 8.10 shows a projection of the 3D diffraction peak of grain 4 for both detectors as a function of the stress state. The sequence illustrates the power of high-resolution diffraction to study the evolution in subgrain structure during tensile deformation [38]. It is observed (on both detectors) that the single grain reflection remains essentially unchanged for increasing strain levels well below the macroscopic yield strength until a critical stress is reached and the reflection disappears. The tensile load required for macroscopic yielding to induce plastic deformation is not reached at this stage. The reason the peak intensity disappeared for 382 MPa is that the critical stress level to activate the martensitic transformation has been reached. As shown in Fig. 8.10, the high resolution data indicate that the peak position is only weakly affected by the tensile load. In the macroscopic elastic regime the grains, embedded in the multiphase microstructure, are indeed not expected to show a significant rotation.

Even though this may not be anticipated, it is important to check that the disappearance of the austenite reflection originates from a martensitic transformation and is not caused by a sudden grain rotation (potentially caused by the transformation of a neighbouring austenite grain). This cannot be excluded from the limited angular view probed by the FF detector. Therefore, the MF data were used to index multiple peaks originating from the same grain. Using the 3DXRD method [28,29] the orientation matrix of the 4 individual grains was obtained for each deformation step from the combined set of reflections collected on the MF detector over a wide angular rotation range. The grain orientation of the 4 grains has been tracked for increasing stress. The resulting stereographic projection was found to be equivalent to initial representation shown in Fig. 8.6. No grain rotation has been observed in the macroscopic elastic regime for the 4 grains of interest.

As explained in a previous study on the thermal stability [9], different types of transformation behaviour exist: (i) no transformation, (ii) a complete transformation (in a single cooling step) and (iii) an partial

transformation (in more than one cooling step). Under tensile deformation we find that most grains show a complete martensitic transformation in a single strain step. In Fig. 8.11, the grain volume as a function of the macroscopic strain has been presented. Grains 2 to 4 transformed in one step, while grain 1 shows a partial transformation in the first step. The grain volume reduced significantly in the first strain step and disappeared in the second strain step.

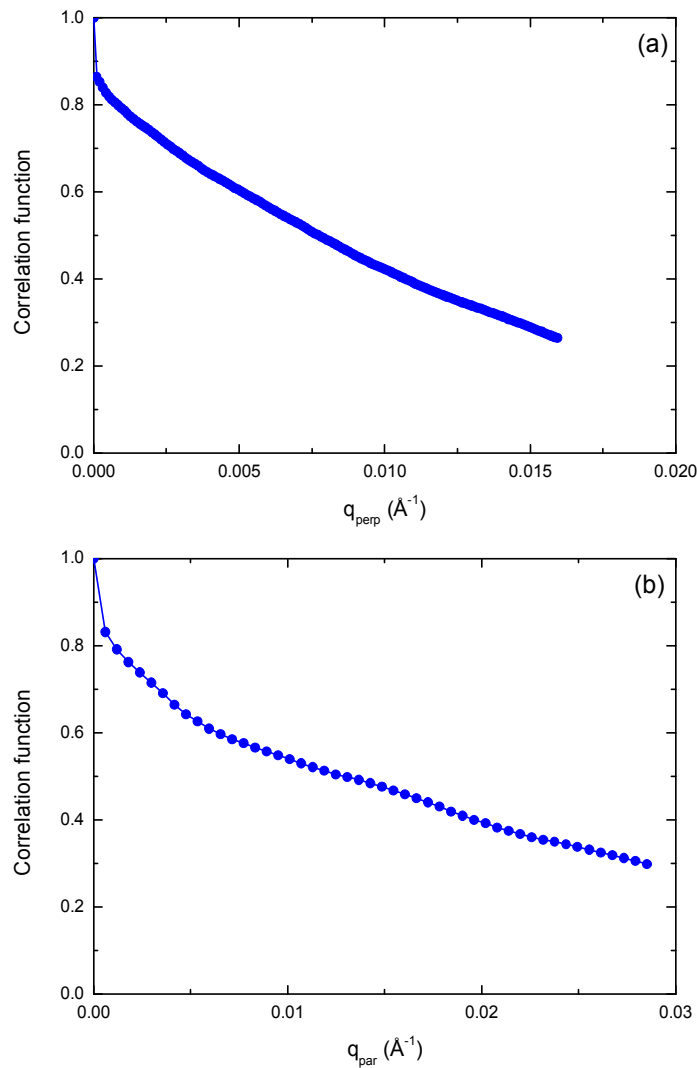


Figure 8.9: Correlation function of the 2D peak of the grain 1 over as a function of (a) q_{perp} and (b) q_{par} .

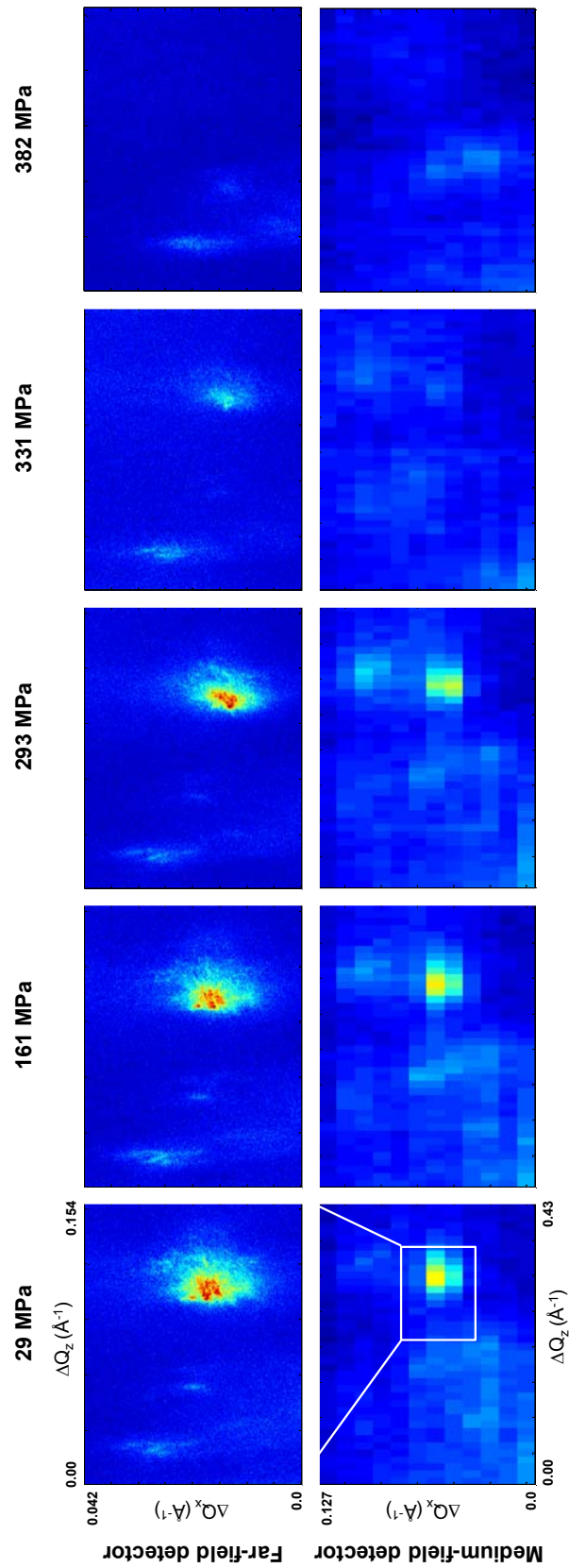


Figure 8.10: Projection of the 3D reciprocal space intensity distribution of the grain 4 on to the azimuthal plane (Q_x, Q_z). A series of projection for both detector and 5 stress states is presented.

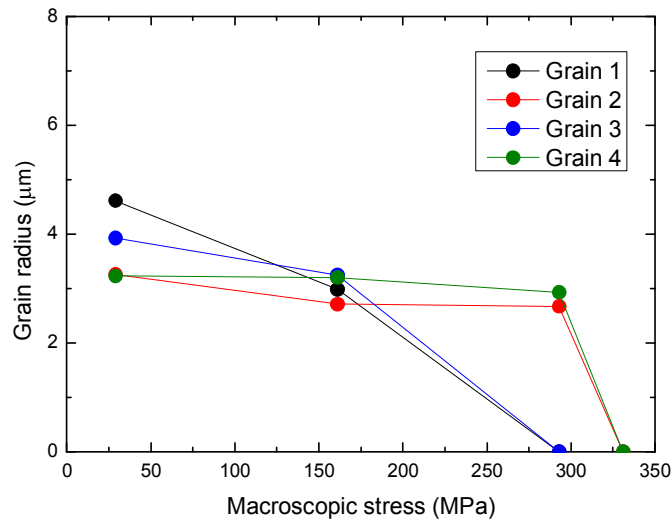


Figure 8.11: Grain volume as a function of the applied macroscopic stress from the medium-field single grain data analysis.

8.5 Conclusions

We have performed in-situ high-resolution X-ray diffraction experiments at a synchrotron source in order to obtain a full characterization of individual metastable austenite grains within a multiphase TRIP microstructure. A multi-method approach focussing on the phase averages (powder data), single grains (micro-beam data) and subgrains (high-resolution data) has been performed. The main conclusions are:

1. the presented method of using a far-field detector allows us to study individual Bragg reflections at high resolution. This makes it possible to resolve subgrains in austenite grains prior to the martensitic transformation.
2. We have observed that the austenite grains already contain a pronounced initial substructure before applying any mechanical load. The corresponding dislocations are expected to be the result of local transformation strains during the TRIP heat treatment.
3. Austenite grains have been tracked during tensile deformation at stress level lower than the macroscopic yield stress. Most austenite grains show a complete martensitic transformation in a single strain step.

4. A full grain characterisation from the medium-field data shows that the grains are not rotating before reaching the required critical resolved shear stress for transformation.

8.6 References

- [1] M. Militzer, *Science* 298 (2002) 975.
- [2] R. Blondé, E. Jimenez-Melero, L. Zhao, J. P. Wright, E. Brück, S. van der Zwaag, N. H. van Dijk, *Acta Mater.* 60 (2012) 565.
- [3] E. Jimenez-Melero, N.H. van Dijk, L. Zhao, J. Sietsma, S.E. Offerman, J.P. Wright, S. van der Zwaag. *Scripta Mater.* 56 (2007) 421.
- [4] W.J. Dan, W.G. Zhang, S.H. Li, Z.Q. Lin. *Comp. Mat. Sci.* 40 (2007) 101.
- [5] P.J. Jacques, Q. Furnémont, F. Lani, T. Pardoën, F. Delannay. *Acta Mater.* 55 (2007) 3681.
- [6] I.B. Timokhina, P.D. Hodgson, E.V. Pereloma. *Metall. Mater. Trans. A* 35A (2004) 2331.
- [7] S. Zaefferer, J. Olhert, W. Bleck, *Acta Mater.* 52 (2004) 2765.
- [8] E. Jimenez-Melero, N.H. van Dijk, L. Zhao, J. Sietsma, J.P. Wright, S. van der Zwaag. *Mat. Sci. Eng. A* 528 (2011) 6407.
- [9] E. Jimenez-Melero, N.H. van Dijk, L. Zhao, J. Sietsma, S.E. Offerman, J.P. Wright, S. van der Zwaag. *Acta Mater.* 55 (2007) 6713.
- [10] E. Jimenez-Melero, N.H. van Dijk, L. Zhao, J. Sietsma, S.E. Offerman, J.P. Wright, S. van der Zwaag. *Acta Mater.* 57 (2009) 533.
- [11] N.H. van Dijk, A.M. Butt, L. Zhao, J. Sietsma, S.E. Offerman, J.P. Wright, S. van der Zwaag. *Acta Mater.* 53 (2005) 5439.
- [12] S. Schmidt, H. F. Poulsen, G. B. M. Vaughan, *J. Appl. Cryst.* 36 (2003) 326.
- [13] J. Oddershede, S. Schmidt, H. F. Poulsen, H. O. Sørensen, J. Wright, W. Reimers, *J. Appl. Cryst.* 43 (2010) 539.
- [14] J. V. Bernier, N. R. Barton, U. Lienert, M. P. Miller, *J. Strain Anal. Eng.* 46 (2011) 527.
- [15] J. K. Edmiston, N. R. Barton, J. V. Bernier, G. C. Johnson, D. J. Steigmann *J. Appl. Cryst.* 44 (2011) 299.
- [16] H.F. Poulsen, *Three-Dimensional X-ray Diffraction Microscopy – Mapping Polycrystals and Their Dynamics* (2004) Heidelberg: Springer.
- [17] B. Jakobsen, H.F. Poulsen, U. Lienert, W. Pantleon, *Science* 312 (2006) 889.
- [18] B. Jakobsen, H.F. Poulsen, U. Lienert, W. Pantleon, *Acta Mater.* 55 (2007) 3421.
- [19] Humphreys, F.J. (2001). *J. Mater. Sci.* 36, 3833-3854.
- [20] J. Jiang, T.B. Britton, A.J. Wilkinson, *Acta Mater.* 61 (2013) 7227.
- [21] J.Y. Huang, Y.T. Zhu, H. Jiang, T.C. Lowe, *Acta Mater.* 49 (2001) 1497.

-
- [22] F. Dalla Torre, R. Lapovok, J. Sandlin, P.F. Thomson, C.H.J. Davies, E.V. Pereloma, *Acta Mater.* 52 (2004) 4819.
- [23] R. Blondé, E. Jimenez-Melero, N.H. van Dijk, E. Brück, L. Zhao, J. Sietsma, S. van der Zwaag, *Solid State Phenom.* 172-174 (2011) 196.
- [24] J. C. Labiche, O. Mathon, S. Pascarelli, M.A. Newton, G.C. Ferre, C. Curfs, G. Vaughan, A. Homs, D.F. Carreiras, *Rev. Sci. Instr.* 78 (2007) 091301.
- [25] M. Ruat, C. Ponchut, *Trans. Nucl. Sci* 59 (2011) 4799.
- [26] A.P. Hammersley, S.O. Svensson, M. Hanfland, A.N. Fitch, D. Hausermann. *High Pressure Res.* 14 (1996) 235.
- [27] J. Rodríguez-Carvajal, *Physica B.* 192 (1993) 55.
- [28] H. Sharma, R. M. Huizenga, S. E. Offerman, *J. Appl. Cryst.* 45 (2012) 693.
- [29] H. Sharma, R. M. Huizenga, S. E. Offerman, *J. Appl. Cryst.* 45 (2012) 705.
- [30] C. P. Scott, J. Drillet, *Scripta Mater.* 56 (2007) 489.
- [31] K.J. Andrews, *J Iron Steel Inst* 203 (1965) 721.
- [32] L. Zhao, N. M. van der Pers, J. Sietsma, S. van der Zwaag, *Mater. Sci. Forum* 500-501 (2005) 379.
- [33] K. Zhang, M. Zhang, Z. Guo, N. Chen, Y. Rong, *Mater. Sci. Eng. A* 528 (2011) 8486.
- [34] P. Hähner, K. Bay, M. Zaiser, *Phys. Rev. Lett.* 84 (1998) 2470.
- [33] P.D. Ispánovity, I. Groma, G. Györgyi, *Phys. Rev. B* 78 (2008) 024119.
- [36] Y.S. Chen, W. Choi, S. Papanikolaou, M. Bierbaum, J.P. Sethna, *Int. J. Plasticity* 46 (2013) 94.
- [37] A.C. Vermeulen, R. Delhez, H. de Keijser, E.J. Mittemeijer, *J. Appl. Phys.* 77 (1995) 5026.
- [38] W. Pantleon, C. Wejdemann, B. Jakobsen, U. Lienert, H.F. Poulsen, *Mater. Sci. and Eng. A* 524 (2009) 55.

Summary

TRIP steel is a material providing great mechanical properties. Such steels show a good balance between high-strength and ductility, not only as a result of the fine microstructure, but also because of the well-known TRIP effect. The Transformation Induced-Plasticity (TRIP) phenomenon is the transformation of the soft metastable austenite phase to the hard martensite phase due to a mechanical or a thermal stimulus. Already developed in the 1980s, these materials gained new interest since their fabrication has been achieved via a considerable reduction of relevant alloying element concentrations. The mechanical response of such steels, intended to be used in the automotive industry to decrease the gas emission of vehicles, remains difficult to predict. The reason is that the stability of austenite simultaneously depends on a number of intrinsic and extrinsic parameters. As a result, limited in-depth information can be obtained using conventional characterization techniques. Some progress has been made by means of micromechanical models developed to tailor the TRIP effect. These advanced multi-scale models that consider both the macrostructure and microstructure are valuable tools, but have so far been based on limited experimental input for validation and are likely to be not correct.

Improved physical characterization methods based on synchrotron radiation make it possible to study the transformation behaviour of the metastable phase in-situ during mechanical or thermal deformation both macroscopically and at the level of individual grains. The aim of this thesis is to quantify the microstructural parameters controlling the mechanical and thermal stability of austenite at an individual grain level using synchrotron X-ray diffraction. This thesis presents the results from experiments probing the transformation behaviour at a macroscopic scale, at a grain level scale and even at a sub-grain scale.

In Chapter 3 I report in-situ magnetization and high-energy X-ray diffraction measurements on two aluminum-based TRIP steels during cooling from room temperature down to 100 K in order to evaluate amount and stability of the retained austenite for different heat treatment conditions. I found that the bainitic holding temperature affects the initial fraction of retained austenite at room temperature but does not influence significantly the rate of transformation upon cooling.

In Chapter 4 the stability of the retained austenite has been studied in-situ in low-alloyed TRIP steels using high-energy X-ray diffraction during tensile tests at variable temperatures down to 153 K. A detailed powder diffraction analysis has been performed to probe the austenite to martensite transformation by characterizing the evolution of the phase fraction, load partitioning and texture of the constituent phases simultaneously. Our results show that at lower temperatures the mechanically induced austenite transformation is significantly enhanced and extends over a wider deformation range, resulting in a higher elongation at fracture. Low carbon content grains transform first, leading to an apparent increase in average carbon concentration of the remaining austenite. At higher deformation levels the average carbon content saturates while the austenite still continues to transform. In the elastic regime the probed $\{hkl\}$ planes develop different strains reflecting the elastic anisotropy of the constituent phases. The observed texture evolution indicates that the austenite grains oriented with the $\{200\}$ along the loading direction are transformed preferentially as they experience the highest resolved shear stress. For increasing degrees of plastic deformation the combined preferential transformation and grain rotation results in the standard deformation texture for austenite with the $\{111\}$ component along the loading direction. The mechanical stability of retained austenite in TRIP steel is found to be a complex interplay between carbon concentration in the austenite, grain orientation, load partitioning and temperature.

In Chapter 5 the microstructure evolution during shear loading of a low-alloyed TRIP steel with different amounts of the metastable austenite phase and its equivalent Dual Phase (DP) grade has been studied by in-situ high-energy X-ray diffraction methods. A detailed powder diffraction analysis has been performed to probe the austenite-to-martensite transformation by characterizing simultaneously the

evolution of the austenite phase fraction and its carbon concentration, the load partitioning between the austenite and the ferritic matrix and the texture evolution of the constituent phases. My results show that for shear deformation conditions the TRIP effect extends over a significantly wider deformation range than for simple uniaxial loading. A clear increase in average carbon content during the mechanically-induced transformation proves that austenite grains with a low carbon concentration are least stable during shear loading. The observed texture evolution indicates that under shear loading the orientation dependence of the austenite stability is relatively weak. Earlier work had shown that under a tensile load the $\{110\}\langle 001\rangle$ component transforms preferentially. The mechanical stability of retained austenite in TRIP steel is found to be a complex interplay between the interstitial carbon concentration in the austenite, the grain orientation and the load partitioning.

Chapter 6 focuses on the determination of the local retained austenite-to-martensite transformation behaviour in an inhomogeneous yet carefully controlled shear loaded region of double notched TRIP and DP steel samples. A detailed powder analysis has been performed to simultaneously monitor the evolution of the phase fraction and carbon enrichment of metastable austenite and the local strain components in the constituent phases as a function of the macroscopic stress and location with respect to the shear band. The metastable retained austenite showed a mechanically-induced martensitic transformation in the localized shear zone, which is accompanied by an apparent carbon enrichment in the remaining austenite. At the later deformation stages the geometry of the shear test samples results in the development of an additional tensile component. The experimental strain field within the probed sample area is in good agreement with the predictions from finite-element calculations. The strain development observed in the low-alloyed TRIP steel with metastable austenite is compared to that of steels with the same chemical composition yet containing either no austenite (a DP grade) or a stable (i.e. non-transforming) retained austenite fraction (a TRIP grade produced at a long bainitic holding time). The transformation of metastable austenite under shear load is a complex interplay between the local microstructure and the evolving strain fields.

In Chapter 7 the stability of individual metastable austenite grains during tensile loading has been studied in-situ. A new analysis method based on Friedel diffraction pairs has been developed to correlate the macroscopic behaviour of the material to the microstructural parameters of individual grains. The carbon concentration, grain volume and orientation have been determined from single peaks of the diffraction pattern. My results show that these three parameters control the mechanical stability, while the grain volume was found to be the dominant parameter. The orientation-dependent stability of the austenite grains with respect to the tensile axis shows a transformation sequence that is in line with their Schmid factor. It has been observed that for increasing tensile load most austenite grains transform into martensite in one step.

In Chapter 8 the martensitic transformation behaviour of the meta-stable austenite phase in low-alloyed TRIP steels during deformation has been studied in more detail. The stability of austenite has been studied at different length scales during tensile tests. A powder diffraction analysis has been performed to correlate the macroscopic behaviour of the material to the observed changes in the volume phase fraction. Moreover, the austenite transformation behaviour has been studied at the length scale of individual grains, where an in-depth characterization of four selected grains has been performed including grain volume, local carbon concentration and grain orientation. For the first time, a high resolution far-field detector was used to study the initial and evolving structure of individual austenite grains during uniaxial tensile deformation of the sample. The sub-grain size in austenite is found not to change significantly during the deformation. The final transformation to martensite occurred in either one or two loading steps.

Samenvatting

TRIP staal is een materiaal dat uitstekende mechanische eigenschappen vertoont. Het belangrijkste voordeel is de goede balans tussen een hoge sterkte en een goede vervormbaarheid, die veroorzaakt wordt door zowel de kleinschalige microstructuur als het bekende TRIP effect. Bij het Transformation Induced-Plasticity (TRIP) effect transformeert de zachte metastabiele austeniet fase in een harde martensiet fase onder de invloed van mechanische of thermische stimuli. Oorspronkelijk ontwikkeld in de 1980s, trok dit materiaal hernieuwde aandacht toen de fabricatie ervan tot stand kwam met een aanzienlijke reductie in legeringselementen. De voorspelling van het mechanisch gedrag van dergelijke stalen, bedoeld voor toepassingen in de auto industrie om de CO₂ emissie van voertuigen te verminderen, bleek moeilijk. De reden hiervoor is dat de austeniet fase gevoelig is voor een reeks van intrinsieke en extrinsieke parameters die gezamenlijk bepalend zijn voor haar stabiliteit. Hierdoor kan er maar beperkte informatie worden verkregen via de gangbare fysische karakteriseringsmethoden voor meergefasige staalsoorten. Enige voortuitgang is geboekt dankzij micromechanische modellen die ontwikkeld zijn om het TRIP effect te optimaliseren. Deze geavanceerde modellen, die diverse lengte schalen bestrijken en zowel de macrostructuur als de microstructuur in beschouwing nemen, zijn waardevolle gereedschappen maar zijn tot nu toe gevalideerd op basis van beperkte en relatief ongedetailleerde experimentele data.

Verbeterde geavanceerde karakterisatiemethoden maken het mogelijk om de metastabiele fase in-situ tijdens deformatie te bestuderen. Het doel van dit proefschrift is om de microstructurele parameters die de mechanische stabiliteit van het austeniet bepalen te kwantificeren met behulp van synchrotron Röntgen-diffractie. Dit proefschrift presenteert de resultaten van experimenten op zowel

macroscopische schaal als op de schaal van individuele korrels en zelfs op sub-korrel nivo, het presenteert daarmee een unieke beschrijving over meerdere lengteschalen.

In Hoofdstuk 3 worden in-situ magnetisatie en Röntgendiffractie metingen gepresenteerd aan twee aluminium-houdende TRIP stalen tijdens afkoeling vanaf kamertemperatuur naar een temperatuur van 100 K om de hoeveelheid en stabiliteit van het rest-austeniet te bepalen als functie van de eerder opgelegde warmtebehandeling. Gebleken is dat de bainitische transformatietemperatuur van invloed is op de initiële fractie rest-austeniet, maar niet significant van invloed is op de mate van transformatie tijdens verder afkoelen naar temperaturen onder kamertemperatuur.

In Hoofdstuk 4 is de stabiliteit van het rest-austeniet in laag-gelegeerde TRIP stalen tijdens mechanische vervorming bij temperaturen variërend van kamertemperatuur tot 153 K bepaald. Een gedetailleerde analyse van de poederdiffractie is uitgevoerd om de transformatie van austeniet naar martensiet te karakteriseren via de gelijktijdige evolutie in de fasefractie, de spanningsdeling over de aanwezige fasen en de textuur binnen elk van deze fasen. De resultaten laten zien dat bij lagere temperaturen de mate van mechanisch geïnduceerde austeniet transformatie significant toeneemt en zich uitstrekt over een breder deformatiebereik, resulterend in een hogere rek bij breuk. Korrels met een lage koolstofconcentratie transformeren als eerste waardoor het resterende austeniet een schijnbare toename laat zien in de gemiddelde koolstofconcentratie. In een later stadium bereikt de koolstofconcentratie een constant waarde, terwijl de austeniet blijft transformeren. In het elastische regime laten de gevolgde $\{hkl\}$ vlakken een verschillend verloop zien in de ontwikkelde rek, wat een gevolg is van elastische anisotropie binnen de aanwezige fasen. De waargenomen evolutie in textuur geeft aan dat de austeniet korrels met een $\{200\}$ oriëntatie langs de trekrichting als eerste transformeren aangezien zij de hoogste opgeloste schuifspanning ondergaan. Voor toenemende plastische deformatie leidt de combinatie van selectieve transformatie voor specifieke oriëntaties en korrelrotatie tot de gebruikelijke deformatie-textuur voor austeniet met $\{111\}$ component langs de trekrichting. De mechanische stabiliteit van rest-austeniet in TRIP staal blijkt een complex samenspel

tussen de koolstofconcentratie in de austeniet, de korreloriëntatie, de spanningsdeling en de temperatuur.

In Hoofdstuk 5 wordt de evolutie in de microstructuur in een laag-gelegeerd TRIP staal als gevolg van afschuifbelasting bestudeerd middels in-situ hoge-energie Röntgen-diffractie. De resultaten worden vergeleken met de data voor een overeenkomstige Dual Phase (DP) staalkwaliteit. Een gedetailleerde poederdiffractie analyse is uitgevoerd om de austeniet-naar-martensiet transformatie te bestuderen door gelijktijdig de evolutie van de austeniet fasefractie, de koolstofconcentratie, de spanningsverdeling en het textuurverloop van de aanwezige fasen te volgen. De resultaten laten zien dat onder een afschuifbelasting het TRIP effect over een aanzienlijk groter deformatie-bereik plaatsvindt dan voor simpele uniaxiale trekbelasting. Een duidelijke toename in de gemiddelde koolstofconcentratie gedurende de mechanisch geïnduceerde transformatie geeft aan dat de austeniet korrels met een lage koolstofconcentratie het minst stabiel zijn tijdens een afschuifbelasting. De waargenomen textuurevolutie geeft aan dat onder afschuifbelasting de oriëntatie-afhankelijkheid van de austeniet stabiliteit relatief gering is, terwijl eerder gevonden was dat onder trekbelasting $\{110\}\langle 001 \rangle$ component bij voorkeur transformeert. De mechanische stabiliteit van rest-austeniet in TRIP staal blijkt een complex samenspel tussen de initiële koolstofconcentratie in het austeniet, de oriëntatie van de korrel en de spanningsverdeling.

Hoofdstuk 6 richt zich op de bepaling van de lokale transformatie van rest-austeniet naar martensiet in een gebied met een inhomogene maar nauwkeurig gecontroleerde afschuifdeformatie in TRIP en DP preparaten met een dubbele insnijding. Een gedetailleerde poederanalyse is uitgevoerd om gelijktijdig de evolutie van de fasefractie en koolstof concentratie van het metastabiele austeniet en de lokale rekcomponenten van de aanwezige componenten als functie van de macroscopische spanning en locatie ten opzichte van de afschuivingsband te bepalen. De metastabiele rest-austeniet vertoont een mechanisch geïnduceerde martensitische transformatie in de gelokaliseerde afschuifzone, welke samengaat met een toename in gemiddelde koolstofconcentratie van de overgebleven austeniet. In de latere deformatiestadia leidt de geometrie van de proefstukken gedimensioneerd voor zuivere

afschuifvervorming tot de ontwikkeling van een aanvullende axiale rekcomponent. Het experimenteel bepaalde deformatieveld in de onderzochte preparaten is in goede overeenstemming met de resultaten van eindige-elementen berekeningen. De ontwikkeling van de vervorming in het laag-geleegde TRIP staal met metastabiel austeniet is vergeleken met dat van staalsoorten met dezelfde chemische samenstelling die geen austeniet (een DP staal) of een stabiele rest-austeniet fractie bevatten (een TRIP staal geproduceerd met een langere bainitische transformatietijd). De transformatie van de metastabiel austeniet onder een afschuifbelasting bleek het resultaat te zijn van een complex samenspel tussen de lokale microstructuur en de zich evoluerende deformatievelden.

In Hoofdstuk 7 is de stabiliteit van individuele austenietkorrels in metastabiele conditie tijdens trekbelasting in-situ bestudeerd. Een analysemethode gebaseerd op het gebruik van Friedel gepaarde diffractiespots is ontwikkeld om het macroscopische gedrag in het materiaal te correleren aan de microstructurele parameters van individuele korrels. De koolstofconcentratie, het korrelvolume en oriëntatie zijn bepaald op basis van individuele pieken in het diffractiepatroon. Onze resultaten laten zien dat de drie eerder genoemde parameters de mechanische stabiliteit bepalen, waarbij het korrelvolume een dominante rol speelt. De oriëntatie-afhankelijke stabiliteit van de austenietkorrels ten opzichte van de trekrichting laat een transformatievolgorde zien die in overeenstemming is met de waarde van hun Schmid factor. De meeste austenietkorrels transformeren in één enkele stap bij toenemende trekbelasting, maar ook twee-traps transformatiegedrag is waargenomen. Ook dit onderzoek laat zien dat de mechanische stabiliteit van individuele austenietkorrels een complex samenspel is tussen de microstructurele parameters en de extern opgelegde vervorming.

In Hoofdstuk 8 wordt het transformatiegedrag van de metastabiele austenietfase in laag-geleegde TRIP stalen in situ tijdens axiale deformatie beschreven. De stabiliteit van austeniet is onderzocht op verschillende lengteschalen. Een poederdiffractie analyse is toegepast om het macroscopische gedrag van het materiaal te correleren aan de waargenomen veranderingen in de volume fractie. Daarnaast is het austeniet transformatiegedrag bestudeerd op de lengteschaal van individuele korrels, waarbij er een diepgaande karakterisatie van vier geselecteerde korrels voor wat

betreft het korrelvolume, de lokale koolstofconcentratie en oriëntatie van de korrels is uitgevoerd. Voor het eerst is er een hoge-resolutie detector-op-grote afstand gebruikt om de initiële en de zich ontwikkelende structuur van individuele austenietkorrels te bestuderen tijdens axiale deformatie. De metingen lieten zien dat de afmetingen van sub-korrels in afzonderlijke austeniet korrels niet significant veranderen tijdens de deformatie. De uiteindelijke transformatie naar martensiet vindt in één of twee stappen plaats.

List of publications

Blondé, R., Jimenez-Melero, E., Zhao, L., Wright, J.P., Brück, E., van der Zwaag, S., van Dijk, N.H. *High-energy X-ray diffraction study on the mechanical stability of individual austenite grains in low-alloyed TRIP steels* (2014) In preparation.

Blondé, R., Jimenez-Melero, E., Huizenga, R., Zhao, L., Wright, J.P., Brück, E., van der Zwaag, S., van Dijk, N.H. *High resolution XRD investigation on the evolution of the substructure of individual austenite grains in TRIP steels during tensile deformation* (2014) Journal of Applied Crystallography, Submitted.

Blondé, R., Jimenez-Melero, E., Ponnusami, S.A., Zhao, L., Schell, N., Brück, E., van der Zwaag, S., van Dijk, N.H. *Position-dependent shear induced austenite-martensite transformation in double notched TRIP and DP steel samples* (2014) Journal of Applied Crystallography, Submitted.

Blondé, R., Jimenez-Melero, E., Zhao, L., Schell, N., Brück, E., van der Zwaag, S., van Dijk, N.H. *The mechanical stability of retained austenite in low-alloyed TRIP steel under shear loading* (2014) Materials Science and Engineering A, **594**, pp. 125-134.

Blondé, R., Jimenez-Melero, E., Zhao, L., Wright, J.P., Brück, E., van der Zwaag, S., van Dijk, N.H. *Multi length scale characterization of austenite in TRIP steels using high-energy X-ray diffraction* (2013) Powder Diffraction, **28** (2), pp. 77-80.

Jimenez-Melero, E., Blondé, R., Sherif, M.Y., Honkimäki, V., van Dijk, N.H. *Time-dependent synchrotron X-ray diffraction on the austenite decomposition kinetics in SAE 52100 bearing steel at elevated temperatures under tensile stress* (2013) Acta Materialia, **61** (4), pp. 1154-1166.

Blondé, R., Jimenez-Melero, E., Zhao, L., Wright, J.P., Brück, E., van der Zwaag, S., van Dijk, N.H. *High-energy X-ray diffraction study on the temperature-dependent mechanical stability of retained austenite in low-alloyed TRIP steels* (2012) Acta Materialia, **60** (2), pp. 565-577.

Blondé, R., Jimenez-Melero, E., van Dijk, N.H., Brück, E., Zhao, L., Sietsma, J., van der Zwaag, S. *Microstructural control of the austenite stability in low-alloyed TRIP steels* (2011) *Diffusion and Defect Data Pt.B: Solid State Phenomena*, **172-174**, pp. 196-201.

Blonde, R., Chan, H.-L., Allain-Bonasso, N., Bolle, B., Grosdidier, T., Lu, J. *Evolution of texture and microstructure in pulsed electro-deposited Cu treated by Surface Mechanical Attrition Treatment (SMAT)* (2010) *Journal of Alloys and Compounds*, **504** (SUPPL. 1), pp. S410-S413.

Acknowledgements

This thesis is the result of four years of research at the group of Fundamental Aspects of Materials and Energy, in the Faculty of Applied Sciences of the Delft University of Technology. This research was carried in the framework of the Research Program of Materials innovation institute (M2i) in the Netherlands. The thesis would not have been possible without the support and help of many people to whom I would like to express my sincere gratitude.

First of all, I would like to thank my promotors, Prof.dr.ir. S. van der Zwaag and Prof.dr. E.H. Brück for offering me the opportunity to come to Delft to pursue my Ph.D. degree and for their excellent guidance, tremendous support and enthusiastic encouragement. It was a great honour to work with them.

Another very important person to whom I am especially grateful is my daily supervisor Dr.ir. N.H. van Dijk. I thank him for his enormous effort and for the long hours he has spent on my Ph.D. project. I acknowledge his valuable guidelines in the development of this research and the intensive daily stimulating discussions. Moreover, I would like to thank him for his great help in improving my written and spoken English. To finish, I would like also to thank him for being more than simply a supervisor for our non-scientific talks. Thank you a lot Niels!

An important contribution to my thesis was given by Dr.E. Jimenez-Melero who took part in the daily supervision of my Ph.D. research during the two first years. I appreciated our discussions and the guidance in my research. I would like also to thank Dr. L. Zhao, who was an important member of this research team, for our great discussions and support for the sample preparations and synchrotron experiments.

I would like to thank Dr. J. Wright and Dr. N. Schell responsible of the ID11 ESRF and P07 PETRA beamlines respectively, for their contribution and support to the synchrotron experiments and data

analysis. I would like also to thank Mr. Huizenga for the contribution in the data analysis of the Far-field synchrotron experiments.

M2i needs to be acknowledged for providing to researchers a wonderful platform between industry and academia. The great effort to provide the best working conditions, knowledge transfer, training, social activities and great care of the employee was essential to accomplish this thesis with the maximum performance. I would like to especially thank Monica Reulink who always supported me during my PhD research.

I would like to thank Dr. D. Hanlon from TATA steel for the support and contribution in my work. During these four years, we had stimulating discussions which helped me to better understand the difficult aspects of this research.

I am grateful to Nicole and Ilse for their administrative support, Hans, Nico, Erik, Anton, Fred, Michel, Piet, Lian and Jouke for their technical support, my colleagues of the FAME group, NPM2 group, MCM group and NOVAM group for their help and pleasant time at the university. Let me acknowledge: Shasha, Inês, Karel-Alexander, Deepak, Ou, Zhouzhou, Xiaoyu, Anna, Anca, Swapna, Ze, Luana, Léon, Wingkee, Gijs, Jacob Jan, Remco, Miao, Fengjiao, Shangming, Kun, Yibole, Thang, Prasad, Maurits, Andrea, Maria, Pina, Patricia, Gözde, Jai, Kirk, Onnaz, Dennis, Hemant, Sebastian, Francois, Alexis, Hao, Jason and Stéphane. I gratefully acknowledge my friends whom I shared great moments of my life during these four years in Delft, Marcelo, David, Kon, Freddy, Daniel, Hugo and a very especially thanks to my flatmates, Sarah and Ambroise.

I would like to express my deep sense of gratitude to Dr. B. Bolle, Prof.dr. A. Tidu and Prof.dr. T. Grosdidier from the Laboratoire d'Etude des Microstructures et de la Mécanique des Matériaux, Metz, France. They introduced me to many areas of metallurgy and sparked my interest in this particular field.

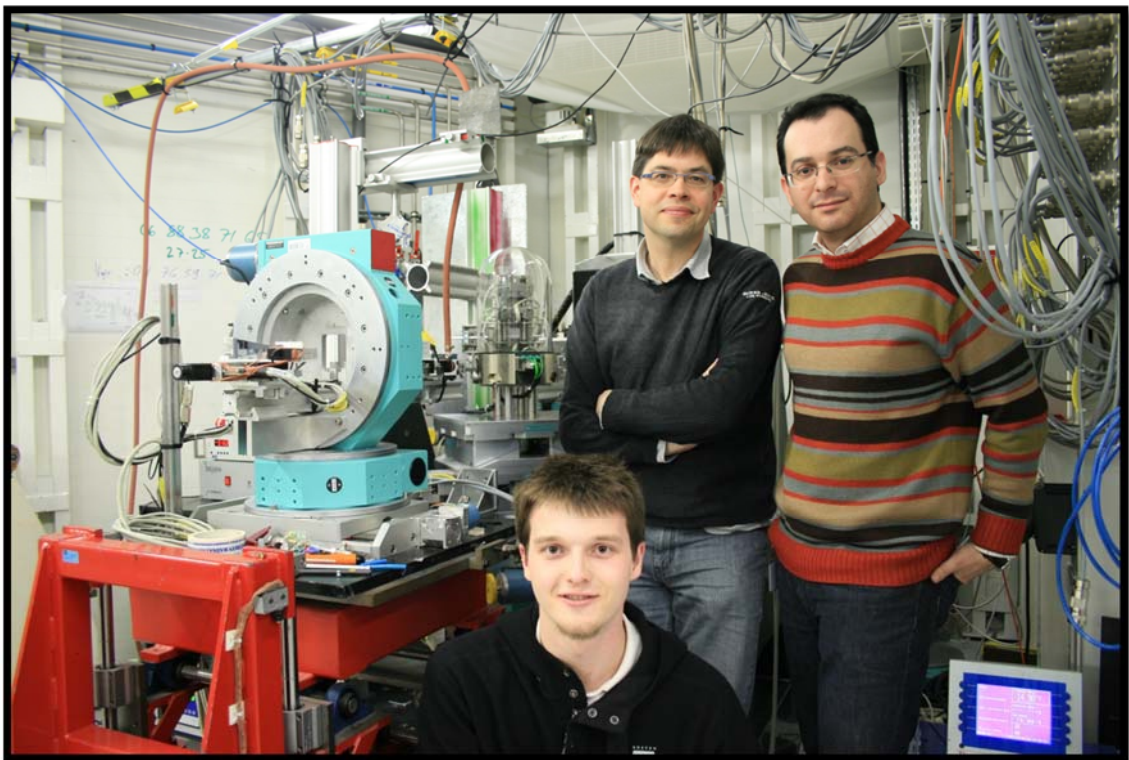
I wish to sincerely thank all other committee members, Prof.dr. M. Preuss, Dr.Ing. U. Prah, Prof.dr.ir. A.S.J. Suiker, and Prof.dr.ir. J. Sietsma, for their comments on the thesis.

Finally, I would like to deeply thank all my family. My mother and grandmother were the pillars of this success by giving me the support and guidance throughout my life. They deserve huge appreciation for helping shape me into the person I am today.

Last but not least, a special thanks goes to my girlfriend, Helena, for her help, love, support and understanding.

Romain Blondé

Delft, 23 Feb 2014



Niels van Dijk, Enrique Jimenez-Melero and Romain Blondé conducting in-situ experiment at the ID15 beamline of the European Synchrotron Radiation Facility (ESRF) in March 2010.

Curriculum Vitae

Romain Jean-Luc Patrick Blondé

Born on 19 November 1985 in Belfort, France

Education

2001-2004 **Baccalaureate in Science**, option: Physics and Chemistry.

Lycée les Haberges, Vesoul, France.

2004-2009 **Diploma of Mechanical Engineer**, specialization: research, development and innovation.

Ecole Nationale d'Ingénieurs de Metz (ENIM), Metz, France

2008-2009 **Master Degree**, specialization: Materials science.

Paul-Verlaine University of Metz, France, in partnership with Ecole Nationale Supérieure d'Arts et Métiers (ENSAM), Metz, France and Ecole Nationale d'Ingénieurs de Metz (ENIM), Metz, France.

Thesis title : *“Study of nanostructured surface layers induced by Surface Mechanical Attrition Treatment (SMAT) on electro deposited materials”*

2009-2014 **PhD Degree**, specialization: Materials sciences.

M2i (Materials innovation institute); Delft University of Technology, The Netherlands.

Thesis title : *“Austenite stability in TRIP steels studied by synchrotron radiation”*